Important Notice

This copy may be used only for the purposes of research and private study, and any use of the copy for a purpose other than research or private study may require the authorization of the copyright owner of the work in question. Responsibility regarding questions of copyright that may arise in the use of this copy is assumed by the recipient.

UNIVERSITY OF CALGARY

Exploring Potential Applications of the Sharpe Hollow Cavity Model, the Gaussian Ball Source Model, and the Heelan Cylindrical Model in Modeling Explosive Pressure Sources

by

Christopher Craig Petten

A THESIS

SUBMITTED TO THE FACULTY OF GRADUATE STUDIES

IN PARTIAL FULFILLMENT OF THE REQUIREMENTS FOR THE

DEGREE OF MASTER OF SCIENCE

GRADUATE PROGRAM IN GEOLOGY AND GEOPHYSICS

CALGARY, ALBERTA

August, 2015

© Christopher Craig Petten 2015

Abstract

This thesis investigates the potential applications of the Sharpe Hollow Cavity Model (SHCM), the Gaussian Ball Source Model (GBSM), and the Heelan Cylindrical Model (HCM) in modelling explosive pressure sources.

Each of these models account for the non-linear nature of wave propagation near an explosive source by mathematically altering the conditions around the source, and replacing it with a model that is more easily understood.

Both the SHCM and the HCM replace the source with a hollow cavity, within which waves do not behave linearly, and elastic waves are assumed to emanate directly from the surface of the cavity. The GBSM does not use a cavity and replaces the explosion with a Gaussian ball; elastic waves are then assumed to emanate from a point in space.

Each of these models were able to make reasonably accurate predictions about the nature of dynamite data measured in the field.

Acknowledgements

I would like to first and foremost thank my spouse, Kimberly Ryan, and our three little ones, Grace, Cameron, and Connor, for their continued love and support throughout this process; I know that patience has been a virtue for Kimberly during the writing of this thesis. Additionally, I would also like to acknowledge the contributions of our other family members, Bradly (the cat) and Becca (the dog). My family is the most important thing in my life, and I don't know where I would be without you guys.

I would like to thank my parents, Colin and Geraldine Petten, for their support throughout my education, and for all they've done for me throughout the years. After having my own children, I truly realize how much you've done for me, and I am eternally grateful for everything that you've done. I would like to thank Ed and Laura Ryan for their continued support, and welcoming me so easily into their family. I would also like to thank their dogs, Belle and Baron for their continued support and drool contributions.

My grandmother, Nora Petten, I want to thank you so much for the love and support you've given me throughout the years, and even though we are separated by an entire country, you are still near to me in my heart. I wish my grandfathers, George Petten and Samual Frampton, were still around for this event in my life, but I know they would have been proud and I can't express how grateful I am to have had them in my life.

I would like to thank Dr. Michael Wieser for the efforts that he put into my undergraduate career. I think that my time working in your lab has been the main reason I was able to function in graduate school as a budding Physicist. Thank you for teaching me how to be a scientist, and I can only hope that many other undergraduates have the opportunity to learn from you and grow the way I have.

Dr. Gary Margave, whom I'm sure patience has also been a virtue within this process. I can't thank you enough for taking me on as a graduate student, and although there have

been some very trying times (like trying to get me to understand how the equation of a straight line works), I'm honored to have had the opportunity to learn from you. I have no doubt that I will be a better Physicist because of your influence.

Dr. Larry Lines, I would like to thank you for your guidance throughout my undergraduate career and taking the time out of your busy schedule to be part of my defense committee, it was truly an honor.

Laura Baird, you've done so much for everyone at CREWES, I don't even know where to start. I can't even count the number of times you've helped me with the simplest of things that I couldn't figure out (like how to use the photocopier downstairs), and the difficult things that would have taken me a long time to figure out (like what I'm supposed to do with certain things in PeopleSoft). I'm sure this isn't the first time you've heard this, but your continued support of the CREWES project and its students is very much appreciated.

I would like to thank everyone that has supported me throughout the years, and I can't express in words how much I appreciate what you've done for me.

Table of Contents

List of Tables

List of Figures and Illustrations

Chapter 1

Introduction

1.1 Dynamite in Practice

Explosive sources are commonly used in seismic exploration to image the subsurface due to the relatively cheap cost and effectiveness in producing elastic wave energy. Figure 1.1 shows a typical seismic survey using dynamite. A charge is buried beneath the surface at a depth that is usually dependent on the charge size, with larger charge sizes generally being buried deeper than smaller charges. When the dynamite is detonated, energy is emitted from the source in the form of elastic wave energy that interacts with features in the subsurface such as reflectors. Note that reflectors are usually the boundary between different layers of rocks, which due to the difference in composition between the two layers, causes elastic waves to reflect and return to the surface. The time required for the waves to return to the surface can be used to determine the depth of the reflectors. Such information is extremely useful in oil and gas exploration, and any other application requiring an image of the subsurface.

The amplitude of the waves that return to the surface are directly proportional to the amount of charge that is used. Larger sources emit more energy, and thus the waves emitted by such sources are higher in amplitude. This results in larger charge sizes being more powerful, and thus they are more effectively able to image the subsurface. However, as will be seen in this study, larger charge sizes tend to produce lower dominant frequencies, which can be a limitation when processing data. By developing our understanding of the waves that are emitted from explosions, we may be able to improve the quality of seismic surveys. The power of the source and the frequency of the emitted waves are of particular importance in the study of Geophysics, as the power of the shot determines our capability of imaging certain features in the subsurface, and the frequency of the emitted waves plays

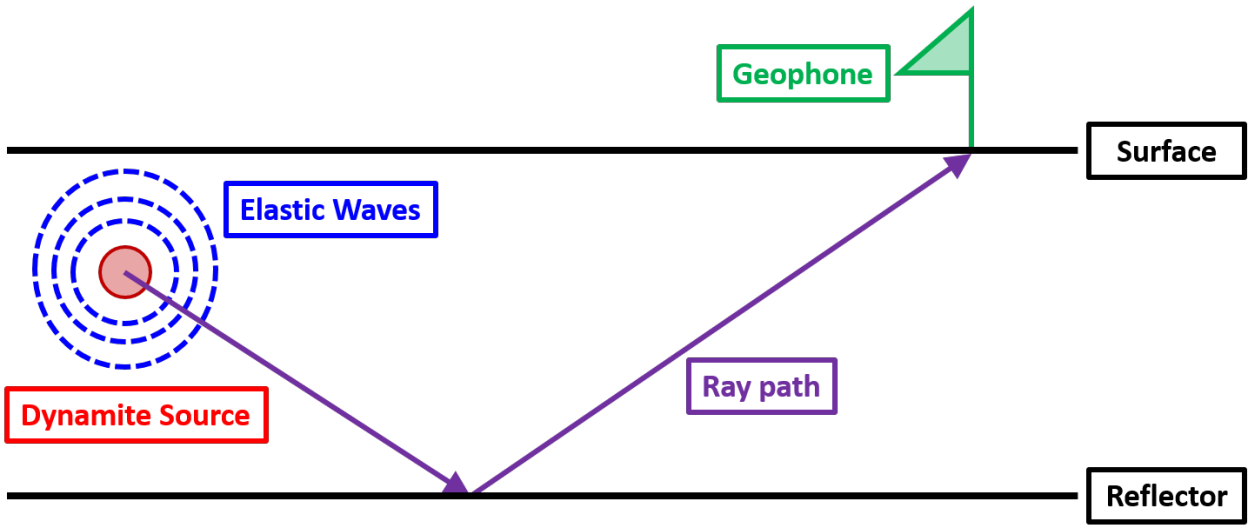

Figure 1.1: Diagram of a typical seismic survey using dynamite. The dynamite source is shown in red, and the geophone that is used to detect the emitted elastic waves is shown in green. When a source detonates, energy is emitted from the source in the form of elastic waves (shown in blue) and follows a ray path (shown in purple). The disturbances caused by this energy is detected by the geophone, and the data obtained offers valuable insight into the subsurface for Geophysicists.

a very important role in processing the data so that it can be used in any application where an image of the subsurface is required.

1.2 Models Used to Characterize Dynamite

There have been numerous studies conducted since the early 1940s that have attempted to characterize and predict the nature of the energy emitted from an explosive source. Three of these models that are of particular interest in this study are the Sharpe Hollow Cavity Model (SHCM), the Heelan Cylindrical Model (HCM), and the Gaussian Ball Source Model (GBSM). One of the most difficult challenges associated with modeling explosive pressure sources, is the fact that waves do not behave linearly in regions that are close to the source. Within this region, we cannot use the elastic wave equation to describe the motion of the wave. Each of these previously mentioned models attempts to account for the nonlinear nature of wave propagation near the source of the explosion by mathematically altering the

conditions of the source by replacing it with a more easily understood model. In the case of the SHCM and the HCM, an "equivalent cavity" is used to isolate the region of non-linear propagation; linearly propagating elastic waves are then assumed to propagate from the surface of this cavity (Sharpe, 1942)(Heelan, 1953). The GBSM on the other hand assumes that the energy of the source is rapidly deposited into the surroundings without considering this hollow cavity. Due to the rapid nature of energy transfer in this scenario, the emitted waves are assumed to behave linearly (Aldridge, 2011).

1.3 Motivation of the Thesis

This thesis explores the viability of each of the aforementioned models in predicting features of dynamite data that has been obtained in the field. This was accomplished by investigating the ability of each model to accurately predict the amplitude and frequency content of waves emitted by dynamite explosions. We hope that by conducting this investigation, we can more effectively utilize each of these models to improve the quality of dynamite surveys by controlling the amplitude and frequency content of the data. This can be accomplished by selecting the appropriate charge sizes, which can be determined by each of the models that we are studying, to produce a desired amplitude and frequency response.

1.4 Overview of Methods

We have three data sets that we worked with in this study. For each data set we measured the amplitude and frequency content that results from different experimental parameters, such as charge size or borehole orientation. We then compare these data to theoretical predictions made by each model in order to determine how accurately they can make predictions about the data that was obtained in the field.

1.5 Overview of Chapters

This thesis is presented in 10 chapters. Chapters 2 through 4 present the theory of the SHCM, GBSM, and the HCM respectively, as well as their relevant derivations. We explore the features of each of these models in these chapters, and how we plan to apply it to data obtained in the field.

Chapter 5 contains an overview of the data that was obtained in the field from the Hussar 2011, Priddis 2012, and Priddis 2013 experiments. Chapter 6 contains a discussion of spectral notching and source ghosts, which present a source of potential uncertainty in this study. For each of the models tested, we did not include a free surface in the modeling; by excluding a free surface we are not accounting for source ghosts and multiples. These contribute to a phenomenon known as spectral notching, and it could potentially be the most significant source of error in this study.

The Hussar 2012 and Priddis 2013 field experiments were used to test both the SHCM and the GBSM models in practice, which can be found in Chapters 7 and 8 respectively.

The Priddis 2013 experiment was used to test the HCM model, as this data set contained shots that were drilled at an angle, allowing us to test the effect of borehole orientation on amplitude and frequency content. The results of this part of the study can be found in Chapter 9.

Finally, Chapter 10 consists of our conclusions and suggestions for future research.

1.6 Software and Development

All of the analyses for this study was conducted in MATLAB using code that was built from components of the CREWES software package. These components include:

- **fftrl** - a function used to compute Fourier transforms
- **stat** - a function used to time shift a data set

- **convm** - a function used to compute minimum phase convolution
- **fxtran** - a function used to obtain the frequency spectra within a predefined time window
- **plotgathers** - a plotting tool

Each of these functions were used to write the MATLAB code that we used for the analysis of the data obtained in the field, as well as to investigate the theory of each model in this study. The original code developed for this study are as follows:

- **sharpeCav** - a function used to compute the theoretical dominant frequency and shot power as a function of cavity radius in the SHCM
- **gaussCav** - a function used to compute the theoretical dominant frequency and shot power as a function of the Gaussian ball width
- **heelanCav** - a function used to compute the theoretical dominant frequency and shot power with varying borehole orientation
- **shotData** - a script used to compute the dominant frequency, frequency spectra, and shot power for each data set
- **computeMaxAzimuth** - a function used to compute the rotation angle of each individual sensor such that the maximum radial or transverse energy are produced
- **rotateRecord** - a function used to rotate the record using the angles determined by the computeMaxAximuth function
- **extractRadiation** - a function used to extract the radiation pattern for each individual sensor in the rotated record that results from the rotateRecord function

1.7 Original Contributions

Determining the link between charge size and cavity radius is of utmost importance in the SHCM. Equally important is the link between charge size and Gaussian ball width in the GBSM. For the SHCM we have developed a method to link the charge size to the cavity radius via a medium-specific proportionality constant, which is determined by computing the dominant frequency of the waves emanating from sources of varying charge size. This has been covered in Chapter 7 of the thesis.

We attempted to link the Gaussian ball width and charge size, however we found that we were not able to produce significant enough variations in the ball width to match observations of the amplitude and frequency content of data obtained in the field. This suggests that we may not be able to use this model to predict the features of the waves emanating from smaller sources, since we cannot produce significant enough variations in the ball width to match the model to our data sets. This has been covered in Chapter 8 of the thesis.

Based on the theory of the HCM, it was suggested that the orientation of the borehole may affect the amplitude and frequency content of waves emanating from a borehole containing an explosive source. We developed a method of rotating the sensors in the record to produce the maximum transverse and radial energy, and from these records we extracted the radiation pattern using each individual sensor. We were able to observe features in these radiation patterns that could possibly be attributed to the theory of the HCM, however we may require further investigation to make any sort of reliable conclusions. This has been covered in Chapter 9 of the thesis.

Chapter 2

The Sharpe Hollow Cavity Model

2.1 Theory and Derivation

A major challenge involved with explosions in theoretical seismology is the fact that elastic waves do not propagate linearly in the regions near the source (Sharpe, 1942). This problem is still being researched extensively by various research institutions, and the problem is often attributed to rapid melting and deformation of the surrounding subsurface when the source is detonated (Sramek and Ricard, 2007). To address this issue, Sharpe developed a model that encloses the region of rapid melting and compaction with a theoretical hollow cavity, within which waves do not behave linearly. This reduces the problem to a scenario where a pressure pulse $p(t)$ (which represents the source of the explosion) acts uniformly over the interior of the cavity, resulting in the emission of compressional waves from its exterior walls.

Figure 2.1 shows a graphical depiction of the SHCM. The radius of the cavity corresponds to the amount of energy that is released during the explosion, with larger cavity radii representing greater amounts of energy being emitted by the source (Sharpe, 1942). When dealing with dynamite, which was the only source used when obtaining data for this study, it is important to note that larger charge sizes in general produce greater amounts of energy when they are detonated (Nicholls, 1965). Therefore, when modeling dynamite explosions using the SHCM, larger cavity radii represent larger charge sizes in the field. Currently, there is no direct link between cavity radius and charge size, which could present a limitation of this model when trying make predictions about dynamite data obtained in practice (O'Brien, 1957). At this point, we can only assume that they are linked via some proportionality constant, which we will examine later on this study.

The particle displacement that is predicted by the SHCM is what we are most interested

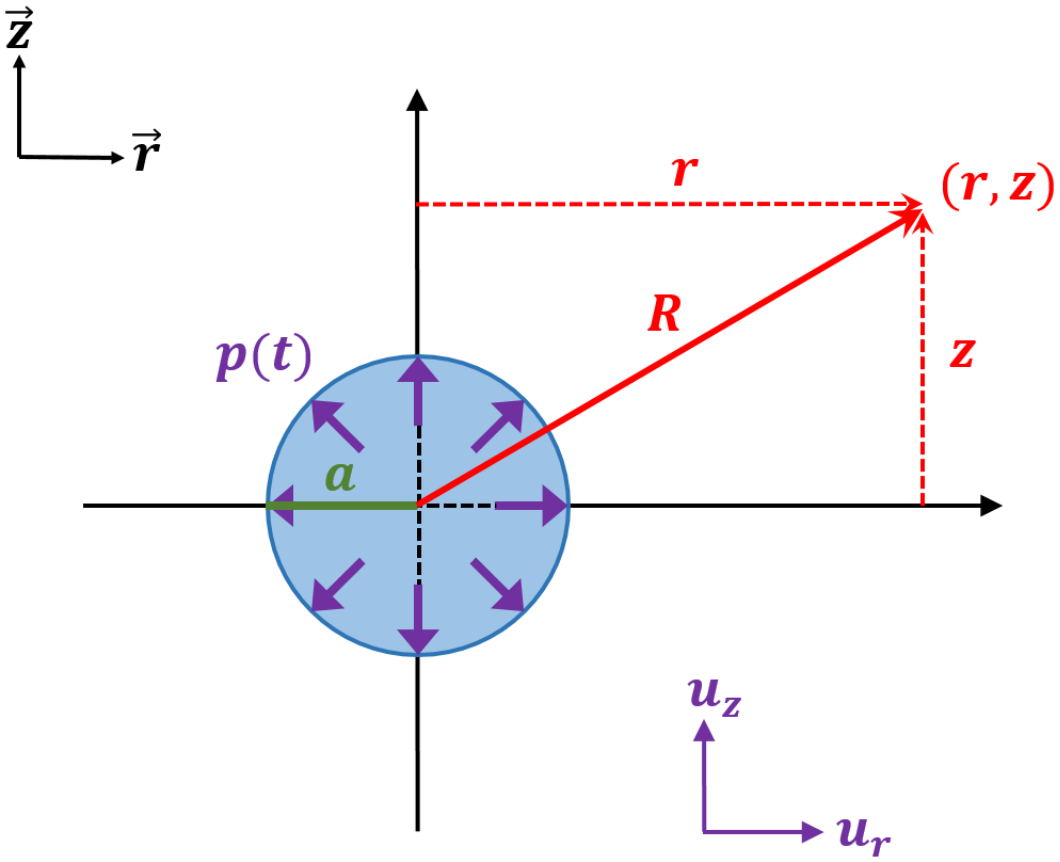

Figure 2.1: A graphical depiction of the SHCM. The region of nonlinear wave propagation is surrounded by a spherical cavity of radius a, reducing the problem to a scenario where a unit form of pressure acts over the interior of the cavity walls. Application of this pressure pulse to the interior of the cavity, results in compressional waves being emitted radially from the exterior of the cavity.

in for the purposes of this study, as it will allow us to predict the dominant frequency and amplitude response of dynamite data that we obtain in the field. Derivation of the particle displacement in the SHCM starts with the Equation of Motion (EOM) (Sharpe, 1942):

$$\rho \frac{\partial^2 \mathbf{q}}{\partial t^2} = (\lambda + 2\mu)\ \nabla\ \nabla \cdot \mathbf{q} - \mu\ \nabla \times \nabla \times \mathbf{q}, \tag{2.1}$$

where ρ is the density of the medium, $\mathbf{q}$ is the displacement, and λ and μ are the Lamé elastic constants. Sharpe proposed a solution to the EOM that was of the form:

$$\mathbf{q} = \nabla\ \Phi, \tag{2.2}$$

provided that it satisfies the wave equation

$$\frac{\partial^2 \Phi}{\partial t^2} = v^2 \nabla^2 \Phi, \tag{2.3}$$

where v is the velocity of the compressional waves in the media, and Φ is a spherical potential. In terms of the Lamé parameters defined earlier, the velocity in the media can be expressed as

$$v = \sqrt{\frac{\lambda + 2\mu}{\rho}}, \tag{2.4}$$

which will be used later in this derivation. Careful examination of Figure 2.1 shows that if the center of the cavity is placed at the origin of a polar coordinate system, the pressure is applied uniformly over the interior of the surface of the cavity. As a result of this, the resulting particle motions will depend only on the radial terms and operate independently of the angular variables. Under this assumption, we can reduce the EOM in Equation 2.1 to

$$\frac{\partial^2 (r\Phi)}{\partial t^2} = v^2 \frac{\partial^2 (r\Phi)}{\partial r^2}, \tag{2.5}$$

where the particle displacement is given by

$$\mathbf{u} = \frac{\partial \Phi}{\partial r}. \tag{2.6}$$

In the previous two equations, r is the distance from the point of origin to the point of observation, t is time, and $\mathbf{u}$ is the particle displacement.

The choice of pressure pulse $p(t)$ in this model is completely arbitrary however, it has to fulfill a very important boundary condition: the resulting displacement of the media has to be equal at both the interior and exterior of the cavity walls. As suggested by Sharpe in his original paper, one such pressure pulse that meets this criteria is

$$-\left[(\lambda+2\mu)\frac{\partial u}{\partial r}+\frac{2\lambda\mu}{r}\right]_{r=a}=p(t). \tag{2.7}$$

At this point, the problem is greatly simplified if we assume that the Lamé parameters are equal. Under this assumption, and using the expression for P-wave velocities given in Equation 2.4, Equation 2.7 can be written as

$$p(t)=-\rho v^2\left[\frac{\partial u}{\partial r}+\frac{2u}{3r}\right]. \tag{2.8}$$

Since the cavity is spherical in the SHCM, a harmonic solution representing a wave diverging from a spherical body is most desirable (Sharpe, 1942). One such solution is

$$\Phi=\frac{1}{r}\,e^{-int}, \tag{2.9}$$

where n is an integer value, t is time, and r is the distance from the center of the cavity to the point of observation. Spherical divergence is a commonly observed phenomenon in wave propagation from an explosive source (Sheriff, 1975). A major advantage of this particular solution is the fact that it accounts for spherical divergence with the $1/r$ term.

It would be useful to reduce the spherical potential Φ, given in Equation 2.5, to something that can be solved analytically when it is used in Equation 2.3, which is the elastic wave equation. Any function that is independent of r and t, multiplied by the RHS of Equation 2.9 is a solution for Φ (Arfken, 1985). Similarly, a sum of such solutions would also be a solution for Φ (Arfken, 1985), and thus Equation 2.9 can be rewritten as

$$\Phi=\frac{1}{2\pi r}\int_{-\infty}^{\infty}\int_{-\infty}^{\infty}A(n)p(\gamma)e^{in(\gamma-t)}dnd\gamma, \tag{2.10}$$

where $p(\gamma)$ is the pressure pulse that is applied to the medium, and $A(n)$ is an arbitrary function. This equation represents a viable solution to the EOM shown in Equation 2.5

(Sharpe, 1942). Also note that the proposed solution in the above equation is only valid if it can be expressed as a harmonic function (Bayin, 2006). In order to incorporate the hollow cavity into this model and maintain a harmonic solution, Sharpe used the following arbitrary function for $A(n)$ in Equation 2.10:

$$A(n) = \frac{(a/\rho)}{n^2 + 4inv/3a - 4v^2/3a^2}, \tag{2.11}$$

where a is the radius of the cavity in meters, and n is an integer value representing the harmonic. (Arfken, 1985)(Sharpe, 1942). Substituting this value of $A(n)$ into Equation 2.10 along with the boundary condition given in Equation 2.8, yields the expression

$$\Phi = \frac{a}{2\pi\rho r} \int_{-\infty}^{\infty} \int_{-\infty}^{\infty} \frac{p(\gamma) e^{in(\gamma - t)} dn d\gamma}{n^2 + 4inv/3a - 4v^2/3a^2}. \tag{2.12}$$

The solution shown in the above equation is the formal solution to the wave equation in polar coordinates, which is given in Equation 2.5.

Upon obtaining the expression in Equation 2.12, we can ascribe a pressure pulse to the SHCM using the $p(\gamma)$ term. Sharpe decided that a unit pressure pulse multiplied by a time-dependent exponential function would be most desirable in this case, such that

$$p(t) = p_o e^{-\alpha t} \text{ for } t \geq 0, \tag{2.13}$$

where α is a positive constant, and p_o is a unit pressure pulse applied to the interior of the cavity walls. The SHCM makes the assumption that a pressure pulse acts within the cavity on the interior of the walls. Therefore, time zero is assumed to be the moment when waves are emitted from the outside walls of the cavity. Therefore, within the cavity α has a value of zero in order to satisfy the boundary condition ascribed to this model, and we are left with the unit pressure pulse p_o within the cavity. Substituting this value for pressure into Equation 2.12 and using the residue theorem as shown presented by Bayin (Bayin, 2006), the following expression is obtained:

$$\Phi = \frac{ap_o/\rho r}{(\omega/\sqrt{2} - \alpha^2) + \omega^2} \left[-e^{-\alpha t} + e^{-\omega t/\sqrt{2}} \left\{ \left(1/\sqrt{2} - \alpha/\omega \right) \sin \omega t + cos\omega t \right\} \right]. \tag{2.14}$$

In the above equation, ω is the angular frequency of the oscillating terms in the solution, which is given by

$$\omega = \frac{2\sqrt{2}v}{3a}. \tag{2.15}$$

For this derivation, we have assumed that the medium is homogeneous by setting the Lamé constants equal to one another. Under this assumption, the angular frequency ω of the solution for Φ can be approximated as the angular frequency of the waves resulting from the SHCM (Sharpe, 1942). Finally, the particle displacement can be computed using the solution for Φ given in Equation 2.14 with the displacement equation, $u = \partial\Phi/\partial r$. The particle displacement that results from this computation is

$$u = \frac{a^2 p_o}{2\sqrt{2}\mu R} e^{-\omega t/\sqrt{2}} \sin \omega t, \tag{2.16}$$

where p_o is a unit pressure pulse, μ is the Lamé parameter for rigidity in Newtons per meter, R is the distance in meters from the center of the source to the point of observation, ω is the angular frequency of the wave in Hz, and t is time in seconds. Note that we have changed r to R in this case because we are now assuming that it is constant; in the derivations r was assumed to be a variable. This change in notation is strictly a matter of convenience. Equation 2.16 is a scalar value, and therefore represents the radial portion of the particle displacement. Note that the direction of particle motion in the SHCM is always assumed to be radially outwards from the center of the source (Sharpe, 1942).

The expression that we have obtained for the particle displacement assumes a unit pressure pulse (a pulse of ones) over the interior of the cavity surface. The displacement for an arbitrary pulse can be obtained by convolving the desired pulse with the expression in Equation 2.16. This can be done by carrying out the following operation:

$$U(t) = \frac{d}{dt} \int_0^t p(n)u(t-n)dn, \tag{2.17}$$

where U is the resulting particle displacement after application of a desired arbitrary pressure pulse, p is the desired pulse, and u is the particle displacement resulting from application of a unit pressure pulse, which is given by Equation 2.16 (Sharpe, 1942).

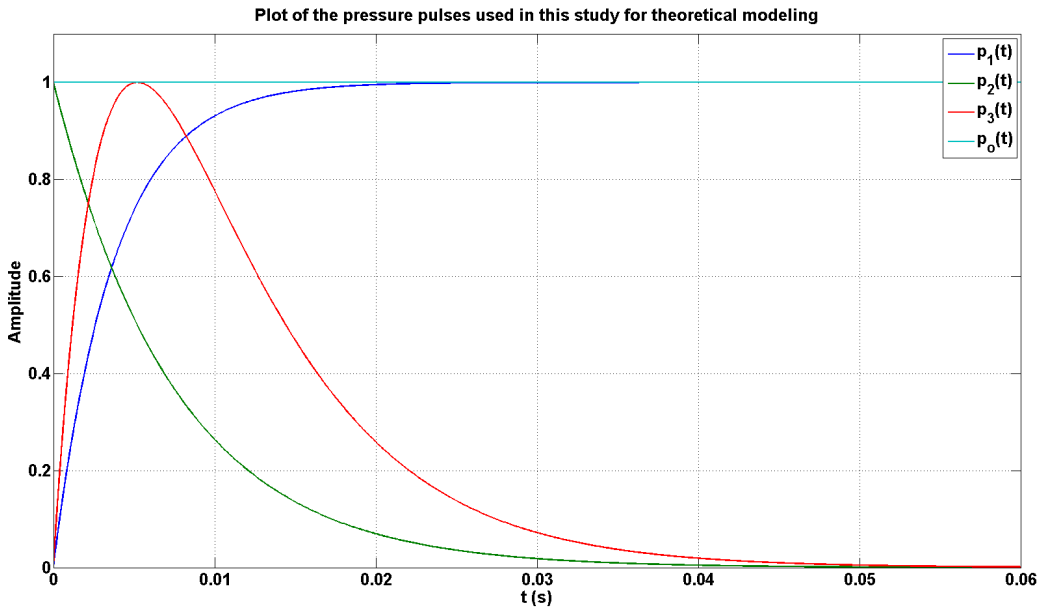

Figure 2.2: Plot of the pressure pulses that were used for the theoretical modeling in this study. All of the pulses were normalized to one for the purposes of simplicity.

2.2 The Choice of Pressure Pulse

The choice of pressure pulse plays an important role in the theoretical predictions made by the SHCM. Note that the pressure pulses used here were completely arbitrary, and that any pulse can be used to obtain a particle displacement. However, in order for the SHCM to be able to accurately make predictions about dynamite data obtained in the field, a pressure pulse that follows what might be expected from a dynamite explosion should be used. The pressure pulses used in this study are:

$$p_1(t) = p_o(1 - e^{-\sqrt{2}\omega t}), \tag{2.18}$$

$$p_2(t) = p_o e^{-\omega t/\sqrt{2}}, \tag{2.19}$$

$$p_3(t) = N p_o \left(e^{-\omega t/\sqrt{2}} - e^{-\sqrt{2}\omega t}\right), \tag{2.20}$$

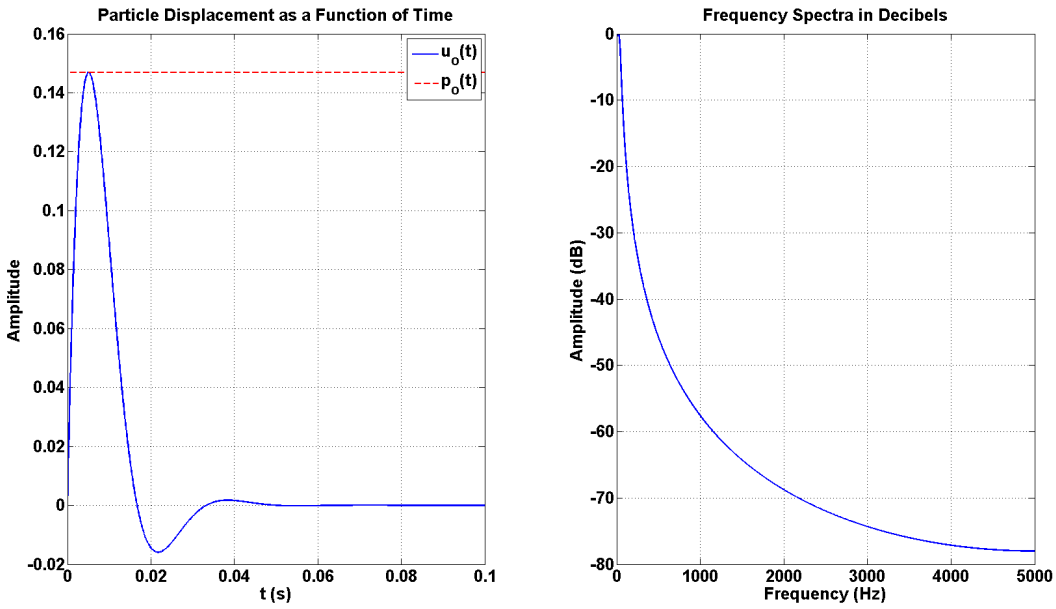

Figure 2.3: A plot of the particle displacement that results from a unit pressure pulse in the SHCM, and its corresponding frequency spectra. This particle displacement is the one used in Equation 2.17 to obtain other displacements using an arbitrary pressure pulse. Note that the amplitude of p_o has been scaled down for plotting purposes.

where ω is the angular frequency found in Equation 2.15, and N is a factor used to normalize the maximum pressure to one. Plots of these pressure pulses can be seen in Figure 2.2.

Figures 2.3 through 2.6 shows a series of particle displacement $u(t)$ and their corresponding frequency spectra that were computed using Equations 2.16 and 2.17, along with the pressure pulses given in Equations 2.18 through 2.20. The variables used in these calculations were

$$R = 100\ m, \tag{2.21}$$

$$\mu = 1\ N/m, \tag{2.22}$$

$$v_p = 2000\ m/s, \tag{2.23}$$

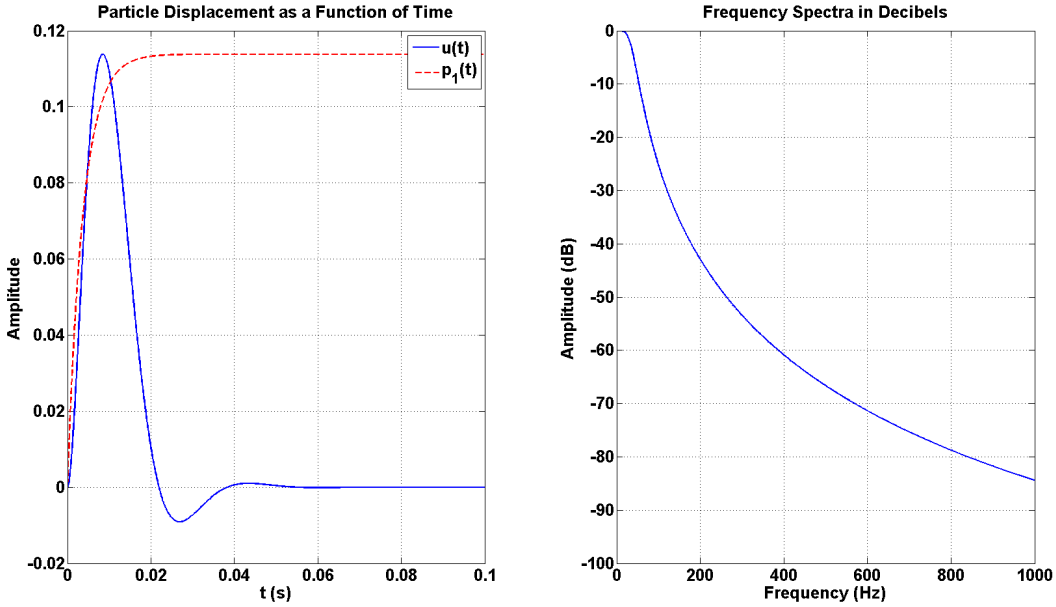

Figure 2.4: A plot of the particle displacement that is obtained from the pressure pulse $p(t) = p_o(1 - e^{-\sqrt{2}\omega t})$, along with its corresponding frequency spectra.

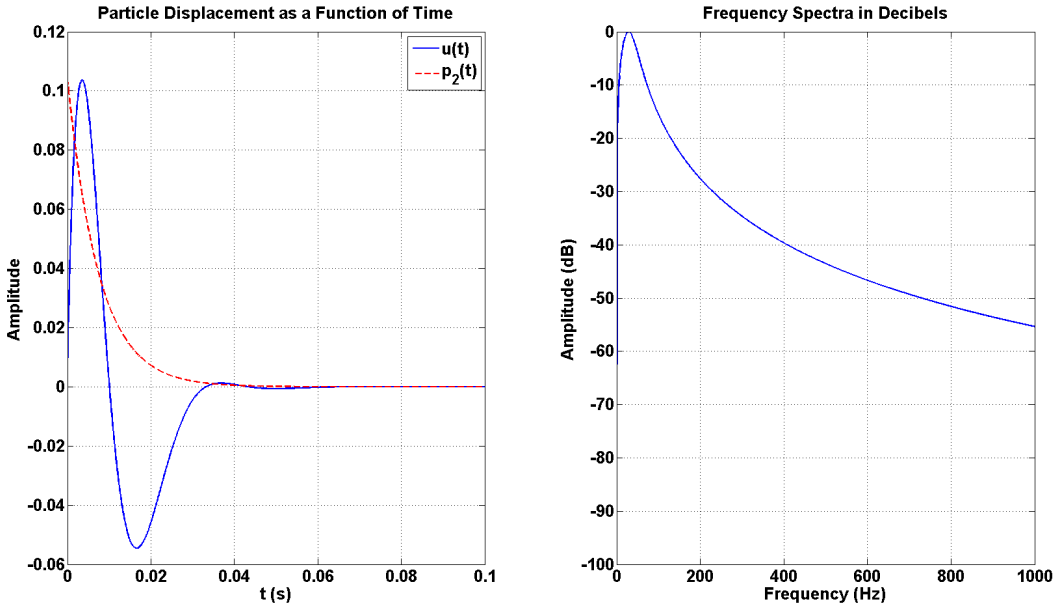

Figure 2.5: A plot of the particle displacement that is obtained from the pressure pulse $p(t) = p_o e^{-\omega t/\sqrt{2}}$, along with its corresponding frequency spectra.

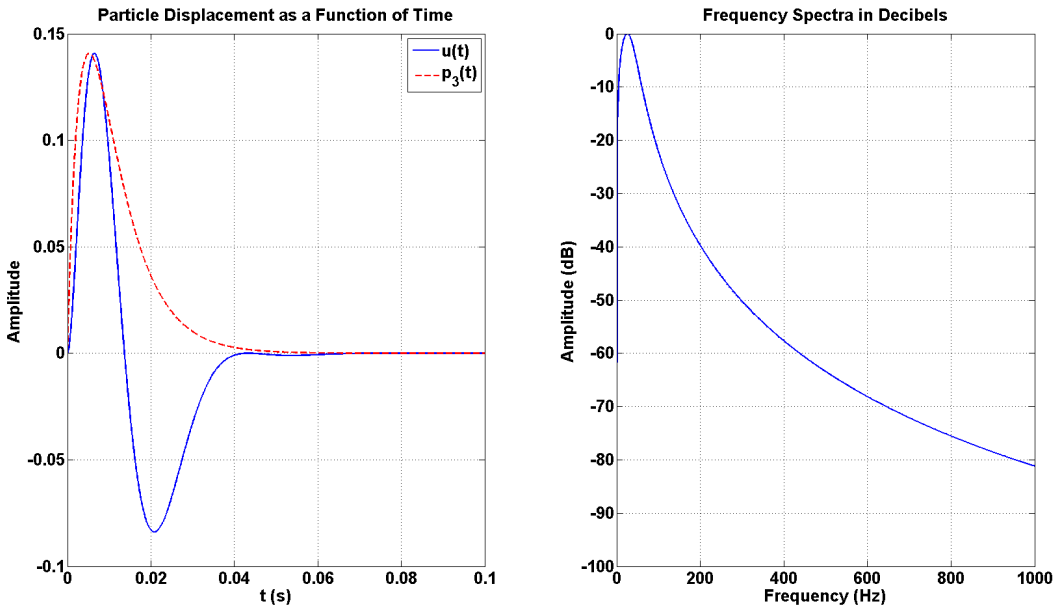

Figure 2.6: A plot of the particle displacement that is obtained from the pressure pulse $p(t) = Np_o(e^{-\omega t/\sqrt{2}} - e^{-\sqrt{2}\omega t})$, along with its corresponding frequency spectra. Note that in this particular case, the variable N is just a normalization factor that adjusts the magnitude of $p(t)$ such that its maximum value is that of p_o.

$$v_s = 1000 \ m/s. \tag{2.24}$$

Examination of each of these figures shows that the choice of pressure pulse plays a significant role in both the particle displacement, as well as the overall form of the frequency spectra. Note that in Figures 2.3 and 2.4 there is no low frequency roll-off in the lower end of the spectrum, while there is a clear roll-off in the spectra of Figures 2.5 and 2.6. The choice of pressure pulse clearly determines the overall form of the predicted frequency spectra, and in order to accurately model explosions using the SHCM, a pulse must be chosen that produces similar features to data that has been measured in the field. If we wish to observe the behavior of the dominant frequency with varying cavity radii, and thus charge sizes, we have to assign a pressure pulse to the SHCM that has a low frequency roll-off since that is a feature of the frequency spectra that is commonly observed in practice (Sharpe, 1942).

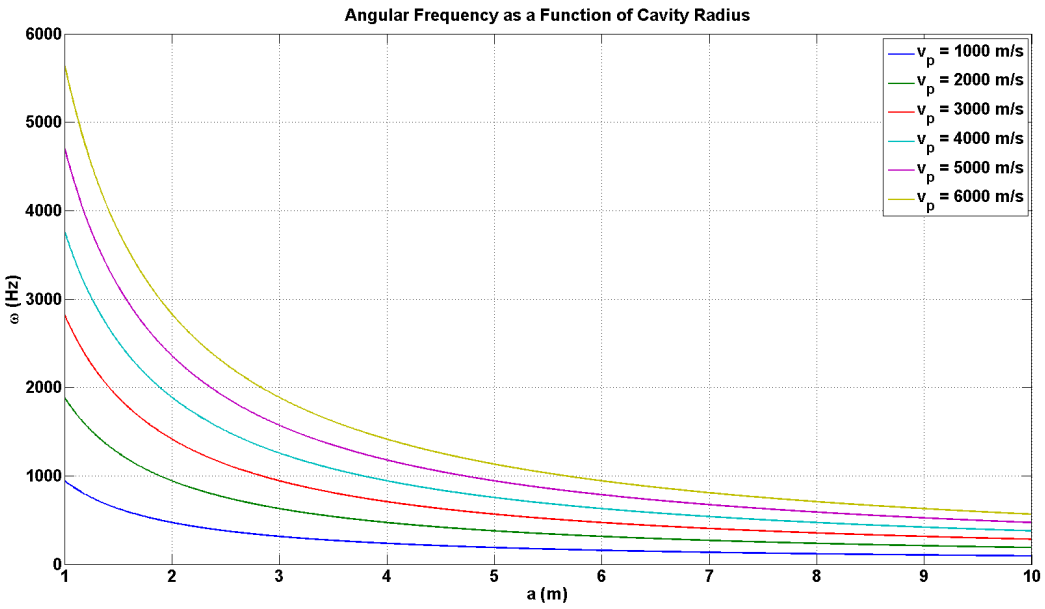

Figure 2.7: Variation of the angular frequency with cavity radii and P-wave speed, this is the same frequency given by Equation 2.15. Note that there is an overall higher frequency content for larger P-wave speeds, and that the frequency appears to taper off near higher values of cavity radius.

2.3 The Role of the Cavity Radius

Careful examination of both Equations 2.16 and 2.15 reveals that the cavity radius plays a very important role in the SHCM, specifically in the prediction of the overall frequency content of the particle displacement. Figure 2.7 contains a plot of the angular frequency, given in Equation 2.15, as a function of varying radii for several different P-wave speeds. There is an apparent increase with overall amplitude response with increased p-wave speeds, which suggests that higher velocity mediums should produce a higher amplitude response. Additionally, the amplitude response for all velocities tapers off near the higher a-values, which suggests that smaller cavities, and thus smaller explosions, should display a greater variation in frequency content than that of larger chargers.

Figure 2.8 depicts a series of particle displacements for varying cavity radii that were computed using Equations 2.16 and 2.17. Note that the pressure pulse used to compute

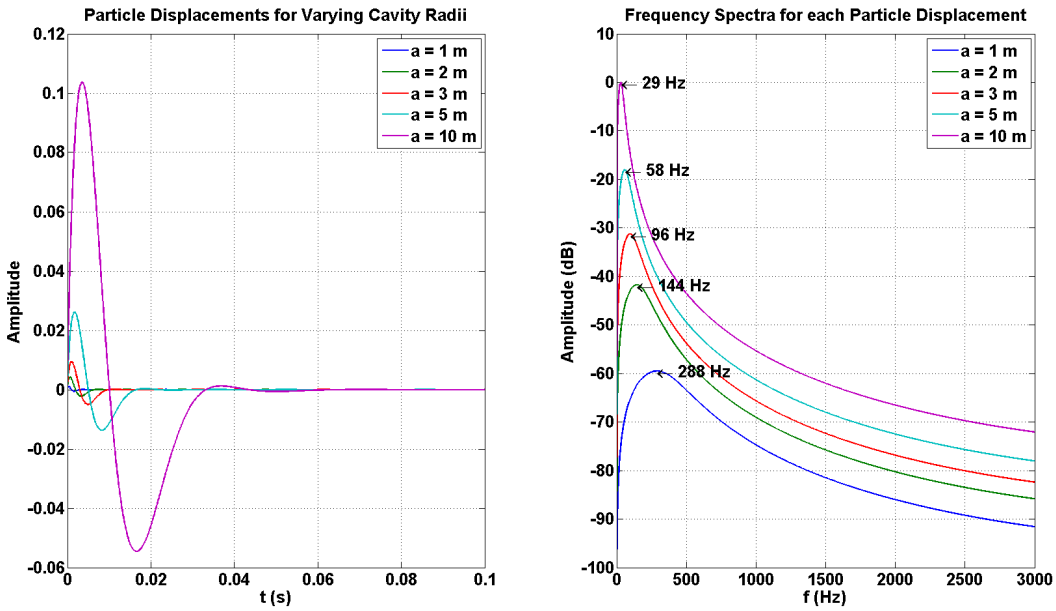

Figure 2.8: Particle displacements for varying cavity radii along with their corresponding frequency spectra. Observation of the frequency spectra shows a increase in the overall amplitude response with increased charge size, however, there is a noticeable decrease in the dominant frequency when chrage size is increased.

these displacements was $p_3(t)$ found in Equation 2.20. There is a clear increase in the overall frequency content with larger cavities, however, there is a significant decrease in the dominant frequency with increased cavity size. This suggests that if the SHCM can be used to make predictions about the frequency content of dynamite data obtained in practice, that we should see an overall decrease in measured dominant frequency for larger charges. Additionally, in each of the plots shown in Figure 2.8, there is a low-frequency roll-off present for all cavity radii. If in fact the SHCM can be used to make predictions about dynamite data obtained in the field, we should also see this low-frequency roll-off when we obtain frequency spectra for real dynamite data. Figure 2.8 also offers some insight into another potential limitation with using smaller charges. Even though the dominant frequency increases with smaller charge sizes, there is significant decrease in the overall amplitude response. This can be very problematic when acquiring data since more power is often desired to better image the subsurface. Therefore, choosing charge sizes based on the predictions of the SHCM could

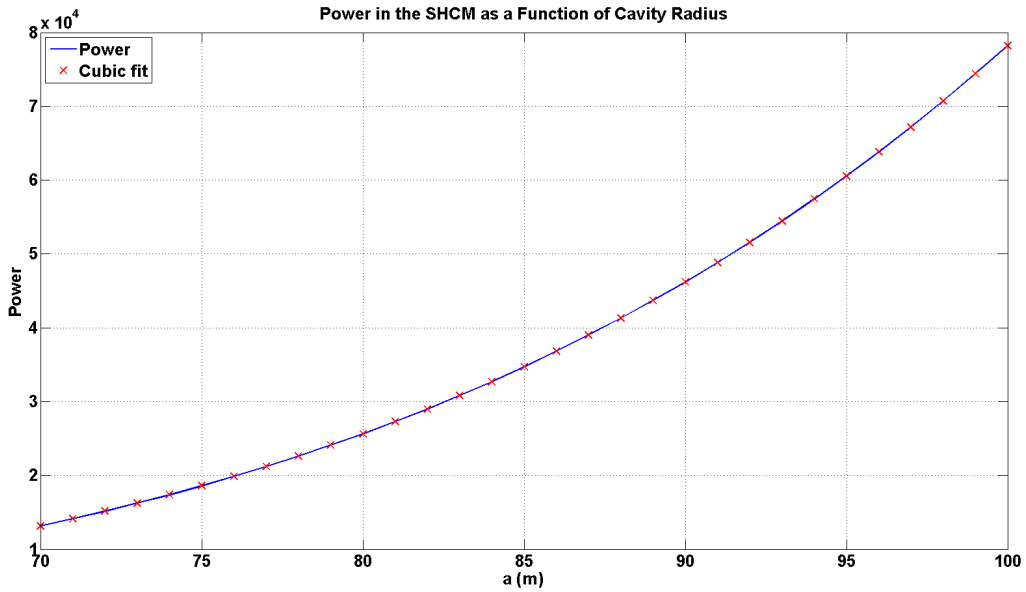

Figure 2.9: Plot of the shot power in the SHCM as a function of the cavity radius. Initial observation of the shot power reveals a potential cubic relationship between power and cavity radii in the SHCM. The red line shows a cubic fit of power and cavity radius, which does appear to be a good fit to the original plot. This suggests that the relationship between shot power and cavity radius may be cubic in the SHCM.

be a balancing act between the desired dominant frequency and power.

The power of particle displacement is directly affected by the size of the cavity in the SHCM (Sharpe, 1942). Figure 2.9 shows a plot of the total power of $u(t)$, calculated using Equations 2.16 and 2.17, as a function of the cavity radius a. Initial observations of this plot reveals a potential cubic relationship between power and cavity radius in the SHCM. Figure 2.10 shows a plot of this same power as a function of the cube of the cavity radius. For larger values of a, the plot appears to be linear, which suggests that there is a cubic relationship between power and cavity radius in the SHCM.

2.4 Application of the SHCM to Data Obtained in the Field

Based on these observations, there are several key features of a measured frequency spectra that need to be observed to verify the viability of the SHCM in making predictions about

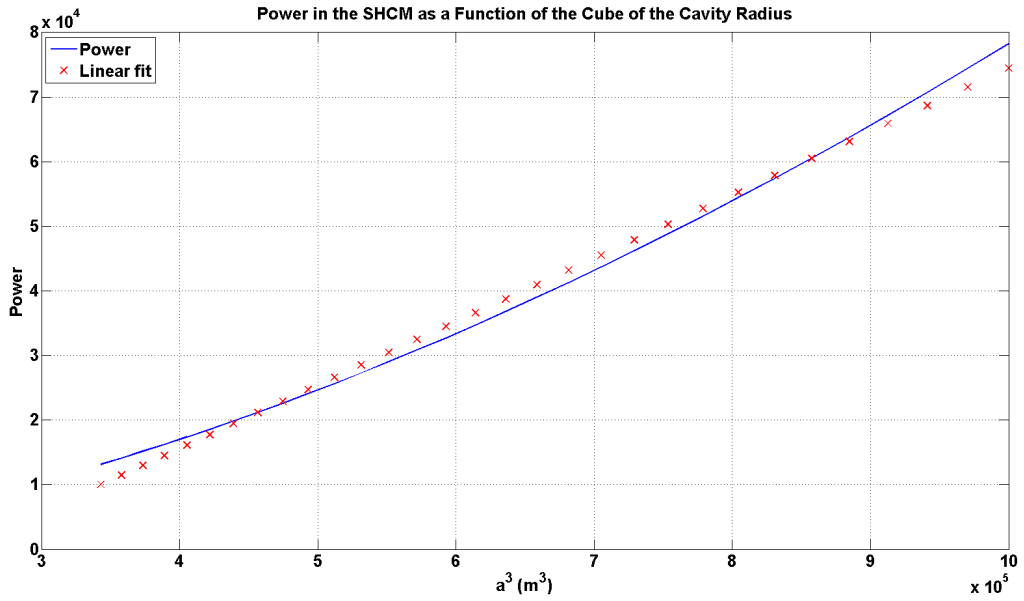

Figure 2.10: Plot of shot power in the SHCM as a function of the cube of the cavity radius. This plot appears to be mostly linear in behavior for larger values of the cavity radius, which suggests that the relationship between power and cavity radius in the SHCM is cubic.

dynamite data that we obtain in the field. These features include:

1. An increase in the overall frequency content with larger charge sizes
2. A decrease in the dominant frequency with larger charge sizes
3. Larger particle displacements with increased charge size
4. The presence of a low-frequency roll-off in the measured spectra

If we can observe these features in data collected in the field, we may be able to use the SHCM to predict critical features of waves emitted by an explosive source. Additionally, if a relationship between the charge size and the shot power can be determined, it may be possible to determine a relationship between charge size and cavity radius. This is based on the observations of the behavior of power and cavity radius in Figures 2.9 and 2.10.

There are several approximations made in this model that may not be realistic for dynamite employed in the field, which could prove to be a limitation of this model. One of

the major assumptions of the SHCM is that the pressure pulse is contained entirely within the cavity, and that it acts uniformly over the cavity's interior. Fluid-filled boreholes are generally used to place charges in the subsurface, which presents a significant limitation for Sharpe's model based on the assumptions that were made when deriving the model. A fluid-filled borehole creates a scenario where a narrow column with different parameters than that of the subsurface surrounding it has been introduced to the geometry of the problem. Therefore, the pressure pulse may not be as evenly distributed around the source as the SHCM assumes. This could present a problem for the SHCM if the energy that travels up the borehole is substantial, since this configuration deviates significantly from the spherical hollow cavity approximation.

2.5 Chapter Summary

- The SHCM predicts that larger cavity radii, and thus larger charge sizes, should produce higher amplitude waves than that of smaller cavity radii.
- The SHCM predicts a decrease in dominant frequency with larger charge sizes.
- In order to accurately represent the energy from an explosive source, an appropriate source activation pressure pulse must be ascribed to the model.
- A low-frequency roll-off must be present in the data according to our implementation of the SHCM.
- The relationship between power and cavity radius is cubic in the SHCM.

Chapter 3

Gaussian Ball Source Model

3.1 Theory and Derivation

The Gaussian Ball Source Model (GBSM) operates under the assumption that any explosion can be considered a body source of seismic waves. This means that the explosive source can be represented as a very large amount of energy being rapidly deposited into the subsurface (Aldridge, 2011). If the medium can support elastic wave propagation, elastic waves will emanate from the point in which the energy was deposited. In this model there is no assumption of an "equivalent cavity" in which wave propagation behaves in a nonlinear fashion, however, it is still a far-field approximation and does not necessarily work when dealing with waves that are close to the source (Aldridge, 2011). Similar to the SHCM, this model also assumes a homogeneous medium.

A graphical depiction of the GBSM has been shown in Figure 3.1, and is very similar to the SHCM in terms of particle motion. The center of the source represents the region in space where a large amount of energy, which in this case is represented as a pressure pulse $p(t)$, is deposited into the subsurface instantaneously. If this is modeled in a region that can support elastic wave propagation, elastic waves emanate from the source and propagate radially outwards from the source.

Aldridge has covered the derivation of this model in great detail in his 2011 report, so we will only outline the derivation here (Aldridge, 2011). The set of partial differential equations that govern this model are as follows:

$$\frac{\partial v_i}{\partial t} - \frac{1}{\rho}\frac{\partial \sigma_{ij}}{\partial x_j} = \frac{1}{\rho}\left(f_i + \frac{\partial m_{ij}^a}{\partial x_j}\right), \tag{3.1}$$

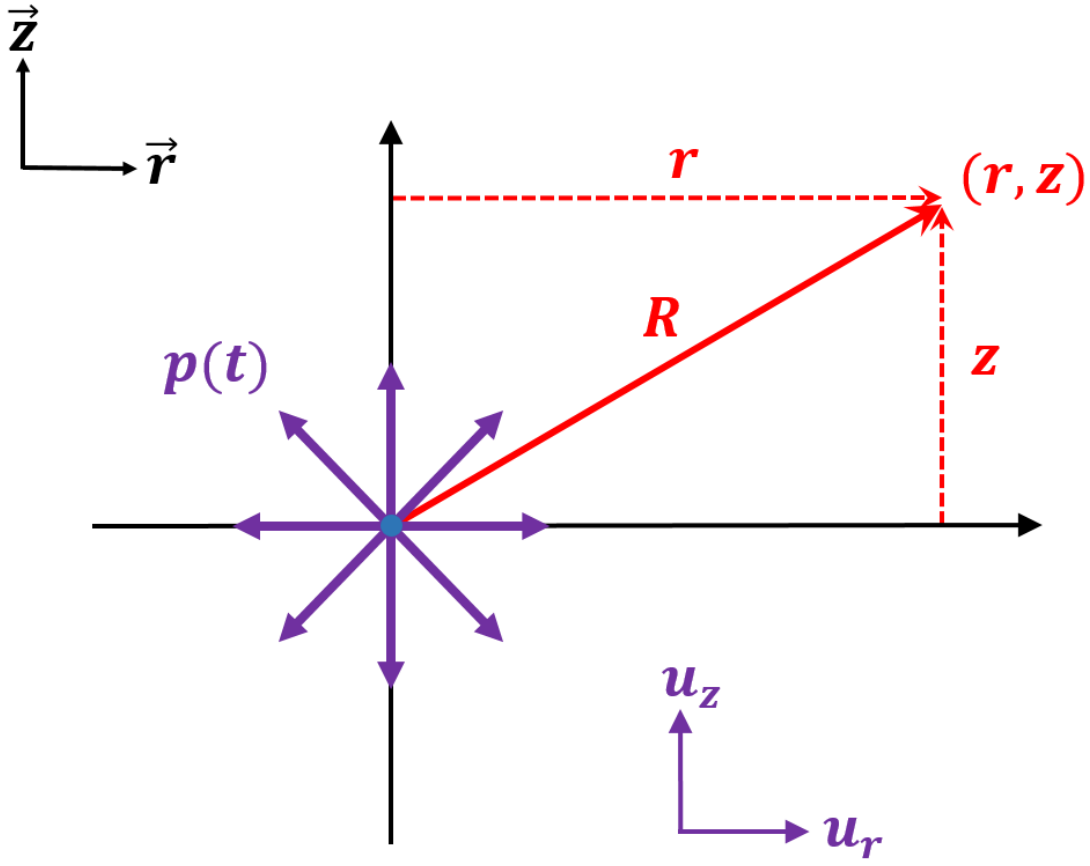

Figure 3.1: Graphical depiction of the Gaussian Ball Source Model. The point source (shown in blue) represents the region in space where a large amount of energy, represented in the form of a pressure pulse $p(t)$, is deposited into its surroundings instantaneously. This results in the emanation of elastic waves, which propagate radially outward from the source.

$$\frac{\partial \sigma_{ij}}{\partial t} - \lambda \frac{\partial v_k}{\partial x_k}\delta_{ij} - \mu\left(\frac{\partial v_i}{\partial x_j} + \frac{\partial v_j}{\partial x_i}\right) = \frac{\partial m_{ij}^s}{\partial t}, \tag{3.2}$$

where v_i is the particle velocity vector, σ_{ij} is the stress tensor, δ_{ij} is the Kronecker delta, ρ is the density of the medium, λ and μ are the Lamé parameters of the subsurface, f_i is the force density vector, and m_{ij} is the moment density tensor. Note that the terms a and s in the above equations are used to denote asymmetric and the symmetric parts of the equations respectively. Since this model assumes that a very large portion of energy is deposited instantaneously into the subsurface, a delta function is used as the moment tensor (Aldridge, 2011). This moment tesnor is given as:

$$m_{ij}(\mathbf{x}, t) = -M d_{ij} w(t) \delta\left(\mathbf{x} - \mathbf{x}_s\right), \tag{3.3}$$

where M is a magnitude scalar, d_{ij} is a dimensionless orientation tensor, and $w(t)$ is an arbitrary source activation waveform. In general, a Gaussian function in mathematics is a function of the form:

$$f(x) = A\ exp\left(-\frac{(x-B)^2}{C^2}\right), \tag{3.4}$$

where A, B, and C are constants that adjust the amplitude, position, and width of the Gaussian function respectively. Figure 3.2 shows a series of Gaussian functions that were obtained using Equation 3.4 with varying values of the constants A, B, and C. In a Gaussian function, the constant leading the exponential (A in this case) adjusts the amplitude of the function, the constant inside the square in the numerator (B in this case) shifts the position of the peak, and constant in the denominator (C in this case) adjusts the width of the Gaussian function. Aldridge suggests a moment tensor of the form

$$m_{ij}(\mathbf{x}, t) = -M\left(\frac{\delta_{ij}}{\sqrt{3}}\right)\ w(t)\ \frac{1}{h^3}\ exp\left(-\pi\left(\frac{\mathbf{x} - \mathbf{x}_s}{h}\right)^2\right), \tag{3.5}$$

where $w(t)$ is an arbitrary waveform, $\mathbf{x(s)}$ is the position of the source, and h is a term referred to as the "Gaussian Width Parameter" given in meters (Aldridge, 2011). Also note that in this case the orientation tensor d_{ij} has been replaced by the term $\delta_{ij}/\sqrt{3}$, where

δ_{ij} is the Kronecker delta function, and $\sqrt{3}$ is a normalization term that implies that there are three mutually exclusive force dipoles of equal magnitude, which represents an explosion (Aldridge, 2011). We can rearrange Equation 3.5 to get an expression of the form

$$m_{ij}(\mathbf{x},t) = -\delta_{ij}\ w(t)\ \frac{M}{\sqrt{3}h^3}\ exp\left(-\pi\left(\frac{\mathbf{x}-\mathbf{x}_s}{h}\right)^2\right). \tag{3.6}$$

The Kronecker delta δ_{ij} will only be nonzero when $i = j$, which only occurs along the diagonals of the moment tensor. If we compare Equations 3.4 and 3.6, we can see that the diagonal terms of the moment tensor is a source activation waveform $w(t)$, multiplied by a Gaussian function of amplitude $M/\sqrt{3}h^3$, centered on $\mathbf{x}_s$, and with width h. Substituting the moment tensor from Equation 3.6 into Equations 3.1 and 3.2 and solving for the pressure, results in the expression:

$$p(R,t) = \frac{M\,(1-4\gamma^2/3)}{4\pi\alpha^2 R} w(t), \tag{3.7}$$

where α is the P-wave speed in the medium in meters per second, γ is the ratio of P- to S-wave speeds, R is the radial distance in meters from the point source to point of observation as shown in Figure 3.1, M is the magnitude scalar in Joules, $w(t)$ is the source activation waveform, and $p(R,t)$ is the pressure pulse in the GBSM. The GBSM is characterized by a "Gaussian explosion filter", which is given by Aldridge as

$$g(R,t;h,\alpha) = \frac{\alpha}{h} H\left(t+\frac{R}{\alpha}\right)\left[exp\left(-\pi\left(\frac{\alpha t}{h}\right)^2\right) - exp\left(-\pi\left(\frac{\alpha(t+2R/\alpha^2)}{h}\right)^2\right)\right], \tag{3.8}$$

where $H(t + R/\alpha)$ is Heaviside unit step function. Finally, the pressure at any point of observation in the GBSM is a convolution of the pressure found in Equation 3.7, and the Gaussian explosion filter given in Equation 3.8. This is expressed mathematically as

$$p_G(R,t) = p(R,t) * g(R,t;h,\alpha), \tag{3.9}$$

where $p_G(t)$ is the pressure at the point of observation in the GBSM, $p(r,t)$ is the pressure pulse at the source, and $g(r,t;h,\alpha)$ is the Gaussian explosion filter. Note that in Equation 3.9, both p and g depend on R and t terms. When the convolution is carried out here, it is

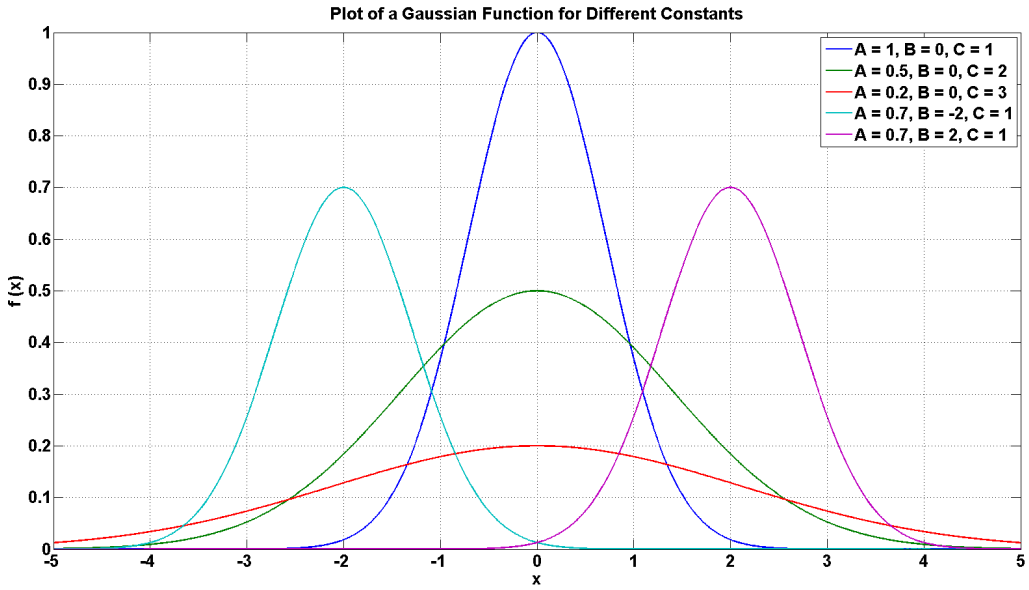

Figure 3.2: A plot of various Gaussian functions obtained using Equation 3.4. The constant A scales the amplitude of the Gaussian, the constant B shifts the position of the peak, and the constant C adjust its width.

over time. We are most interested in computing the value of $p_G(t)$ in this model, as that is what was used to model the amplitude and frequency response of charges employed in the field.

3.2 The Choice of Pressure Pulse and Gaussian Ball Width

Figure 3.3 shows a Gaussian pressure pulse that was obtained using Equation 3.7, where pressure pulse $p_3(t)$ from Equation 2.20 was used for the activation waveform $w(t)$. Note that all applicable parameters from Equation 2.21 through 2.24, and a magnitude of $M = 1$ were used in the following calculations. After a pressure pulse for $p(R, t)$ has been established in Equation 3.9, a Gaussian explosion filter $g(R, t; h, \alpha)$ can be used to compute $p_G(R, t)$. Figure 3.4 shows a series of Gaussian explosion filters with varying values of the width parameter h, and Figure 3.5 shows the Gaussian pressures $p_G(R, t)$ that result via convolution of these filters with the pressure pulse $p(R, t)$, as per Equation 3.9 and Figure 3.3. Essentially, the

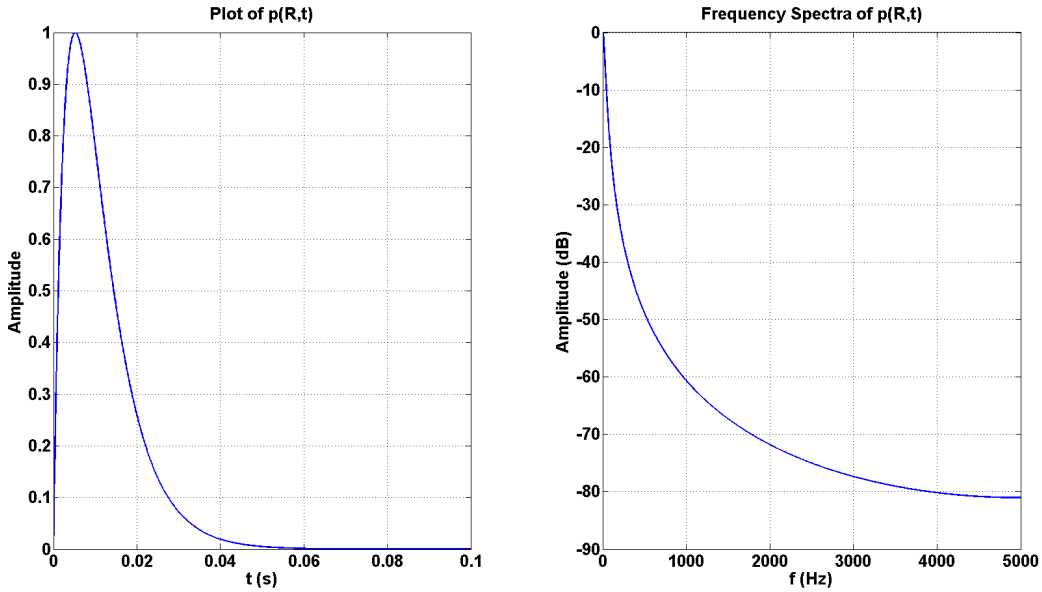

Figure 3.3: A plot of the Gaussian pulse using $p_3(t)$ in Equation 3.7 for $w(t)$. Note that this is the same pulse that was used in both the SHCM and HCM to compute the particle displacements and frequency spectra.

plots in Figure 3.5 were obtained via convolution of the pulse in Figure 3.3 with the Gaussian Balls in Figure 3.4.

Examination of Figures 3.3 through 3.5 reveals several key features of the GBSM. The width of the Gaussian explosion filter in Equation 3.8 determines the width of the Guassian pressures obtained via Equation 3.9. Figures 3.8 and 3.5 shows that the width of the obtained Gaussian pressures is inversely proportional to the width of the Gaussian ball filters, since expanding in the time domain results in shrinking in the frequency domain. From these figures, it is also apparent that the amplitude of the resulting Gaussian pressures, is directly proportional to that of the Gaussian filters, and thus higher amplitude Gaussian filters should produce higher amplitude Gaussian pressures.

For the purposes of modeling real data, it would be useful to be able to observe the behavior of the dominant frequency when we alter both the magnitude and width of the Gaussian explosion filter shown in Equation 3.8. Observation of Figures 3.3 and 3.5 reveals a potential limitation of pressure pulse $p_3(t)$ that we used in the SHCM and HCM. There

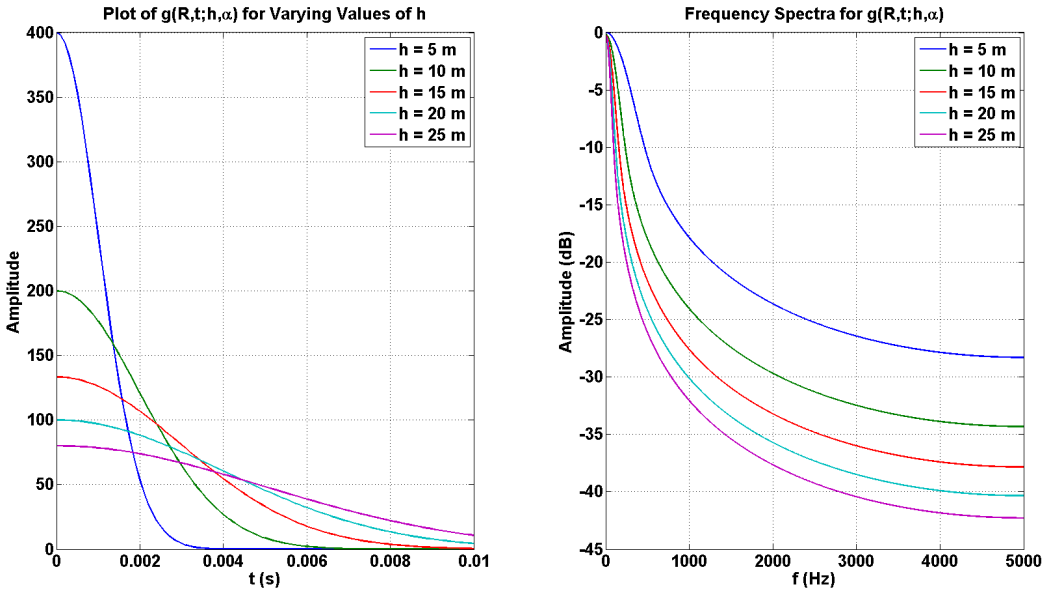

Figure 3.4: A plot of the Gaussian explosion filters with varying Gaussian width parameter h, as per Equation 3.8. Note that as the width of the ball increases, the amplitude decreases and the Gaussian begins to expand. An increased width parameter expands the width of the Gaussian, but in the case of Equation 3.8, the amplitude of the filer is inversely proportional to h, and thus the amplitude decreases for wider Gaussian explosion filters.

does not appear to be a low frequency roll-off in the Gaussian pressures of Figure 3.5, which could pose a problem when modeling dynamite explosions. It is therefore necessary to utilize a different pressure pulse in the GBSM if we wish to observe any sort of variation in dominant frequency when we change the parameters of this model. In the frequency domain, Equation 3.9 can be expressed as

$$\hat{p}_G(R,\omega) = \hat{p}(R,\omega)\hat{g}(R,\omega;h,\alpha). \tag{3.10}$$

In the frequency domain, the spectra of the Gaussian pressures is the product of the spectra of the pressure pulse and the Gaussian explosion filter. Figures 3.6 through 3.8 shows a series of pulses that were obtained using the same calculations performed previously, but using a different source activation waveform $w(t)$. Note that all of the other parameters used previously were maintained in these calculations. Figure 3.6 shows the pulse $p_3(t)$ as the source activation waveform $w(t)$ in Equation 3.7, Figure 3.7 shows a Ricker wavelet of

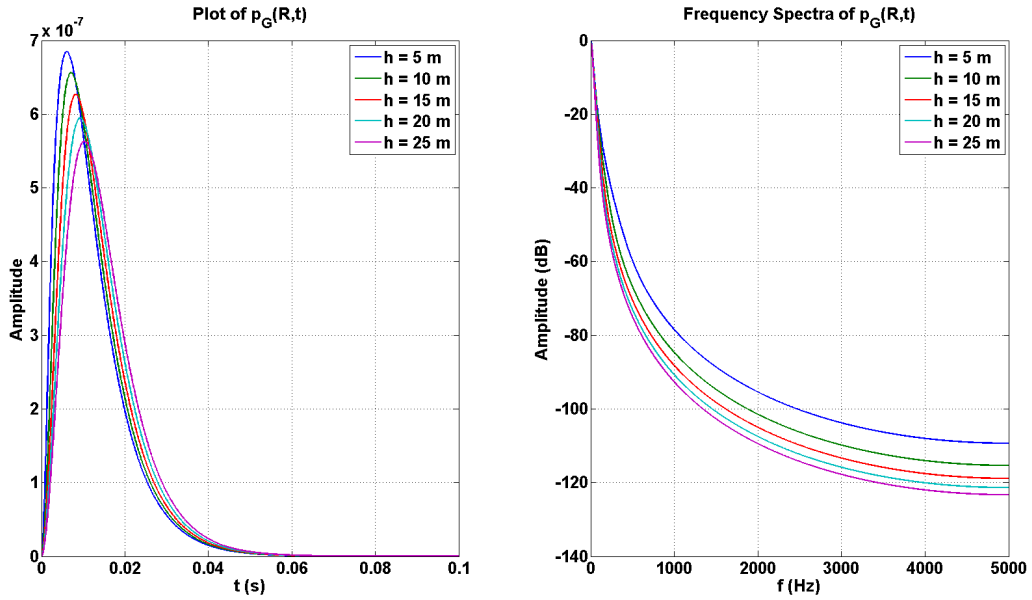

Figure 3.5: A plot of the Gaussian pressures obtained via convolution of the pressure pulse in Figure 3.3 with the Gaussian explosion filters in Figure 3.4, using Equation 3.9. The resulting pressures in the GBSM are modulated by the Gaussian explosion filters, and thus the width of the resulting pressures are determined by the width of the Gaussian explosion filters. Since widening in the time domain becomes shrinking in the frequency domain, the width of the Gaussian pressure is inversely proportional to width of the Gaussian explosion filter. Also note that the amplitude of the Gaussian explosion filter determines the amplitude of the Gaussian pressures as well.

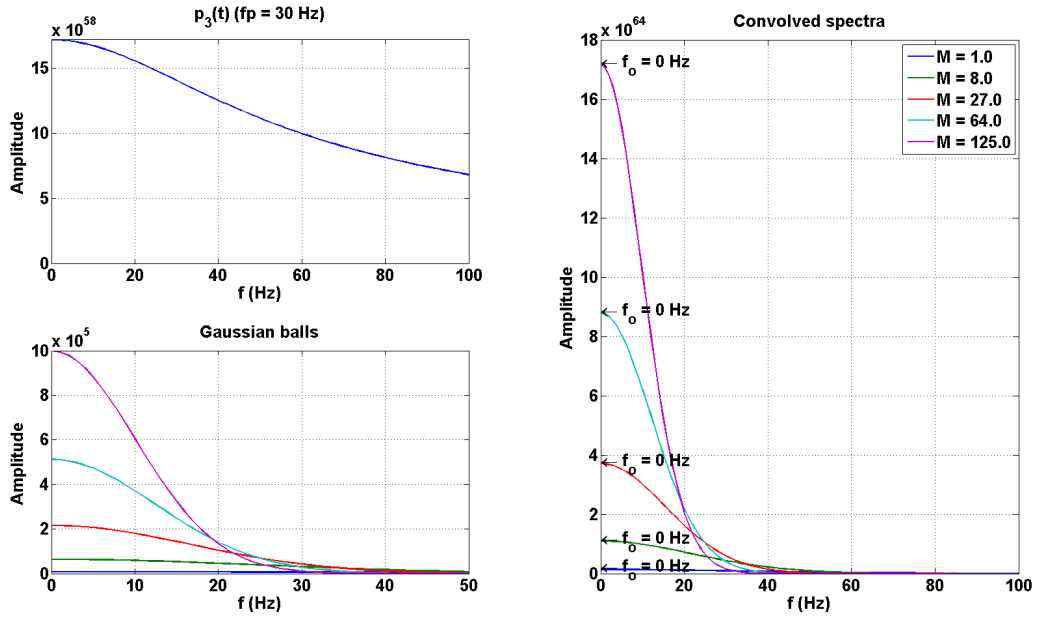

Figure 3.6: Plot of the Gaussian pressures obtained using $p_3(t)$ as the source activation waveform $w(t)$ in Equation 3.7. Note the fact that the resulting frequency spectra of the Gaussian pressures do not contain any sort of low frequency roll-off, which could prove to be a significant limitation of $p_3(t)$ in this particular model as we are interested in observing changes in the dominant frequency when we alter the parameters of this model.

dominant frequency $30Hz$ used for $w(t)$, and Figure 3.8 shows a minimum phase wavelet of dominant frequency $30Hz$ used for $w(t)$. Both the Ricker wavelet and the minimum phase wavelet display a low frequency roll-off in their resulting frequency spectra, which suggests that they may be a better candidate for the source activation waveform $w(t)$ used in this study.

The behavior of the dominant frequency in Figures 3.7 and 3.8 suggests that there are some very distinct similarities between the SHCM and the GBSM. In the SHCM we observed that as the size of the cavity was increased the resulting amplitudes of the particle displacement increased, but the dominant frequency decreased. In the GBSM we were only able to observe this effect if we used the assumption that the magnitude M in Equation 3.7 is related to the width parameter h via a cubic relationship

$$M = C\ h^3 \tag{3.11}$$

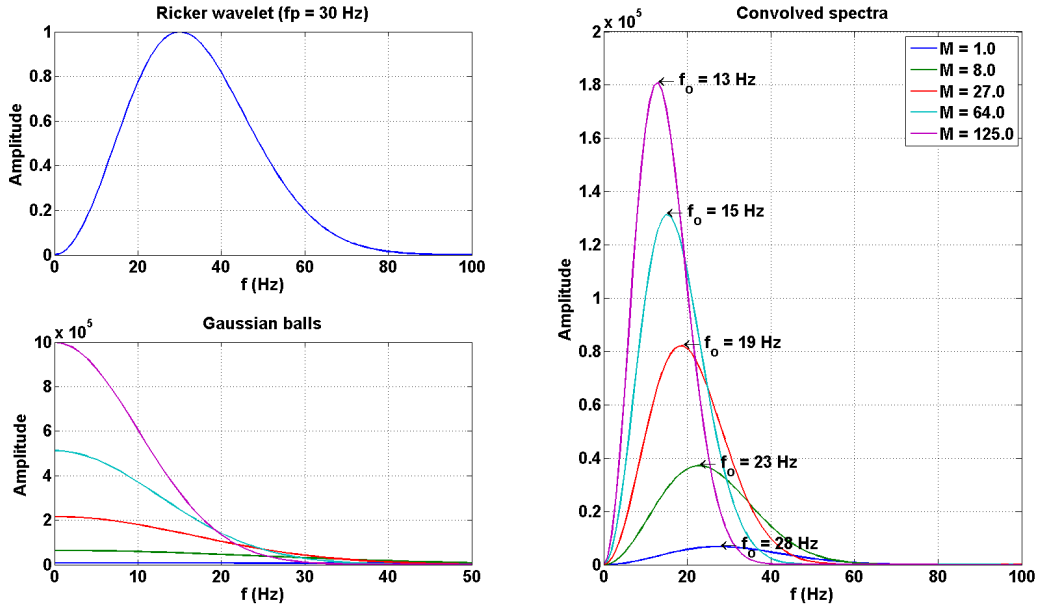

Figure 3.7: Plot of the Gaussian pressures obtained using a Ricker wavelet with a dominant frequency of $30Hz$ as the source activation waveform $w(t)$ in Equation 3.7. This pressure pulse results in a low frequency roll-off in the frequency spectra, which suggests that this is a good choice of pressure pulse if we wish to observe the behavior of the dominant frequency with changing parameters in the GBSM.

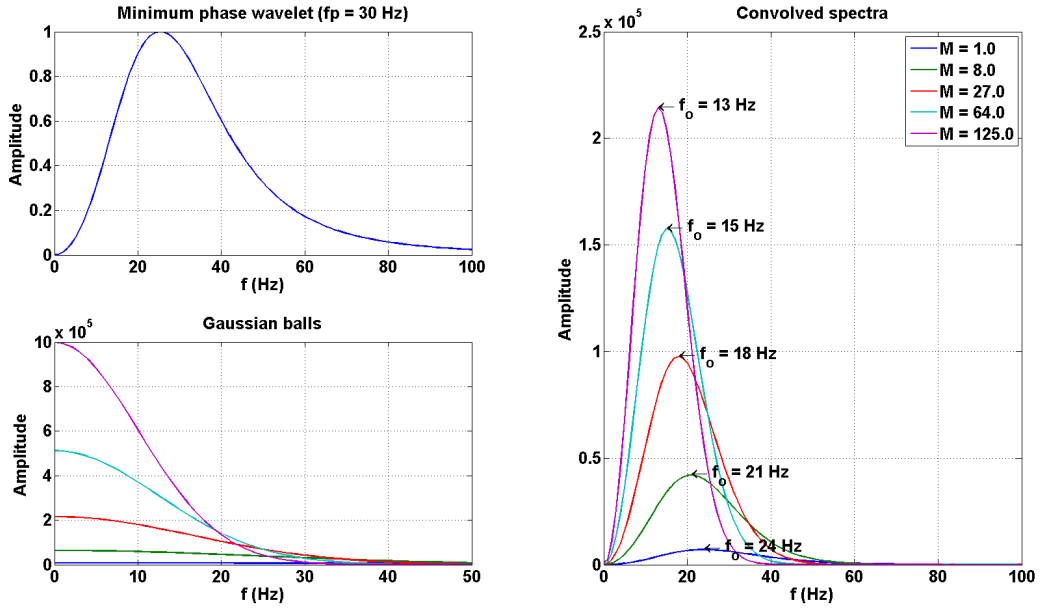

Figure 3.8: Plot of the Gaussian pressures obtained using minimum phase wavelet with a dominant frequency of $30Hz$ as the source activation waveform $w(t)$ in Equation 3.7. This pressure pulse results in a low frequency roll-off in the frequency spectra, which suggests that this is also good choice of pressure pulse if we wish to observe the behavior of the dominant frequency with changing parameters in the GBSM.

where C is a proportionality constant with units of $1/m^3$ such that M remains unitless. The frequency spectra shown in Figures 3.7 and 3.8, were obtained using the M and h shown in the previous equation for a C value of 1 m^{-3}, in Equations 3.7 through 3.9. If we did not use this parameterization of the magnitude in terms of the Gaussian ball width, we did not observe this decrease in dominant frequency with larger ball widths. This suggests that in order match the GBSM with data obtained from dynamite in practice, we may have to assume the relationship between cavity ball width and magnitude shown in Equation 3.11. The assumption made here does not seem to be unreasonable, as this relationship states that the explosive potential of dynamite is directly proportional to the volume of the charge. Observation of these results suggests that we should expect to see similar amplitude and frequency effects in the GBSM, as we did in the SHCM.

3.3 Power Distribution in the GBSM

Figures 3.9 and 3.10 shows the power variation in $p_G(R,t)$ in Equation 3.9 as a result of varying ball widths h. Note that for these power computations, we assumed that the relationship between M and h was that of Equation 3.11. The results of these computations shows a cubic relationship between the power of $p_G(R,t)$ and the width parameter h, and a linear relationship between $p_G(R,t)$ and the cube of the width parameter. This is very similar to what we observed in the SHCM, and therefore if we assume that the charge size is related to the Gaussian width parameter and magnitude, we may be able to establish a link between the size of the charge and the width parameter.

3.4 Application of the GBSM to Data Obtained in the Field

There are three main criterion that we must observe in real data to ensure that the GBSM can be used to effectively make predictions.

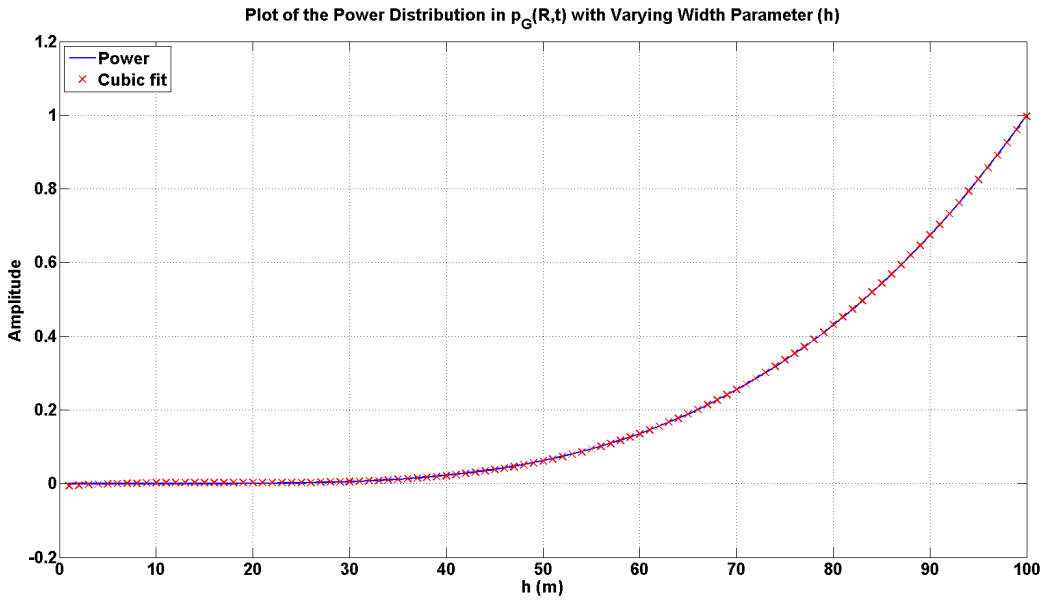

Figure 3.9: A plot of the power spectra resulting from the GBSM as a function of the ball width h. In this figure, we can see that there is a cubic relationship between power and ball width in the GBSM.

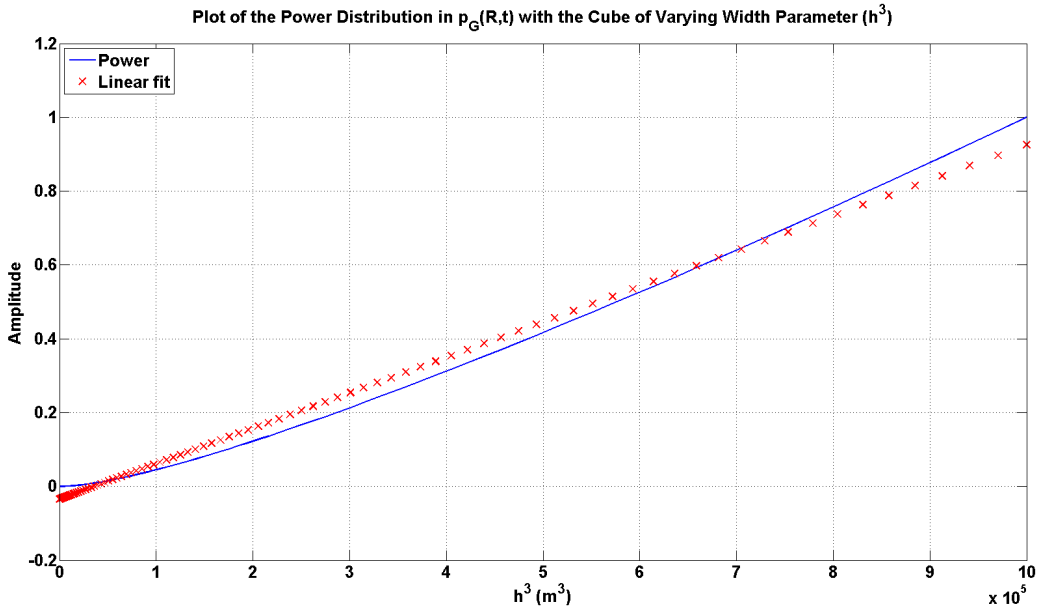

Figure 3.10: A plot of the shot power as a function of the cube of the ball width. The linear line of best fit seems to match the calculated values, which provides further evidence that the power and width relationship is cubic in the GBSM.

1. The amplitude of the particle displacements increases with charge size

2. The dominant frequency decrease with charge size

3. A low frequency roll-off is present in the data

These match the criterion of the SHCM, so in essence the models are almost identical in their expected observations.

There are several potential limitations with this model that could cause erroneous predictions in real data. This model assumes that the energy source is distributed over a 3D Gaussian ball with an intensity proportional to the Gaussian amplitude. As a result of this symmetric energy injection, only pressure waves are produced that propagate radially outward from the center of the Gaussian ball. The assumption that the waves propagate outwards in a symmetrical, radial pattern may be violated in some media. In addition to that, this model is a far-field approximation, so it may not be able to make accurate predictions for data that was collected close to the source.

3.5 Chapter Summary

- The GBSM predicts an increase in amplitude response for larger Gaussian ball widths.
- The GBSM predicts a decrease in dominant frequency with Gaussian ball width provided that the magnitude is assumed to be the cube of the ball width.
- In order to accurately model an explosive source using the GBSM, an appropriate source activation waveform must be ascribed to the model.
- The relationship between ball width and power is cubic in the GBSM.

Chapter 4

The Heelan Cylindrical Model

4.1 Theory and Derivation

One of the biggest limitations of the SHCM and GBSM models is the fact that they cannot predict the nature of S-wave propagation because they do not have the ability to produce S-waves (Sharpe, 1942). This is due largely to how the cavity is set up as a sphere in the SHCM, or the representation of the source as a Gaussian ball in the GBSM; the symmetry of the problem allows for a derived particle displacement that is independent of the angular variables, and thus there are no terms that can account for S-waves. Heelan developed a model that is very similar to the SHCM in that it contains an "equivalent cavity", however, in Heelan's Model it is a hollow cylinder instead of a sphere (Heelan, 1953). Utilization of a cylinder for the equivalent cavity allows for a derivation of the particle displacement that uses both the angular and radial terms, which can be used to account for S-waves. Heelan's model may also prove to be advantageous since a hollow cylinder more accurately represents the configuration of a charge in the subsurface, specifically the borehole that is used to set the charge in the ground.

Figure 4.1 shows a graphical depiction of the Heelan Cylindrical Model (HCM). This model assumes that an explosive source can be encapsulated by hollow cylinder of radius a and length L wherein waves emitted from the source do not propagate linearly. Similar to the SHCM, the size of this cavity is directly proportional to the size of the charge. However, in the case of the HCM, there are two independent source activation waveforms, $p(t)$ and $q(t)$, that act independently along the radial and axial components of the cylinder, resulting in a particle motion that is dependent on two different activation waveforms. The particle displacement that occurs along the radial component as a result of $p(t)$ is termed u, and the

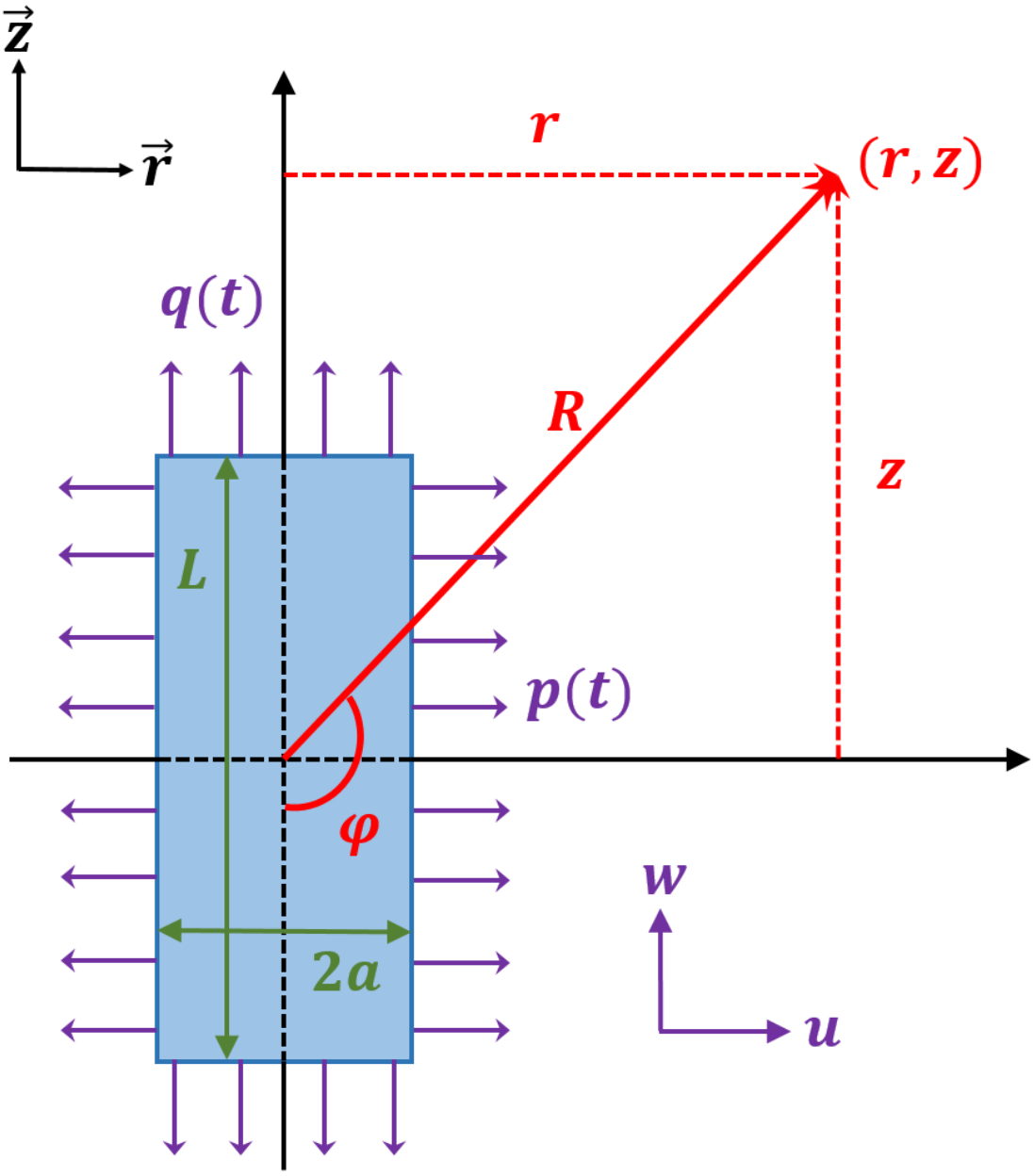

Figure 4.1: A graphical depiction of the Heelan Cylindrical Model (HCM). The equivalent cavity is a cyilinder of radius a, and length L, within which the waves are assumed to behave in a nonlinear manner. A source activation waveform $p(t)$ acts along the radial component of the cylindar, and another source activation waveform $q(t)$ acts along the axial component of the cylinder. This results in a particle displacement u along the radial component, and a particle displacement w along the axial component. Note that both $p(t)$ and $q(t)$ are assumed to be independent of each other.

particle displacement that occurs along the axial component as a result of $q(t)$ is termed w. Note that the HCM also has a third source activation waveform that acts along the angular component of the cylinder, but for the purposes of this study we will ignore it and only consider $p(t)$ and $q(t)$.

Examination of Figure 4.1 shows that if we place the center of the cylinder at the origin of our coordinate system, the resulting deformation caused by $p(t)$ and $q(t)$ will be symmetrical about both the z and r axis of the cylinder. The particle displacement that occurs along each component of the cylinder can be expressed in terms of two potentials: Φ_o and Θ_o, which satisfy the following wave equations,

$$\Phi_o'' - v_p^2 \nabla^2 \Phi_o = 0, \tag{4.1}$$

$$\Theta_o'' - v_s^2 \nabla^2 \Theta_o = 0, \tag{4.2}$$

where v_p and v_s are the P- and S-wave speeds respectively. The particle displacements u and w when expressed in terms of the Φ_o and Θ_o potentials are

$$u = \frac{\partial \Phi_o}{\partial r} - \frac{\partial^2 \Theta_o}{\partial r \partial z}, \tag{4.3}$$

$$w = \frac{\partial \Phi_o}{\partial z} - \frac{1}{r}\frac{\partial}{\partial r}\left(r \frac{\partial \Theta_o}{\partial r}\right). \tag{4.4}$$

The boundary conditions for the stress in this case are similar to that of the SHCM, in that the particle displacement on the interior and the exterior of the cavity have to be equal (Heelan, 1952). The two boundary conditions that work for this problem, when expressed in terms of the auxiliary wave functions are

$$p(t) = -\lambda \nabla^2 \Phi_o + 2\mu \frac{\partial}{\partial r}\left(\frac{\partial \Phi_o}{\partial r} - \frac{\partial^2 \Theta_o}{\partial r \partial z}\right), \tag{4.5}$$

and

$$q(t) = -\mu \frac{\partial}{\partial r}\left(2\frac{\partial \Phi_o}{\partial z} + \nabla^2 \Theta_o - 2\frac{\partial^2 \Theta_o}{\partial z^2}\right). \tag{4.6}$$

After obtaining these boundary conditions for the stress on the medium, the auxiliary wave functions shown in Equations 4.1 and 4.2 are expressed as Hankel functions, such that

$$\Phi_o = \int_0^\infty e^{ikVt} dk \int_C f_o(\sigma, k)\ H_o^{(1)}\ (\sigma r)\ e^{z(\sigma^2 - k^2)^{\frac{1}{2}}}\ d\sigma, \tag{4.7}$$

$$\Theta_o = \int_0^\infty e^{ikVt} dk \int_C g_o(\sigma, k)\ H_o^{(1)}\ (\sigma r)\ e^{z(\sigma^2 - h^2)^{\frac{1}{2}}}\ d\sigma. \tag{4.8}$$

$H_o^{(1)}$ is a Hankel function of the first kind and zeroth order, and C is a loop that goes from $i\infty$ around $-h$ and $-k$ and excludes the origin. The terms $f_o(\sigma, k)$ and $g_o(\sigma, k)$ correspond to the boundary conditions at the source, and can be solved using a Fourier integral that satisfies Equations 4.7 and 4.8. Once expressions for these terms has been determined they can be used in conjunction with Equations 4.1 and 4.2, and Equations 4.3 and 4.4, to obtain expressions for the particle displacements u and w. These expressions comprise two separate wave systems, a P-wave (u_p,0,w_p) that propagates with velocity v_p, and an S-wave (u_{SV},0,w_{SV}) that propagates with velocity v_s. In other words, u_p and w_p are the particle displacements along the u and w directions (shown in Figure 4.1) for the P-waves, and u_{SV} and w_{SV} are the particle displacements along the u and w directions for the S-waves. Note that since we have only considered the motion along the axial and radial components of the cylinder, we can only account for vertically polarized S-waves using the Heelan model in this study. Taking these two separate wave systems into consideration, we can see that particle displacement along each cylindrical component will be a superpostion of both the P- and S-wave particle displacements, such that

$$u = u_p + u_{sv}, \tag{4.9}$$

$$w = w_p + w_{sv}. \tag{4.10}$$

The expressions obtained for the particle displacement in the HCM are

$$u_p = \frac{1}{R}\left[F_1(\phi)\frac{d}{dt}p(t) + G_1(\phi)q(t)\right] sin\phi, \tag{4.11}$$

$$w_p = \frac{1}{R}\left[F_1(\phi)\frac{d}{dt}p(t) + G_1(\phi)q(t)\right] cos\phi, \tag{4.12}$$

$$u_{sv} = \frac{1}{R}\left[F_2(\phi)\frac{d}{dt}p(t) + G_2(\phi)q(t)\right] cos\phi, \tag{4.13}$$

$$w_{sv} = \frac{1}{R}\left[F_2(\phi)\frac{d}{dt}p(t) + G_2(\phi)q(t)\right] sin\phi, \tag{4.14}$$

where R is the distance from the center of the source to the point of observation, and ϕ is the angle between the axial component of the cylinder and the line connecting the center of the cylinder to the point of observation, as shown in Figure 4.1. The terms F_1, F_2, G_1, and G_2 are given by

$$F_1(\phi) = \Delta(1 - 2v_s^2 cos^2\phi/V_p^2)/4\pi\mu v_p, \tag{4.15}$$

$$F_2(\phi) = \Delta sin2\phi/4\pi\mu v_s, \tag{4.16}$$

$$G_1(\phi) = -Av_s^2 cos\phi/4\pi\mu v_p^2, \tag{4.17}$$

$$G_2(\phi) = Asin\phi/4\pi\mu. \tag{4.18}$$

In this set of equations, μ is the rigidity of the medium in Newtons per meter, v_p is the P-wave speed in meters per second, and v_s is the S-wave speed in meters per second. The terms Δ and A in these equations are the volume and area of the cylindrical cavity respectively, which are given by

$$\Delta = 2\pi a^2 L, \tag{4.19}$$

$$A = 4\pi a L, \tag{4.20}$$

where a and L are the radius and length of the cylinder, as shown in Figure 4.1.

One of the major differences between this model and the SHCM is the fact that the particle displacement depends on the angle ϕ, which is shown in Figure 4.1. This suggests that the orientation of the cavity with respect to the point of observation plays a significant role on the measured particle displacement, if in fact the HCM is able to make accurate predictions about dynamite data obtained in the field. There are numerous scientific studies that have been conducted which show a clear variation in S-wave amplitude with offset, suggesting that the orientation of a source plays a significant role in S-wave amplitudes (Blair, 2007). The HCM allows us to predict the nature of S-waves, which could prove to be very advantageous in modeling dynamite explosions.

4.2 Pressure Pulse and Particle Displacement

The pressure pulse that is assigned to $p(t)$ and $q(t)$ in Equations 4.11 through 4.14 plays a significant role in the particle displacement of the HCM. The choice of pressure pulse is completely arbitrary, and the two sources are assumed to act independently of one another (Heelan, 1952). For the purposes of this study, we will assume that $p(t)$ and $q(t)$ are equal in Equations 4.11 through 4.14. Pressure pulses $p_1(t)$, $p_2(t)$, and $p_3(t)$, given in Equations 2.18 through 2.20 were used for the source activation waveform in $p(t)$ and $q(t)$ in Equations 4.11 through 4.14, and the corresponding particle displacements were computed; the results of this computation can be seen in Figures 4.2 through 4.6. In each of these figures the volume of the cylinder, the distance from the source to the point of observation, the speed of the P- and S-waves, and the frequency of the source remained constant. The values of these parameters were as follows:

$$R = 100\ m, \tag{4.21}$$

$$a = 10\ m, \tag{4.22}$$

$$L = 100\ m; \tag{4.23}$$

$$Vp = 2000\ m/s, \tag{4.24}$$

$$Vs = 1000\ m/s, \tag{4.25}$$

$$f_o = 30\ Hz. \tag{4.26}$$

Also note that the angular frequency used in the pressure pulses of Equations 2.18 through 2.20 was calculated as:

$$\omega = 2\pi f_o. \tag{4.27}$$

Note that unless otherwise specified, these parameters were used to create all of the theoretical plots in the HCM. Observation of Figures 4.2 through 4.6 shows a distinct variation in particle displacement $u(t)$ and $w(t)$ based on the pressure pulse that is assigned to the source. Similar to the SHCM, it is important to assign a pulse to the source that represents a realistic scenario for an explosion, so that the HCM can make accurate predictions regarding the the particle displacement and frequency spectra of data obtained in the field.

4.3 Amplitude Variation with Angle Phi

The variables found in Equations 4.15 through 4.18 scale the amplitude of the particle displacement when they are used in Equations 4.11 through 4.14. These variables are dependent on the angle ϕ, which suggests that the orientation of the source affects the overall amplitude of the particle displacements that are computed with the HCM. Figures 4.7 and 4.8 shows the amplitude variation of these variables with a changing ϕ value between 0 and 2π.

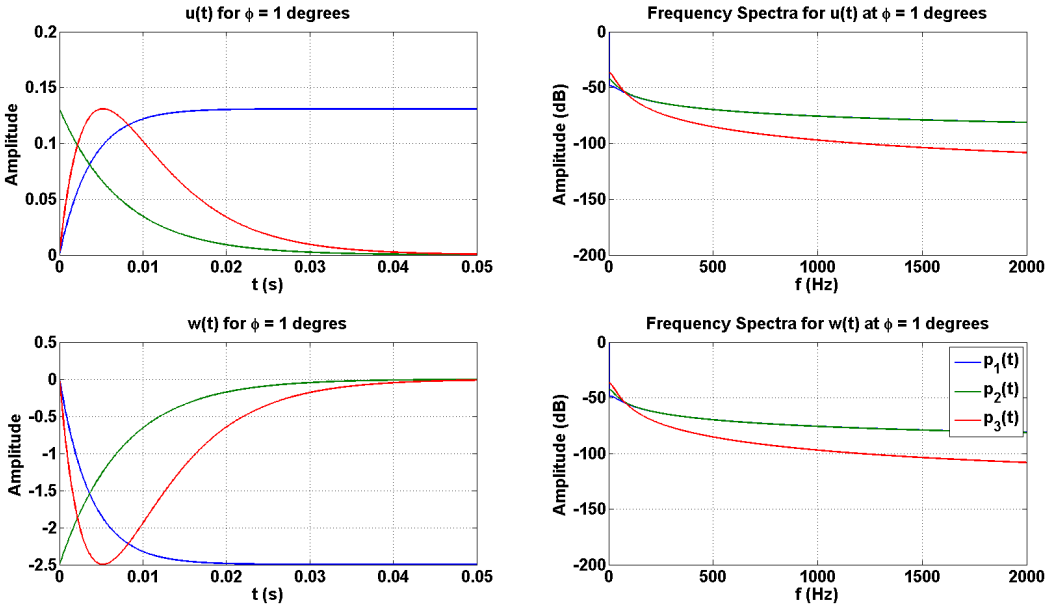

Figure 4.2: Varying pressure pulse inputs for both $p(t)$ and $q(t)$ and their resulting particle displacement in the Heelan Cylindrical Model for with $\phi = 1^o$. Note that the same pressure pulse was used for both $p(t)$ and $q(t)$ to compute the particle displacements $u(t)$ and $w(t)$.

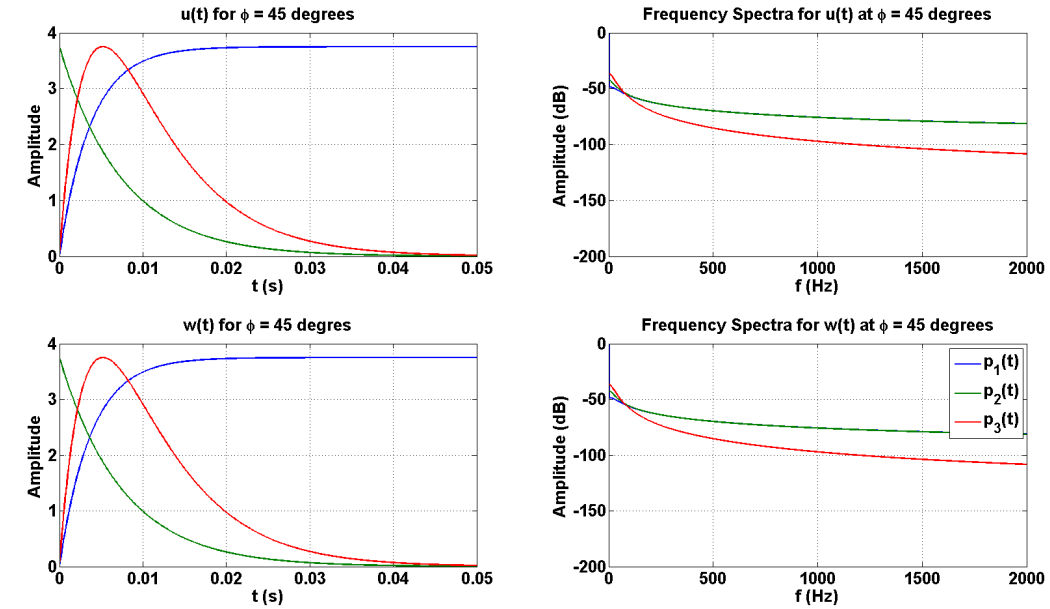

Figure 4.3: Varying pressure pulse inputs for both $p(t)$ and $q(t)$ and their resulting particle displacement in the Heelan Cylindrical Model for with $\phi = 45^o$. Note that the same pressure pulse was used for both $p(t)$ and $q(t)$ to compute the particle displacements $u(t)$ and $w(t)$.

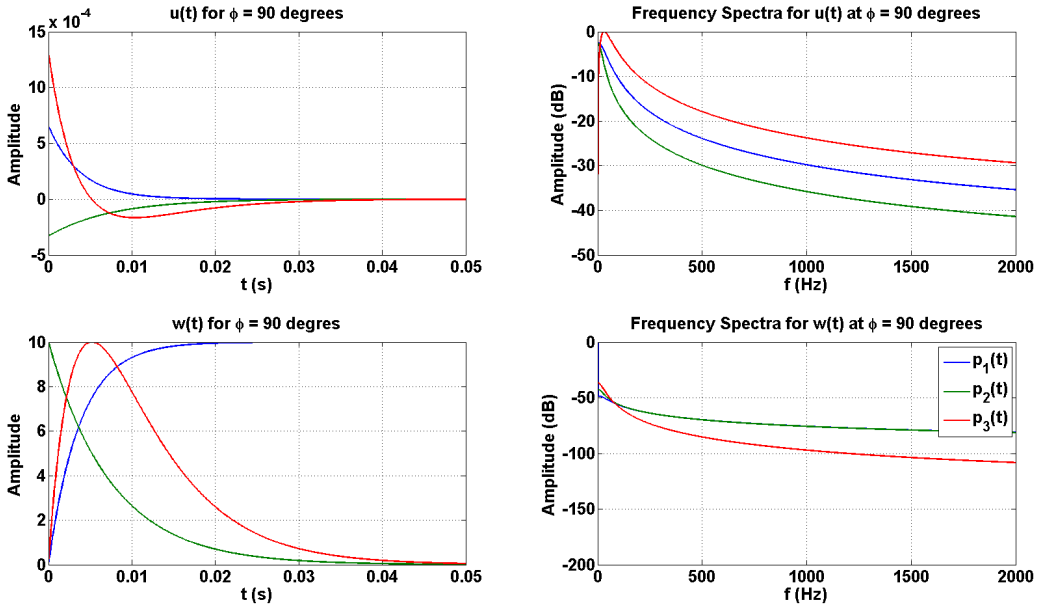

Figure 4.4: Varying pressure pulse inputs for both $p(t)$ and $q(t)$ and their resulting particle displacement in the Heelan Cylindrical Model for with $\phi = 90^o$. Note that the same pressure pulse was used for both $p(t)$ and $q(t)$ to compute the particle displacements $u(t)$ and $w(t)$.

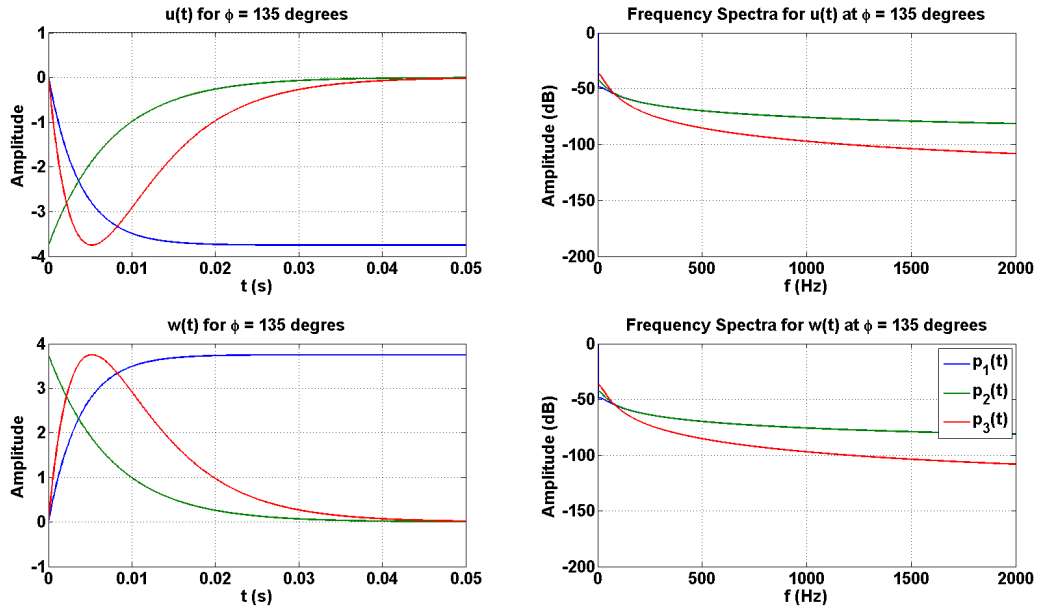

Figure 4.5: Varying pressure pulse inputs for both $p(t)$ and $q(t)$ and their resulting particle displacement in the Heelan Cylindrical Model for with $\phi = 135^o$. Note that the same pressure pulse was used for both $p(t)$ and $q(t)$ to compute the particle displacements $u(t)$ and $w(t)$.

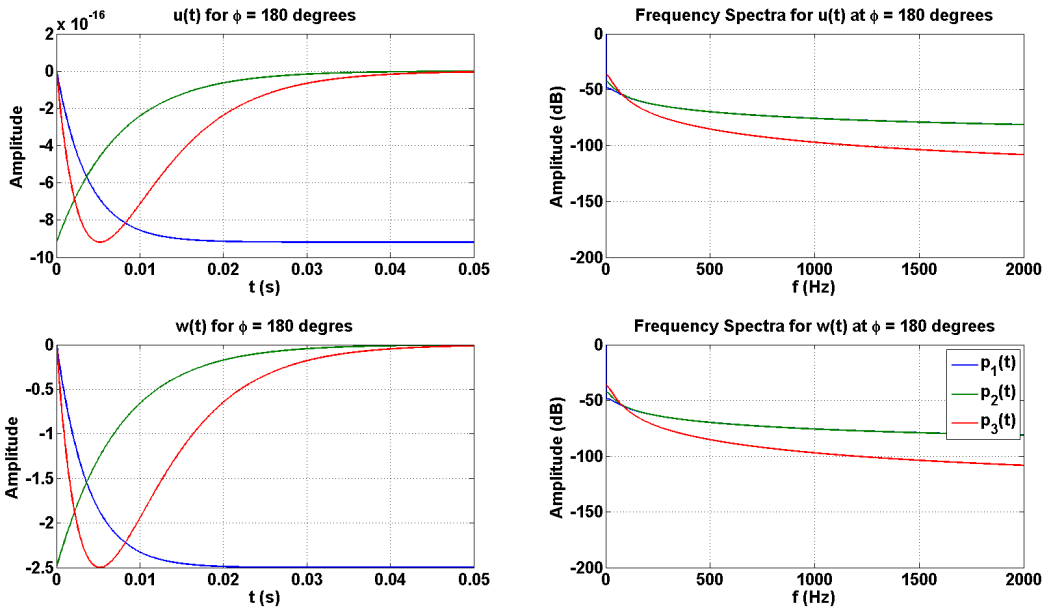

Figure 4.6: Varying pressure pulse inputs for both $p(t)$ and $q(t)$ and their resulting particle displacement in the Heelan Cylindrical Model for with $\phi = 180^o$. Note that the same pressure pulse was used for both $p(t)$ and $q(t)$ to compute the particle displacements $u(t)$ and $w(t)$.

Figure 4.7 shows the amplitude variation of the P- and S-waves when the source is subject to a source activation waveform $p(t)$ only in Equations 4.11 through 4.14. Note that this is a polar plot that shows amplitude variation with angle ϕ, and thus the radius of the polar plot corresponds to the amplitude at a specific angle ϕ. The amplitude of the P-wave pattern (shown in blue) corresponds to the $F1$ variable found in Equation 4.15, and the amplitude of the S-wave pattern (shown in red) corresponds to the $F2$ variable found in Equation 4.16 (Heelan, 1952). This plot predicts that, assuming there is only a force acting along the radial component of the hollow cylinder, that the P-waves should have a nonzero amplitude for all values of ϕ. However, this model also predicts that for ϕ values of 0^o, 90^o, 180^o, and 270^o that there should be no S-wave radiation observed, and for ϕ values of 45^o, 135^o, 225^o, and 315^o that there should be a maximum in the observed S-wave radiation, and it should be larger than that of the P-waves. This is something that may be possible to observe in dynamite data obtained in the field, and it could prove to be very useful when designing

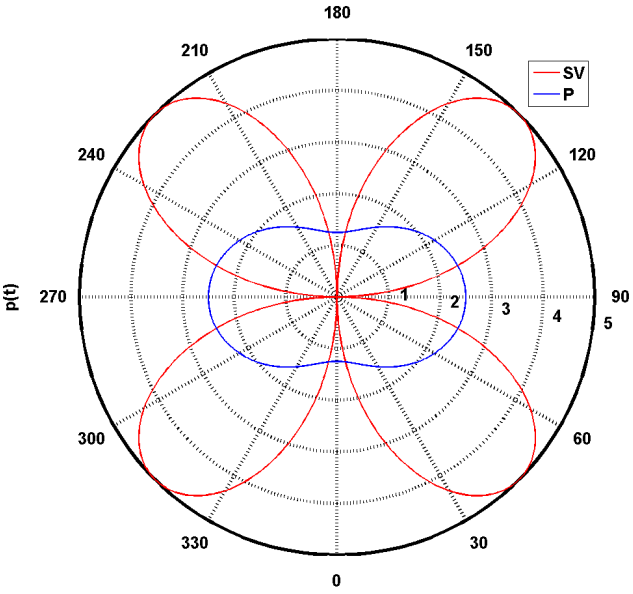

Figure 4.7: Variation of P and SV amplitudes with ϕ, as a result the source activation waveform $p(t)$ only. Note that this plot has been normalized to the highest amplitude. For the P-waves, which are shown in blue, the radius is proportional to the F1 variable; in the case of the SV-waves, shown in red, the radius is proportional to F2.

surveys with dynamite for the purposes of measuring S-waves, as the borehole orientation may have significant effects on the amplitude of the radiated S-waves.

Figure 4.8 shows the amplitude variation for the P- and S-waves when the source is subject to a source activation waveform $q(t)$ only in Equations 4.11 through 4.14. In this case the radius of the P-wave pattern corresponds to the $G1$ in Equation 4.17, and the radius of the S-wave pattern corresponds to the $G2$ variable found in Equation 4.18 (Heelan, 1952). When the source is subject to a source activation waveform $q(t)$ only, there are values of ϕ where both the P- and S-waves have zero amplitude, however this should not occur simultaneously. Realistically, a source detonated in the field will probably have a amplitude pattern that is a combination of Figures 4.7 and 4.8, as there will be energy traveling up and down the borehole when the shot is detonated (Blair, 2007).

Figure 4.9 and 4.10 shows the distribution in power of $u(t)$ and $w(t)$ for varying angles of ϕ, and a cavity radius of $a = 10\ m$. The power distribution appears to be periodic after 180^o,

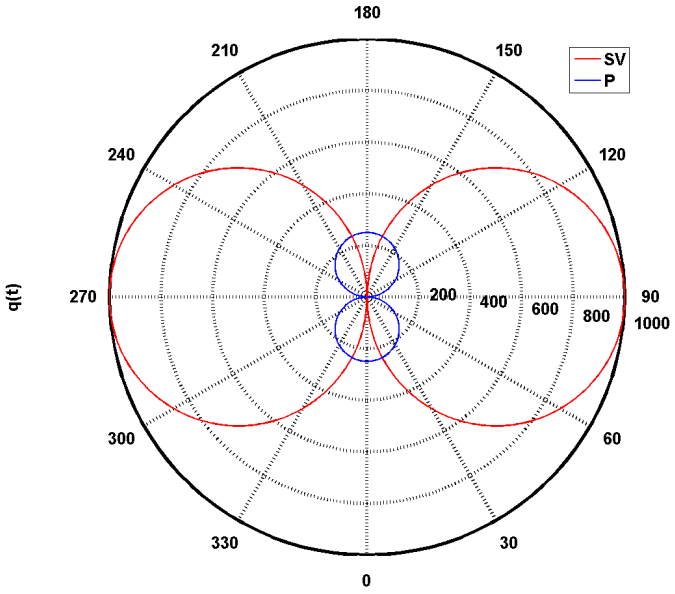

Figure 4.8: Variation of P and SV amplitudes with ϕ, as a result of the source activation waveform $q(t)$ only. Note that this plot has been normalized to the highest amplitude. For the P-waves, which are shown in blue, the radius is proportional to the G1 variable; in the case of the SV-waves, shown in red, the radius is proportional G2.

so we can confine our discussion to angles between 0^o and 180^o. The maximum power occurs at $\phi = 90^o$, and the minimum power occurs at $\phi = 0^o$ and $\phi = 180^o$. This observation is consistent with the behavior of the particle displacements in Figures 4.2 through 4.6. These figures display a significant variation in the particle displacements $u(t)$ and $p(t)$ when the value of ϕ changes. Additionally, the w displacement dominants most of the theoretical power, which is consistent with our observations in Figure 4.7 and 4.8.

There are three key observations to take note of regarding these amplitude changes that distinguishes the HCM from the SHCM: (1) The amplitudes of the particle displacements are dependent on the value of ϕ. (2) The polarity of the particle displacements depends on angle ϕ. (3) The maximum power occurs at $\phi = 90^o$, and the minimum power occurs at $\phi = 0^o$ and $\phi = 180^o$. This is significantly different than the SHCM. Equation 2.16 and Figure 2.1 shows that the particle displacement is dependent only on the radial component of the cavity in the SHCM (Sharpe, 1942), and thus the orientation of the cavity should not

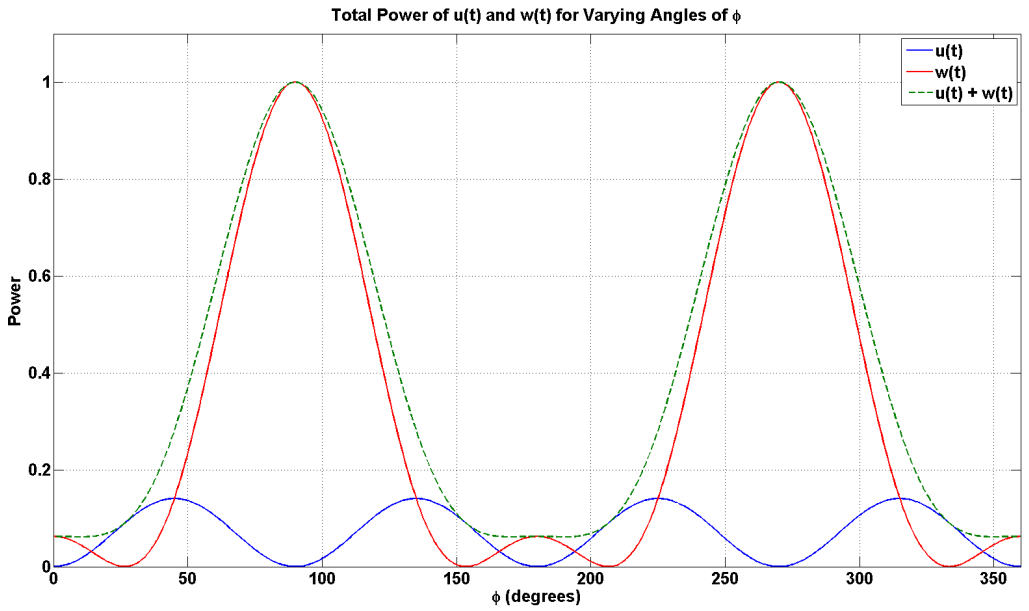

Figure 4.9: Plot of the power distribution of $u(t)$ and $w(t)$ for varying angles of ϕ between 0^o and 180^o. After 180^o the power distribution becomes periodic, suggesting that power in the HCM is symmetric about the axial component of the cavity.

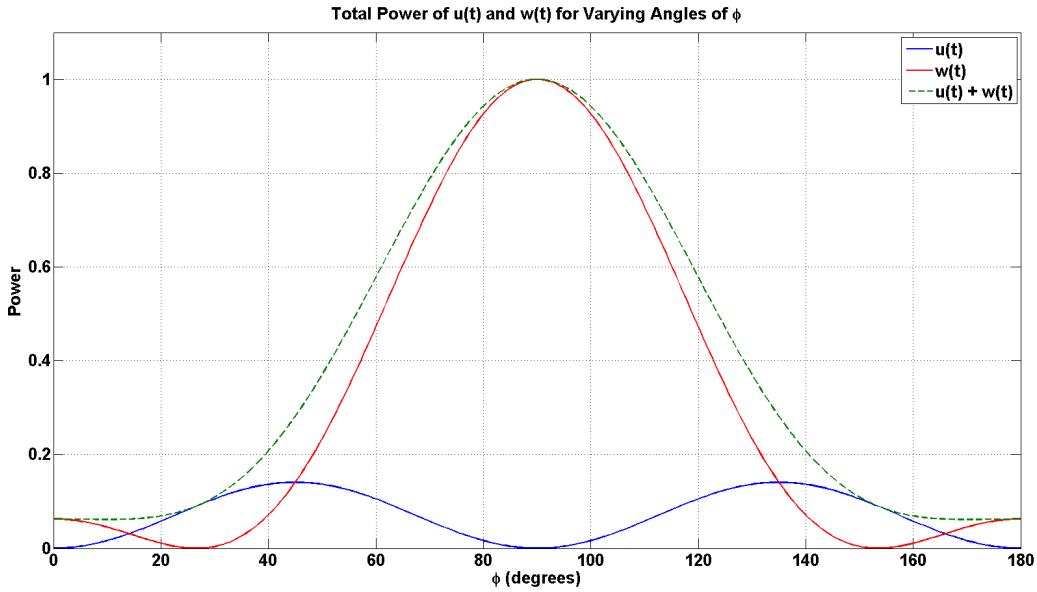

Figure 4.10: Plot of the shot power distribution of $u(t)$ and $w(t)$ for varying angles of ϕ between 0^o and 180^o. The maximum power occurs at 90^o, and the power spectra appears to be dominated by the $w(t)$ particle displacement.

contribute to the particle displacement and frequency spectra. Due to the variation in the particle displacement with ϕ, the orientation of the cavity plays an important role in the particle displacement that is calculated in the HCM.

4.4 The Role of the Cavity Size

To change the cavity size in the HCM, we have the options of varying the radius or length of the cavity. Figure 4.11 shows the power variation of $u(t)$, $w(t)$, and $u(t) + w(t)$ with angle ϕ for different values of a, the cavity radius. Note that in order to obtain this figure, we used the applicable parameters in Equations 4.21 through 4.26; we kept the value of L constant at 10 m for these calculations. Observation of this figure shows that when the cavity radius is varied, the location of the peak amplitudes remain unchanged form that of Figure 4.10 (which depicts the total power for the HCM as a function of ϕ) for $u(t) + w(t)$, however the amplitudes have been scaled significantly with increased cavity radius. This suggests that in the HCM, changing the radius of the cavity does not affect the location of the peaks in the power spectra(and thus the radiation pattern), however it does scale the amplitudes. Alternatively, Figure 4.12 shows a similar calculation, however this time it is the power variation in the HCM with angle ϕ for different values of L, the cavity length. Also note that we used the same parameters for these calculations as we did when we varied the cavity radius a. The results of these calculations are similar to that of the previous one, in that peak locations remain unchanged, and the amplitude increases with larger cavity lengths. From this we can conclude that varying both a and L increases the volume of the cavity, which increases the overall power predicted by the HCM. This suggests that volume of the cavity plays the most significant role in power of the HCM, which is also true for the SHCM.

Comparison of Figures 4.11 and 4.12 reveals a significant difference in the amplitudes of $u(t)$, $w(t)$, and $u(t) + w(t)$ when altering the cavity radius a as opposed to the cavity length

L. Varying the cavity radius seems to have the most significant effect on the amplitudes, which may lead to the conclusion that it is the most optimal way of increasing power in this model. Recall that the volume of the cavity is given by Equation 4.19, and the area of the cavity is given by Equation 4.20. From these equations we can see that the cavity radius is going to affect the volume in a more significant manner as it is a squared term in this equation while the length is a single power; in the area equation both terms are only raised to a single power so they have the same effect on the area. Therefore, it is expected that the cavity radius should have the most significant effect on the overall power predicted by the HCM. However, there are some issues with expanding the cavity radius in practice. Generally, boring instruments that are used to drill holes for dynamite are of a fixed width, and it is often more practical to adjust the depth at which a charge is placed than the width of the borehole, simply by drilling deeper into the subsurface. Therefore, the more likely scenario to encounter in the field is the variation in L, not a.

Figures 4.13 through 4.22 shows a series of particle displacements at different ϕ values and their corresponding frequency spectra, that were also computed using varying values for the cavity radius a, a fixed cylinder length given in Equation 4.23, and pressure pulse $p_3(t)$ given in Equation 2.20. These figures reveal a significant difference between the HCM and the SHCM in the behavior of the frequency spectra with varying cavity size. In the SHCM we observed an increase in the particle displacements for larger charge sizes, but there was also a significant decrease in the dominant frequency of the spectra as the charge size was increased. When dealing with the HCM in Figure 4.17, there is an increase in particle displacement with larger charge sizes, but there is no decrease in dominant frequency when the cavity volume is enlarged. This suggests that a decrease in dominant frequency with increased cavity size may not be a feature of this particular model.

A major difference between the SHCM and HCM is role of the cavity orientation in the particle displacement. Both models predict an increase in particle displacement with

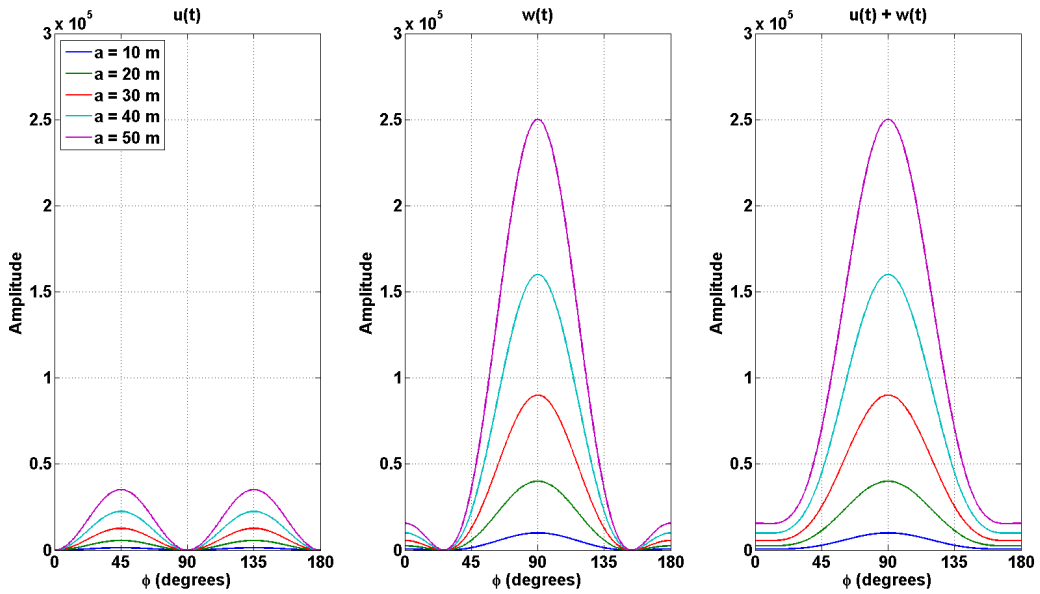

Figure 4.11: Variation in power distribution of $u(t)$, $w(t)$, and $u(t) + w(t)$ for varying values of ϕ and cavity radius a. The minimum and maximum power remain unchanged from Figure 4.10, however, the increase in cavity radius has scaled the amplitudes; larger values of cavity radii produce higher amplitudes in the HCM. Also note that $w(t)$ appears to be larger than than $u(t)$ for all values of a.

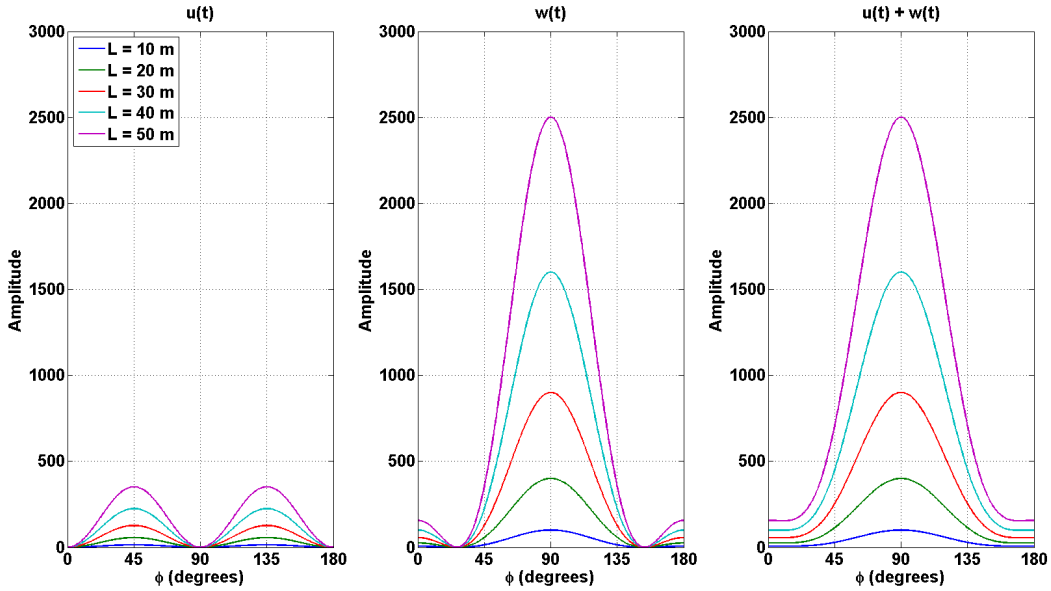

Figure 4.12: Variation in power distribution of $u(t)$, $w(t)$, and $u(t) + w(t)$ for varying values of ϕ and cavity length L. The minimum and maximum power remain unchanged from Figure 4.10, however, the increase in cavity length has scaled the amplitudes; larger values of cavity length produce higher amplitudes in the HCM. Also note that $w(t)$ appears to be larger than $u(t)$ for all values of L. This plot is very similar to that of Figure 4.11 where the value of a was varied instead of the length, note however that the overall amplitudes of all displacements are higher in when a is varied.

larger cavities, and thus larger charge sizes. However, particle displacement in the SHCM is independent of the cavity orientation due to the symmetry of the problem. In the HCM, the particle displacement depends on the orientation of the cavity, and needs to be taken into account when making theoretical predictions about dynamite data obtained in practice.

4.5 Application of the HCM to data obtained in the field

There are several key observations from the theory of the HCM that, if observed in real data, can confirm the validity of the HCM in applications to data collected in the field. These observations include:

1. Variation in shot power and amplitude with ϕ
2. Maximum shot power occurring at $\phi = 90^o$
3. Minimum shot power at $\phi = 0^o$ and $\phi = 180^o$
4. Increase in shot power for larger charge sizes
5. Variation in the frequency spectra with ϕ

If we can observe these effects in the field, we would have experimental verification of the HCM, and could potentially use it to improve the quality of dynamite surveys.

There are several potential limitations of this model which could cause difficulties when trying to model dynamite data that has been collected in practice. The amplitude variation plots shown in Figure 4.7, 4.8, and 4.10, assume that the borehole is pointed straight downwards, in other words the $\phi = 0^o$ angle is aligned directly along the $-z$ axis. The $\phi = 0^o$ angle can be rotated to produce the correct plots, however, if we assume that the borehole is oriented vertically when it is not, we may see significant deviations from the predictions of the HCM. Additionally, the HCM is still in effect a far-field approximation, and if the

source is located too close to the point of measurement, we may not be able to effectively use this model to make accurate predictions of the obtained data.

4.6 Chapter Summary

- The HCM predicts a variation in amplitude with borehole orientation.
- Altering the cavity radius a has the most significant impact on the amplitudes in the HCM, however, it is not practical to increase the radius of the cavity in practice as boring instruments are of fixed with.
- The HCM does not show any sort of reliable variation in the frequency spectra for changing borehole orientation.
- The HCM predicts that the maximum amplitude should occur at $\phi = 90^o$, along the radial component of the borehole.
- The HCM predicts an increase in amplitude response with larger cavity size, and thus larger charge sizes.
- The HCM does not predict a change in dominant frequency with varying cavity size.

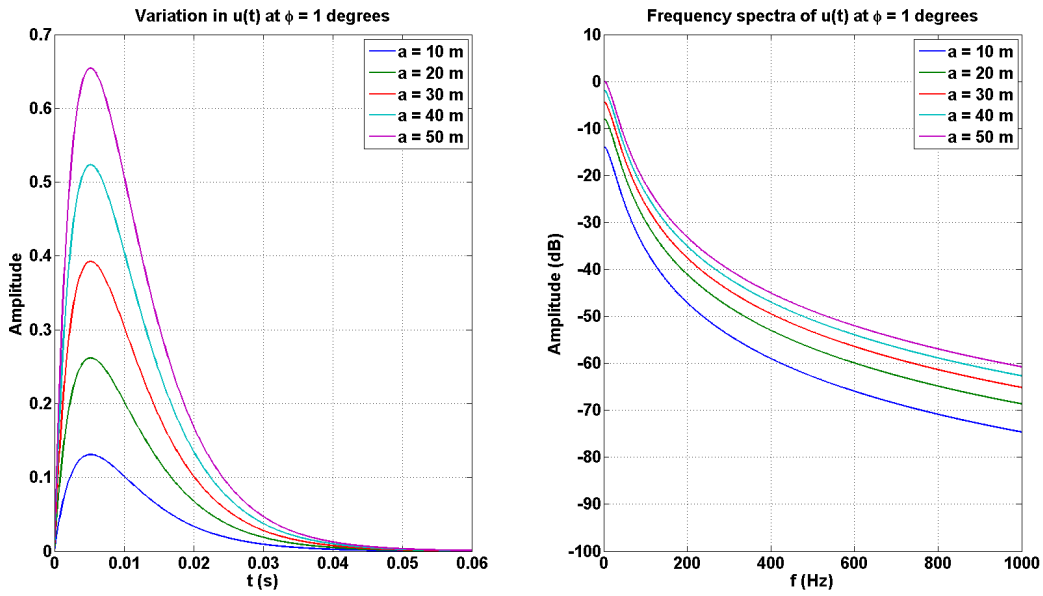

Figure 4.13: Variation in particle displacement $u(t)$ with cylinder radius for $\phi = 1^o$.

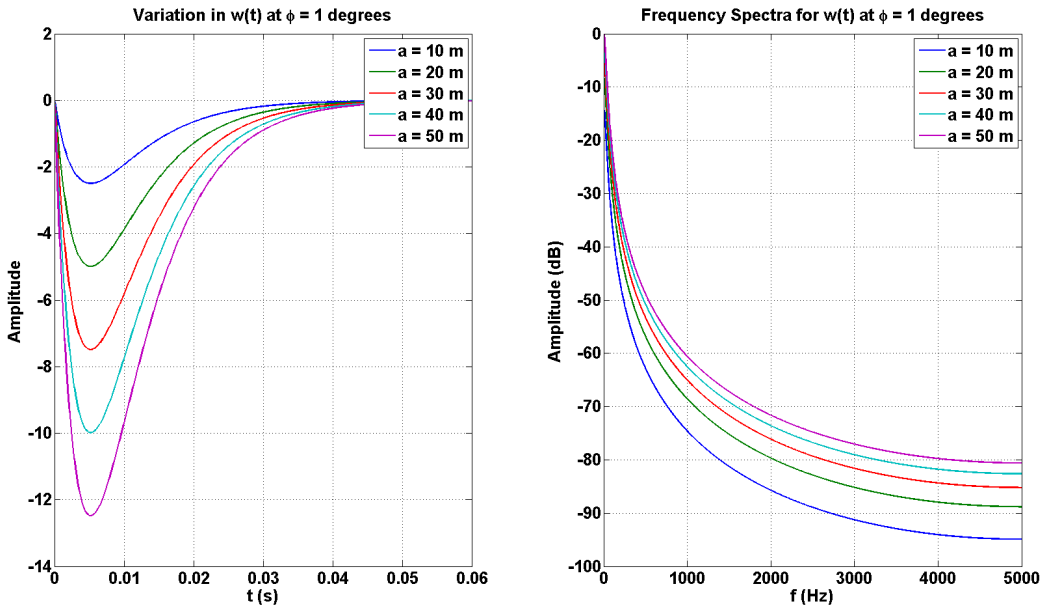

Figure 4.14: Variation in particle displacement $w(t)$ with cylinder radius for $\phi = 1^o$.

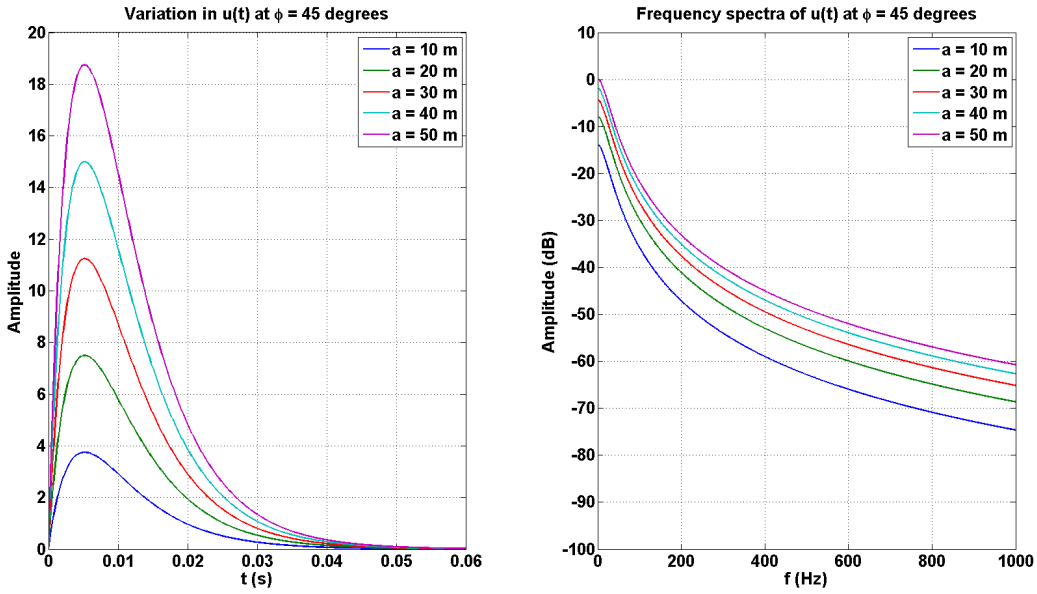

Figure 4.15: Variation in particle displacement $u(t)$ with cylinder radius for $\phi = 45^o$.

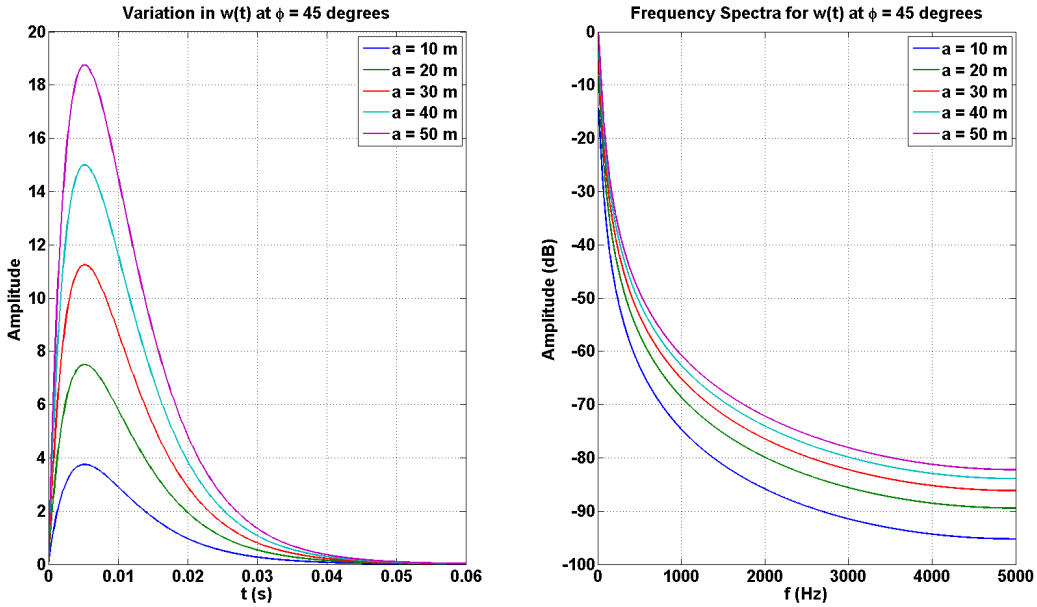

Figure 4.16: Variation in particle displacement $w(t)$ with cylinder radius for $\phi = 45^o$.

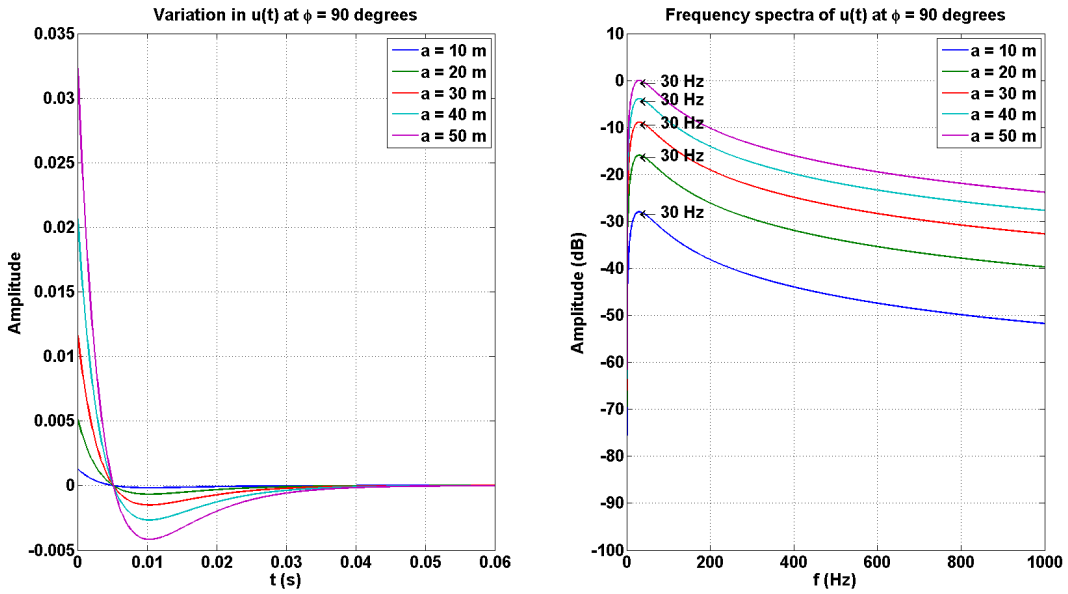

Figure 4.17: Variation in particle displacement $u(t)$ with cylinder radius for $\phi = 90^o$.

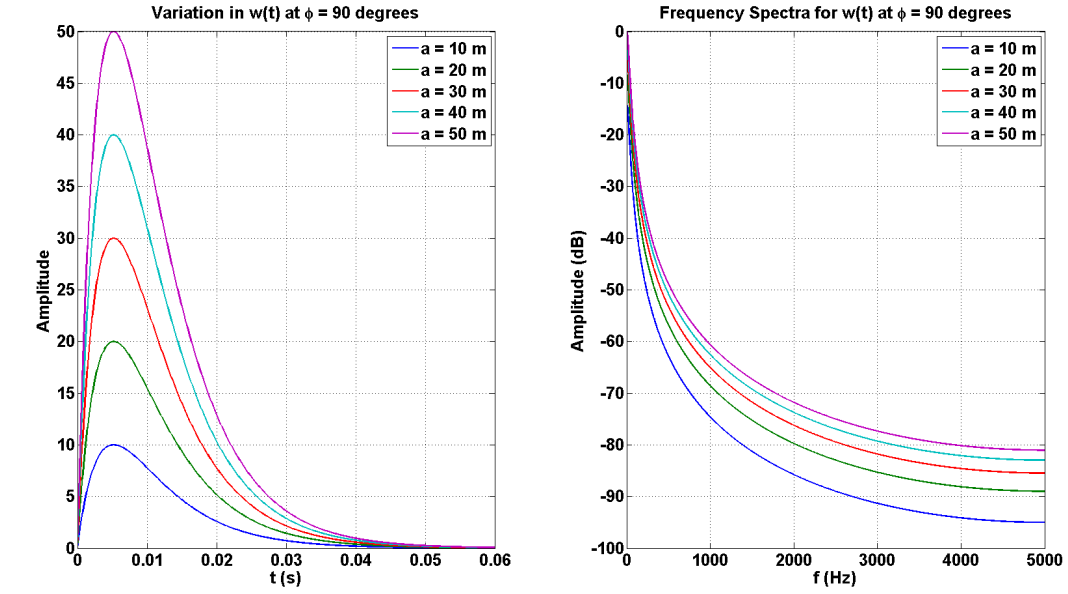

Figure 4.18: Variation in particle displacement $w(t)$ with cylinder radius for $\phi = 90^o$.

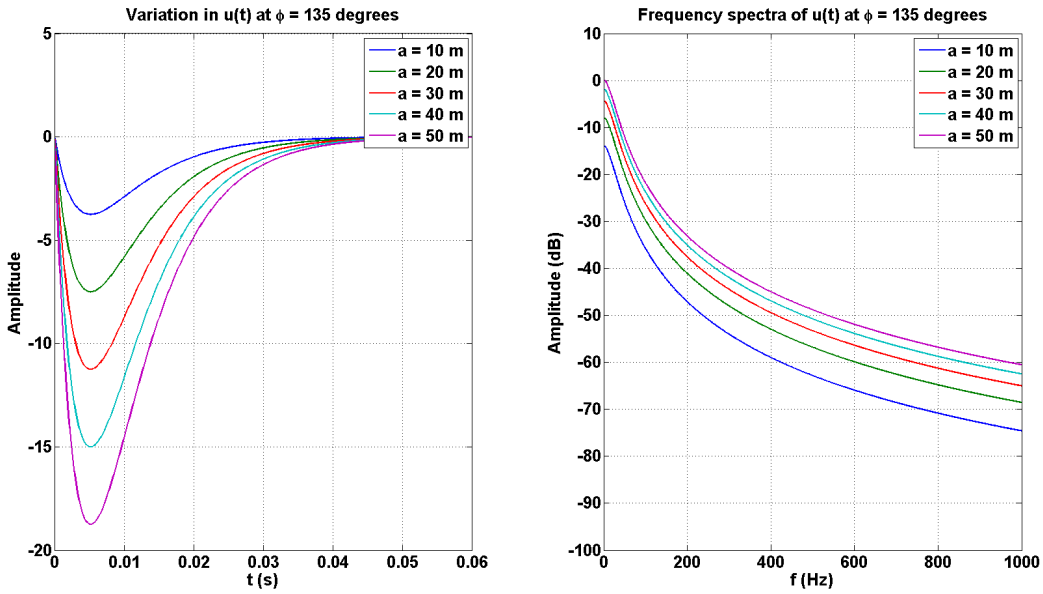

Figure 4.19: Variation in particle displacement $u(t)$ with cylinder radius for $\phi = 135^o$.

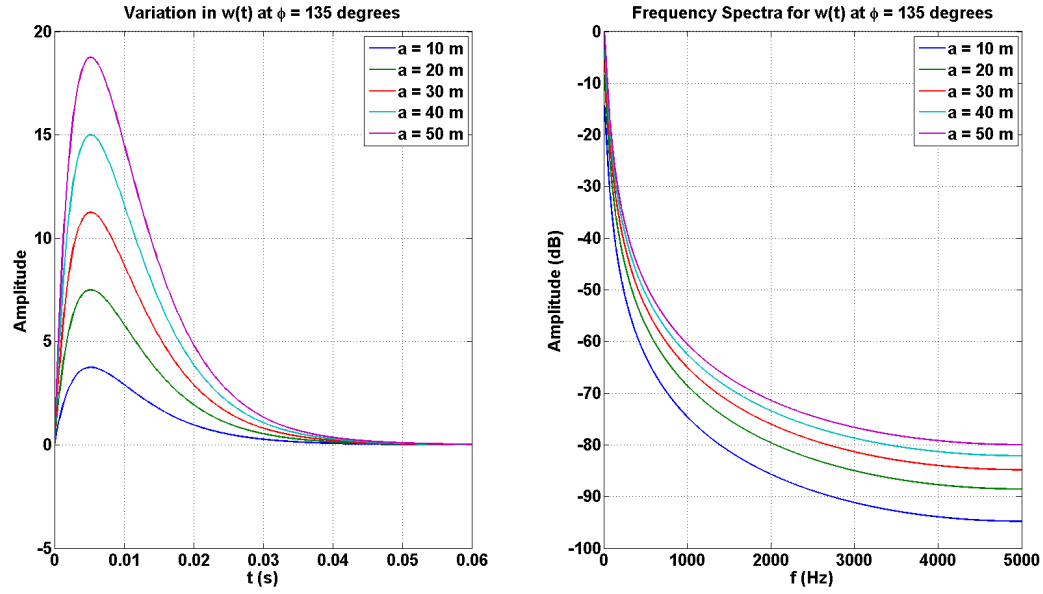

Figure 4.20: Variation in particle displacement $w(t)$ with cylinder radius for $\phi = 135^o$.

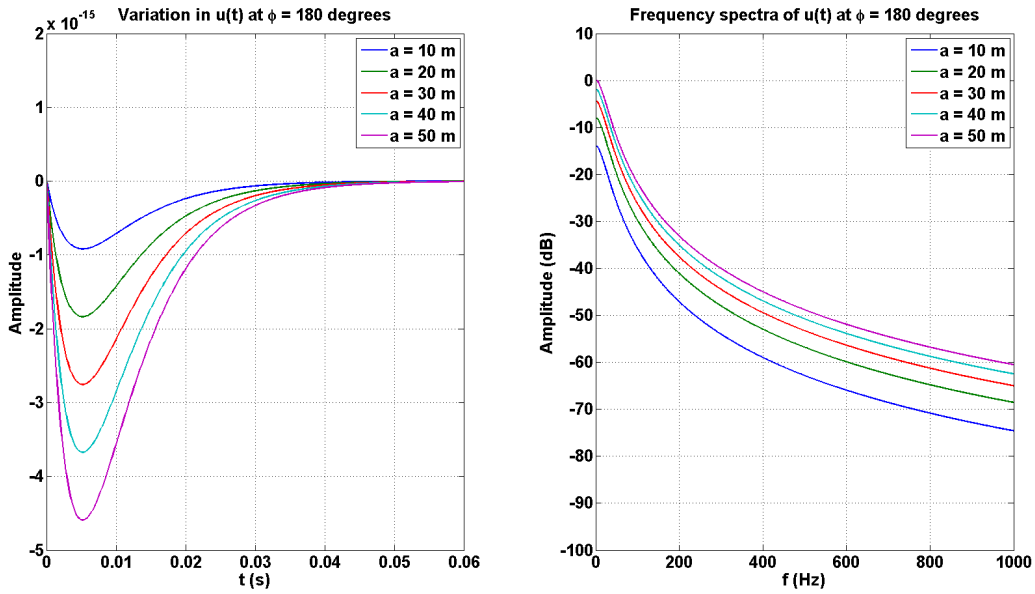

Figure 4.21: Variation in particle displacement $u(t)$ with cylinder radius for $\phi = 180^o$.

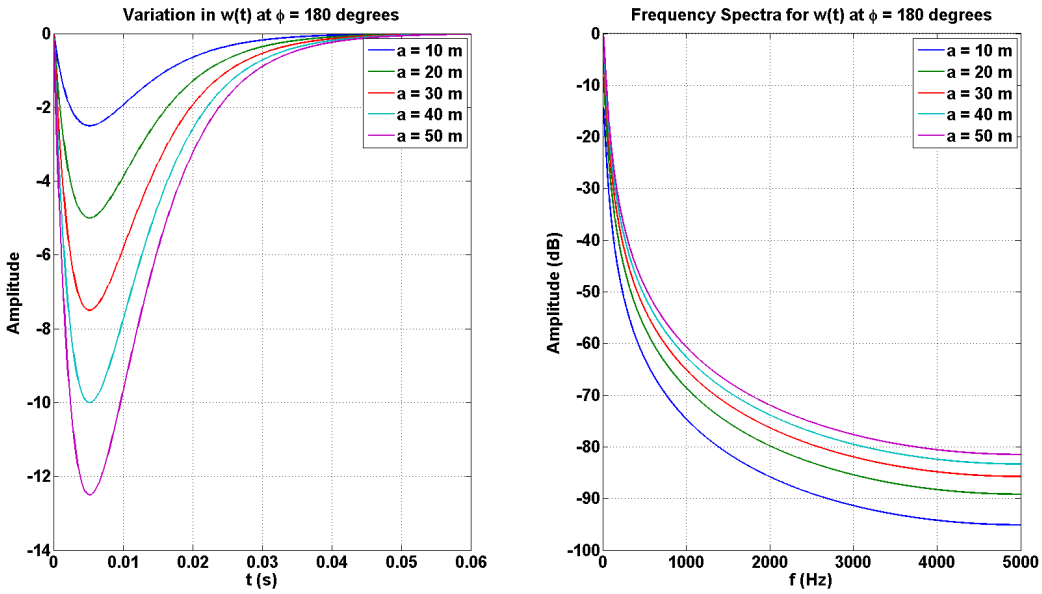

Figure 4.22: Variation in particle displacement $w(t)$ with cylinder radius for $\phi = 180^o$.

Chapter 5

An Overview of the Data Used in This Study

The data used in this study was collected over the course of three field experiments, at two different sites: Priddis and Hussar. All of the data used in this study was collected using dynamite, which ranged in size from one third of a kilogram, to four kilograms. These field experiments have been covered in great detail by publications listed in our references, so we will provide a brief overview of the field work here (Margrave et al., 2011)(Bertram et al., 2012)(Hall et al., 2013).

5.1 Hussar 2011 low-frequency experiment

During this field experiment, a series of test charges ranging in size between 1 and 4 kg were buried in groups at three separate locations, at a depth of approximately 15 m along a horizontal 4.5 km long line of three-component geophones. Margrave et al. shows a series of geophone lines, which were all recording the test shots (Margrave et al., 2011). In this study we only used the data from the vertical component of Line 2, which was a series of three-component 10 Hz geophones spaced at 10 m intervals. For reference, Table 5.1 lists all of the relevant parameters of this experiment.

5.2 Priddis 2012 pulse-probe experiment

In this experiment, a series of test charges ranging in size between 0.0625 kg and 2 kg were buried at a depth of approximately 15 m depth along several horizontal lines of geophones. In this study, we used the data from the vertical component of the SM7 three-component 10 Hz geophones, which were spaced at 10 m intervals. The parameters for this data can be found in Table 5.2.

Hussar 2011 Parameters	
Smallest charge size	1 kg
Largest charge size	4 kg
Charge depth	15 m
Sample rate	2 ms
Geophone spacing	10 m
Shot spacing	20 m

Table 5.1: A list of parameters for the dynamite data obtained in the Hussar 2011 low-frequency experiment.

Priddis 2012 Parameters	
Smallest charge size	0.125 kg
Largest charge size	2 kg
Charge depth	15 m
Sample rate	1 ms
Geophone spacing	10 m
Shot spacing	20 m

Table 5.2: A list of parameters for the dynamite data obtained in the Priddis 2012 Pulse-probe experiment.

Priddis 2013 Parameters	
Smallest charge size	1 kg
Largest charge size	4 kg
Charge depth	15 m
Sample rate	1 ms
Geophone spacing	10 m
Shot spacing	20 m

Table 5.3: A list of parameters for the dynamite data obtained in the Priddis 2013 Pulse-probe experiment.

5.3 Priddis 2013 field experiment

The data from this experiment is different than that of the Hussar 2011 and Priddis 2012 experiments, since these data were collected using a vertical line of geophones placed in an observation well. In addition to the different geophone orientation from the previous experiments, some of the boreholes for the dynamite shots were drilled at an angle of 30^o. The charges ranged in size between 1 kg and 4 kg, and the boreholes were drilled in a direction that either faced the well, or faced in the opposite direction of the well. The parameters for this experiment can be found in Table 5.3.

Chapter 6

Spectral Notching and Source Ghosts

6.1 Spectral Notching Theory

Ghosts are a common phenomenon in seismic data that can contribute significantly to the spectral content of measured waves. A ghost occurs when a wave emitted from the source reflects off of the surface and travels back into the earth, creating an event that is a combination of of the free surface and a reflector (Hamarbatan and Margrave, 1998). Figure 6.1 shows a graphical depiction of a common ghost, wherein a wave travels upwards from a buried source and reflects off of the surface. This is then followed by a downward propagation and a second reflection off of the base of the layer, and finally the wave travels upward again where it is detected at the receiver.

A ghost can be modeled mathematically using the arrival times of two separate events. Let t_r represent the arrival time of the reflection event, and t_g represent the arrival time of the ghost. Using these two arrival times, a trace composed of a reflection event and its spectral ghost can be represented as

$$g(t) = \delta(t - t_r) + \delta(t - t_g), \tag{6.1}$$

where $g(t)$ represents the trace. Investigation of the geometry in Figure 6.1 reveals a way to simplify the expression given in Equation 6.1. The ray path for the ghost (represented by blue arrows) is longer than that of the reflection event (represented by the purple arrows), and thus the ghost will arrive at the receiver at a later time than the reflection. If the arrival time of the reflection is assigned a value of zero, and the t_g term is treated as the difference in time between the arrival of the reflection and the ghost event, Δt_g, Equation 6.1 becomes

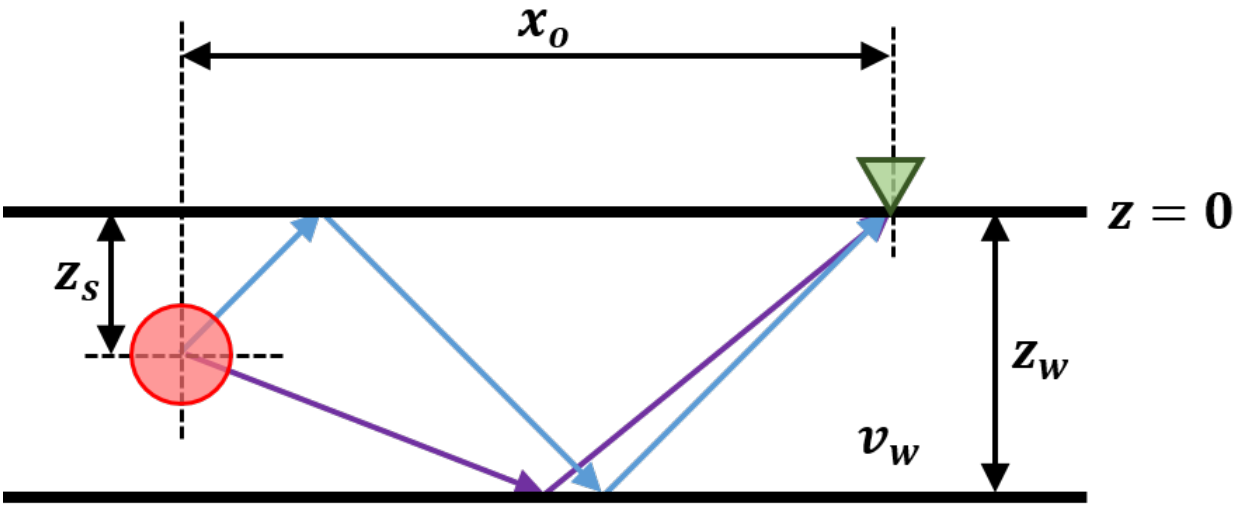

Figure 6.1: Graphical depiction of a source ghost, whose raypath is represented by the blue arrows. The source (shown in red) emits a wave that travels upwards and reflects off of the surface, which then travels downward and reflects a second time off of the base of the layer. This wave is then detected by the receiver (shown in green) as a source ghost. The raypath of the reflection event corresponding to this ghost is represented by the purple arrows in this figure. Note that the distance traveled by the ghost is longer than that of the reflection event.

$$g(t) = \delta(t) + \delta(t - \Delta t_g). \tag{6.2}$$

The Fourier Transform of Equation 6.2 can be used to theorize the effect of ghosts on the spectral content of the waves. The Fourier Transform of Equation 6.2 is given by

$$\hat{g}(\omega) = \int_{-\infty}^{+\infty} \delta(t) e^{-2\pi i \omega t} dt + \int_{-\infty}^{+\infty} \delta(t - \Delta t_g) e^{-2\pi i \omega t} dt, \tag{6.3}$$

where ω is the angular frequency. The Fourier transform of a delta function is given by

$$\int_{-\infty}^{-\infty} \delta(t - t_o) e^{-2\pi i \omega t} dt = e^{-2\pi i \omega t_o}, \tag{6.4}$$

and using this identity in Equation 6.3 yields the following expression:

$$\hat{g}(\omega) = 1 + e^{-2\pi i \omega \Delta t_g}. \tag{6.5}$$

which can be rewritten as

$$\hat{g}(\omega) = e^{-2\pi i \omega \Delta t_g/2} \left(e^{2\pi i \omega \Delta t_g/2} + e^{-2\pi i \omega \Delta t_g/2} \right). \tag{6.6}$$

This expression can be further simplified using the cosine identity

$$\cos(z) = \frac{e^{iz} + e^{-iz}}{2}, \tag{6.7}$$

which when used in Equation 6.6 results in the following expression:

$$\hat{g}(\omega) = 2e^{-2\pi i \omega \Delta t_g} \cos \pi \omega \Delta t_g. \tag{6.8}$$

Finally, the amplitude spectrum of $\hat{g}(\omega)$, which represents spectral content, is given by

$$|\hat{g}(\omega)| = |2 \cos \pi \omega \Delta t_g|. \tag{6.9}$$

The expression given in Equation 6.9 reveals critical information about seismic data containing a reflection and ghost event, since this equation will be zero whenever the terms inside of the cosine equal $\pi/2$. Additionally, given the periodic nature of the cosine function, there

will be multiple points in the frequency spectra where it goes to zero. This phenomenon is referred to as "notching" in the frequency spectra, and can occur whenever you have ghosts with reflection data (Hamarbatan and Margrave, 1998). Mathematically, the phenomenon discussed here can be derived by first expressing the conditions under which Equation 6.1 will be zero:

$$\pi\omega\Delta t_g = \frac{\pi}{2}. \tag{6.10}$$

Based on the condition expressed Equation 6.10, the frequency spectra given by Equation 6.9 will be zero when the angular frequency is

$$\omega = \frac{1}{2\Delta t_g}. \tag{6.11}$$

For this derivation we have assumed that the amplitude of the reflection and the ghost event are both positive, which can be seen in Equation 6.2. Depending on the reflectivity of the layers in the subsurface, the amplitude of the ghost event could also be negative. Under this condition, Equation 6.2 can be written as

$$g(t) = \delta(t) - \delta(t - \Delta t_g), \tag{6.12}$$

where we have used a negative sign in the second term of the right hand side of this equation to represent a negative polarity of the ghost with respect to the reflection event. If we carry out the same derivation using the identity for sine

$$\sin(z) = \frac{e^{iz} - e^{-iz}}{2i}, \tag{6.13}$$

we arrive at an amplitude spectrum of

$$|\hat{g}(\omega)| = |2\sin\pi\omega\Delta t_g|. \tag{6.14}$$

Equations 6.9, 6.14, and 6.11 reveals a common phenomenon that is present in most seismic signals (Hamarbatan and Margrave, 1998). Whenever a seismic signal contains a reflection and a ghost event, there will be points in the frequency spectra (given in Equation 6.9)

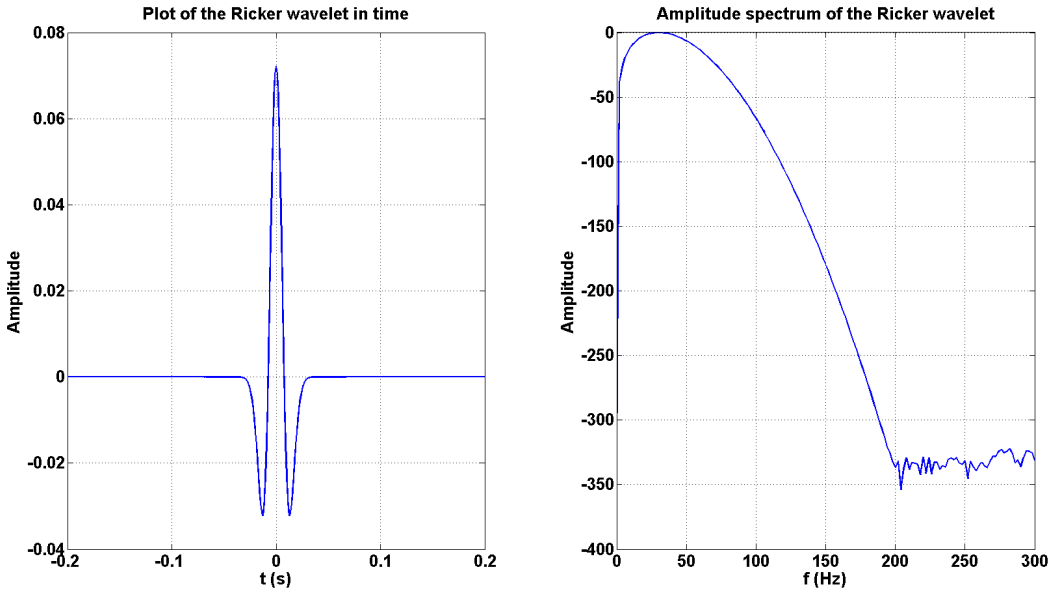

Figure 6.2: Plot of a 30 Hz Ricker wavelet used to construct a synthetic seisimc trace and its corresponding frequency spectra.

where the amplitude goes to zero due to the condition given in Equation 6.11. Depending on the polarity of the reflection and the ghost event, the form of the frequency spectra will also behave differently, which can be seen in the sine and cosine terms of Equations 6.9 and 6.14. Additionally, the spacing of these notches is also given by Equation 6.11. This effect is often referred to as Spectral Notching, and can cause potential errors when interpreting the spectral content of seismic data.

A synthetic seismic trace can be modeled using the convolution operation

$$s(t) = r(t) * w(t), \tag{6.15}$$

where $s(t)$ is the synthetic seismic trace, $r(t)$ is a synthetic reflectivity, and $w(t)$ is an arbitrary wavelet (Aki and Richards, 1980). Figures 6.2 through 6.5 shows two synthetic seismic traces that were created using Equation 6.15. Figure 6.2 shows a 30 Hz Ricker wavelet that was used for $w(t)$ and its corresponding frequency spectra. Note that for this spectra, there are no notches below the noise floor of the spectra, and the dominant frequency is located around the 30 Hz position as expected. Figures 6.3 and 6.4 shows the reflectivity

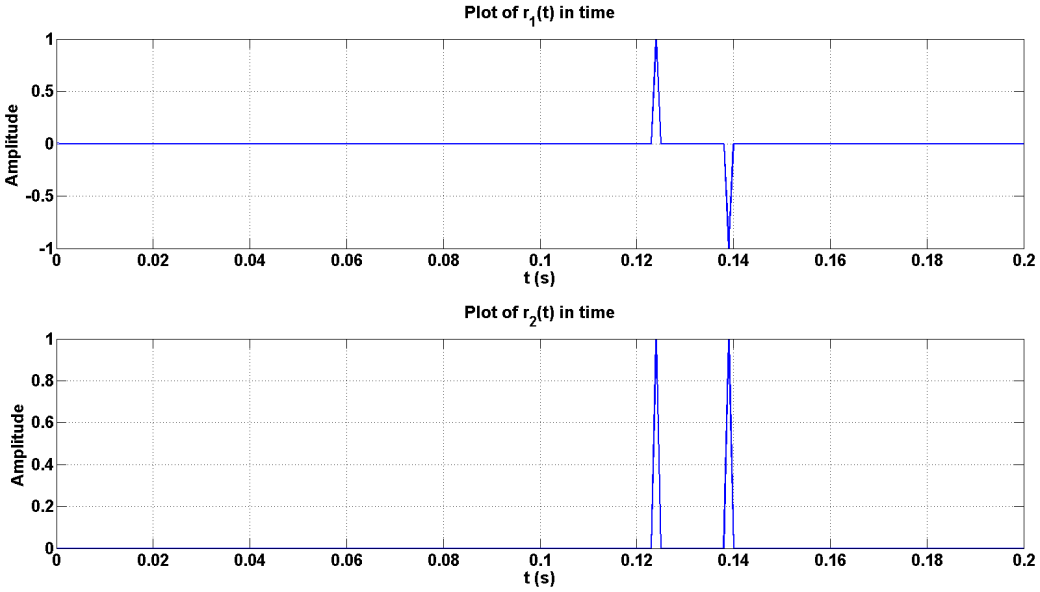

Figure 6.3: Plot of the reflectivities used to create a synthetic seismic trace. The first event in each plot is the reflection event, and the second event is the ghost. Note the difference in polarity of the second event in each of the plots.

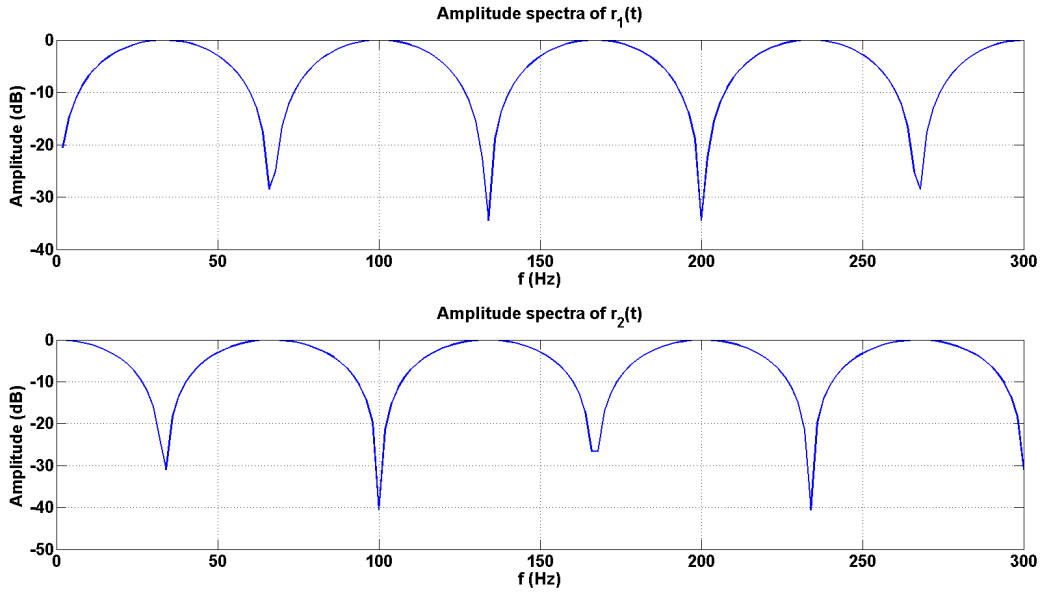

Figure 6.4: Plot of the amplitude spectra of the reflectivities used to create a synthetic seismic trace. The first reflectivity $r_1(t)$ follows the form of a sine function, which was predicted in Equation 6.14, and the second reflectivity $r_2(t)$ follows the form of a cosine function, which was predicted by Equation 6.9.

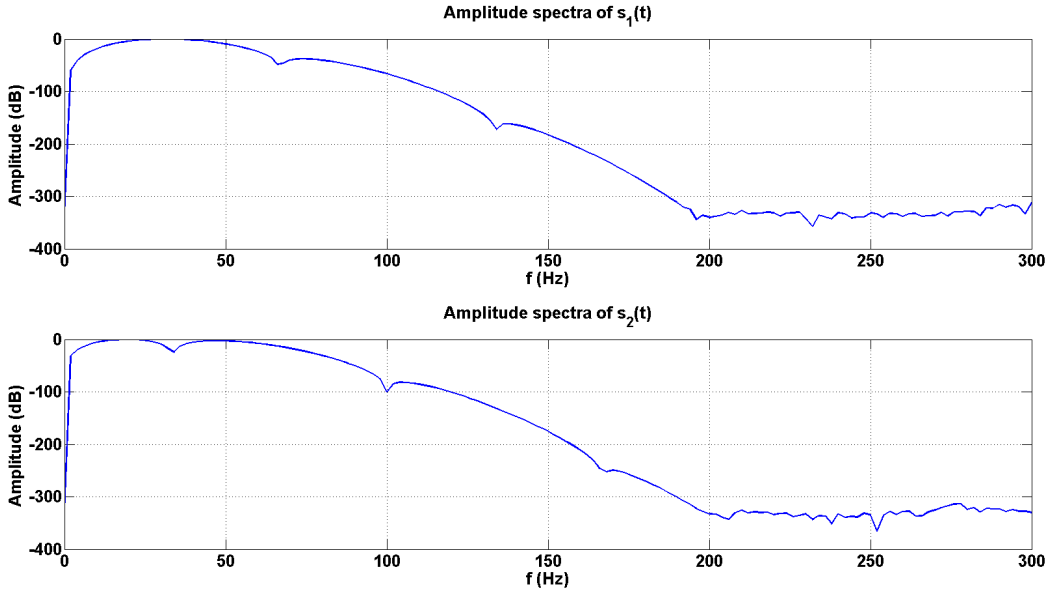

Figure 6.5: Frequency spectra of the synthetic seismic traces created using Equation 6.15 with the Ricker wavelet in Figure 6.2, and with the reflectivities in 6.3. Note that in each case the locations of the notches and the form of the final frequency spectra depend on the amplitude polarity of the second event in the reflectivities.

functions that were used for $r(t)$ in Equation 6.15. The first event in both of these spectra represents the arrival time of the reflection, and the second event is the arrival time of the ghost. Note that we used two different reflectivities for this model: $r_1(t)$ is a reflection event where the ghost polarity is negative, and $r_2(t)$ is a reflection event where the ghost polarity is positive. When these reflectivities are convolved with the Ricker wavelet, as per Equation 6.15, the frequency spectra shown in Figure 6.5 is obtained. When compared to the original Ricker wavelet spectrum in Figure 6.2, the presence of notching becomes apparent in Figure 6.5. These notches are a result of the convolution of $r(t)$ with $w(t)$ in Equation 6.15. Since $r(t)$ is dependent on the polarity of the reflection and the ghost events, which can be seen in Figure 6.3 and 6.4, the notches in amplitude spectra seen in Figure 6.5 are also dependent on the polarity of the events. Therefore for events that occur in real data, we should ex[ect to observe notching that is dependent on the polarity of the events that arrive at the geophone. Careful observation of Figure6.5 shows a clear shift in the notches depending on $r(t)$, however

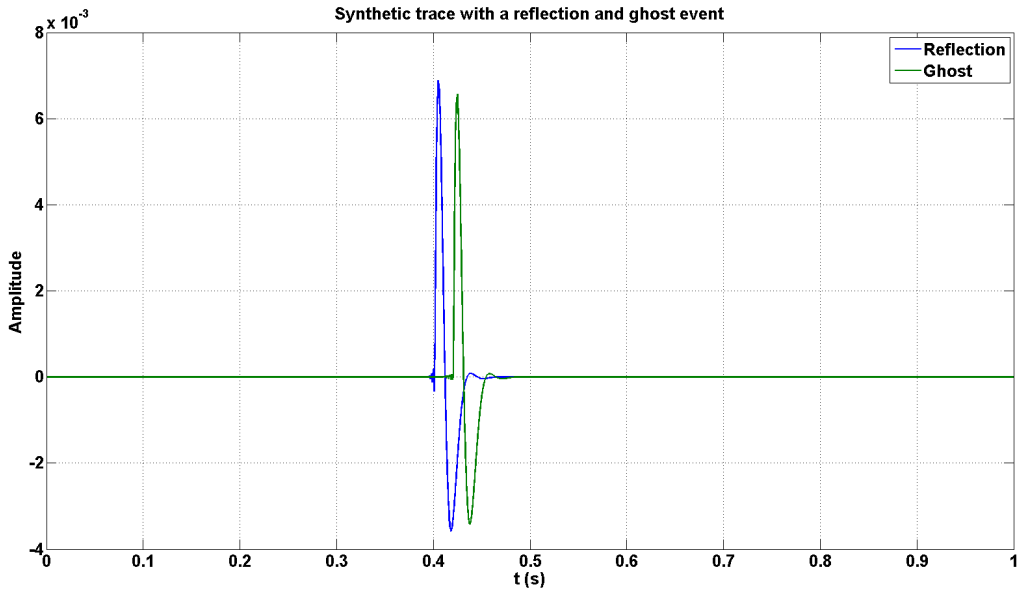

Figure 6.6: Synthetic seismic trace containing a reflection event and its ghost. For the trace modeled in this scenario, the source is buried at a very shallow depth, and thus the events are very closely spaced.

the overall form of the frequency spectra is similar to that of the original wavelet in Figure 6.2. Therefore, it would not be unreasonable to assume that the polarity of the events will shift the position of the nothces in the final frequency spectra. For the remainder of this discussion, we will only consider events that have the same polarity.

6.2 Modeling Spectral Notching

Figure 6.6 shows a synthetic seismic trace that was modeled using the scenario shown in Figure 6.1. For the trace shown here, the source was buried at a depth close to the surface. From the geometry shown in Figure 6.1 it can be seen that if the source is buried close to the surface, the ghost and the reflection events will be closely spaced since the up-going wave from the source does not have to travel far before reflecting off of the free surface. The corresponding frequency spectra of this trace, which can be seen in Figure 6.7, shows the effect of the ghost on the frequency content of a reflection event.

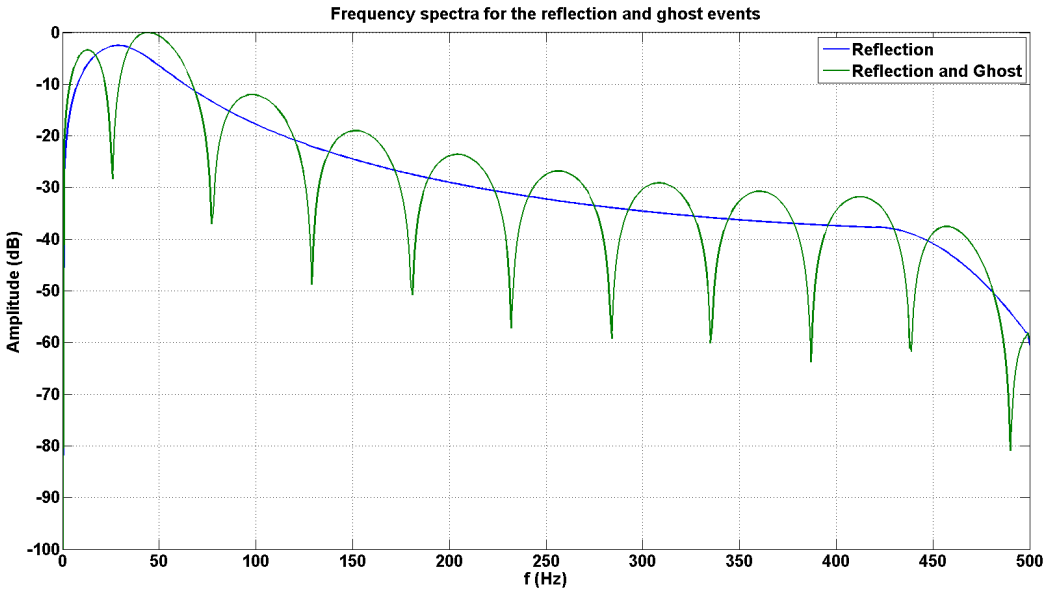

Figure 6.7: Frequency spectra of the trace(s) shown in Figure 6.6. The reflection event without the ghost is shown in blue, and the reflection event including the ghost is shown in green. Note the presence of spectral notching when the trace contains the ghost event as well.

Alternatively, Figure 6.8 shows a synthetic trace that was also modeled using the scenario shown in Figure 6.1, however the source has been buried much deeper in this particular model. The frequency spectra corresponding to this trace, which can be seen in Figure 6.9, shows a much more narrow spacing of the spectral notches than that observed in the previous scenario. Since the source has been buried much deeper in this particular model, the ghost requires more time to travel back to the surface, and thus Δt_g in Equation 6.9 is larger in this case. Based on the zero-condition shown in Equation 6.11, it would be expected that the notches will be much more closely spaced for events that occur at larger time intervals. In practice, and in this study in particular, seismic sources tend to be buried at a depth that is close to the surface; the largest burial depth encountered in this study was approximately 15 meters. Taking this into consideration, it may be more reasonable to expect to see notching similar to that of the scenario shown in Figures 6.6 and 6.7.

Note that the notching effect observed here is not unique to ghosts in seismic data.

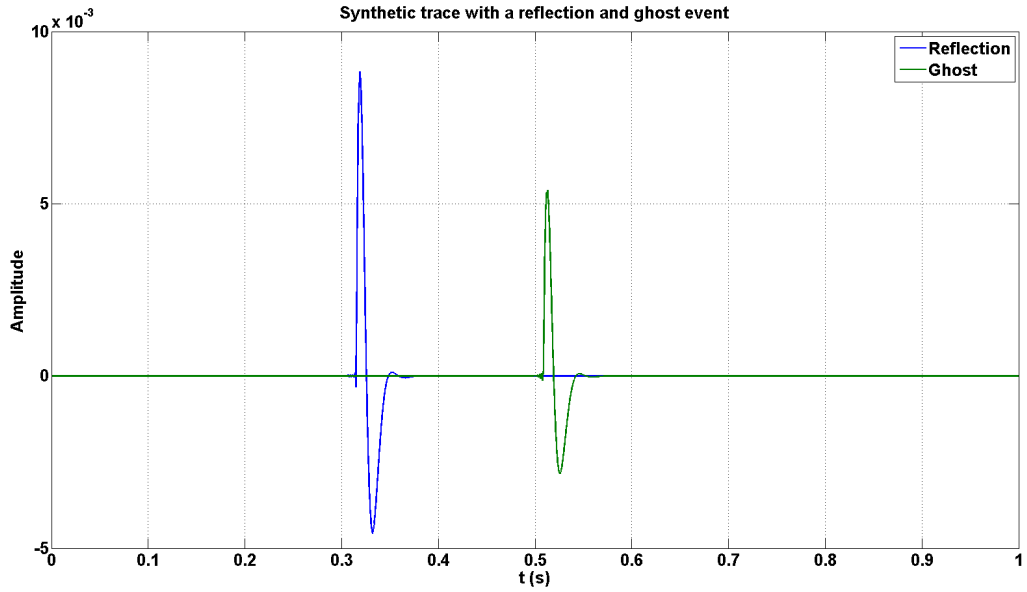

Figure 6.8: Synthetic seismic trace containing a reflection event and its ghost. For the trace modeled in this scenario, the source is buried at a deeper depth than that of Figure 6.6, and thus the events are more widely spaced since the up-going wave has to travel further to reach the free surface.

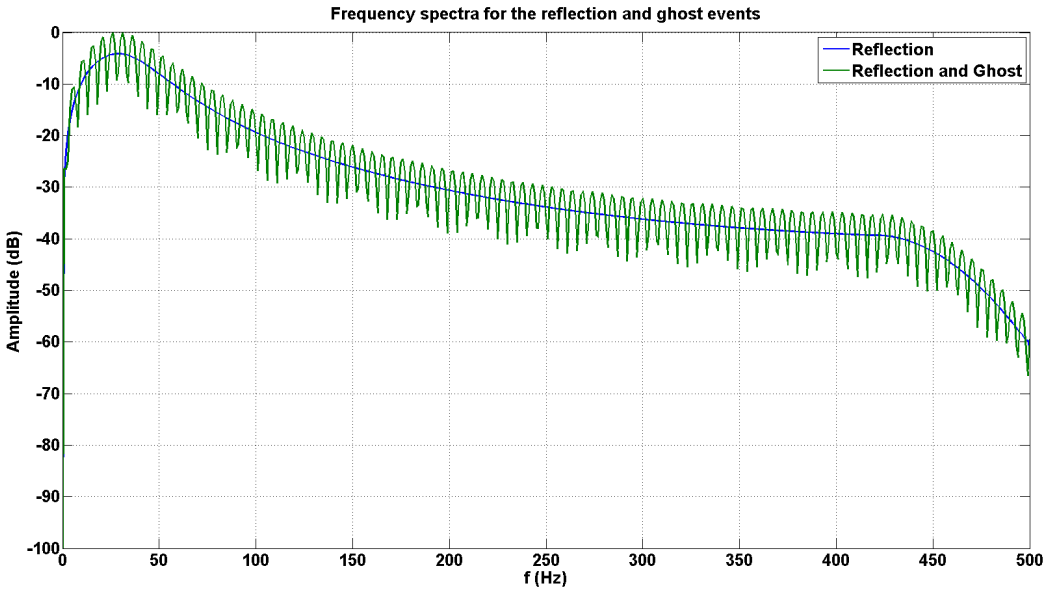

Figure 6.9: Frequency spectra of the trace(s) shown in Figure 6.8. In this case the notches are narrower as the events in the time domain are more widely spaced than the scenario modeled in Figure 6.6.

Any trace containing multiple events, similar to the traces seen in Figures 6.6 and 6.8, will produce notches in the frequency spectra. These events include multiples, ghosts, an any other disturbances sensed by the geophones that are not part of the desired data (Hatton et al. 1986). The data used in this study was not processed in any way, and analysis was carried out on raw data. Therefore notching should be expected in all the frequency spectra obtained in this study.

We expected this notching effect to cause significant deviations between our models and measured data, because we did not include the free surface in any of our models. Without a free surface in the model, we cannot account for events such as multiples or ghosts, and thus we are not taking into account any sort of effects that the free surface will have on the frequency spectra of our acquired data.

6.3 Examining the Effects of Spectral Notching on Data

The majority of the data analysis in this study was carried out in a window that contained the reflection data. In order to determine the effect of the source ghosts and other notching effects, the spectral content of a source from each experiment was analyzed within the window shown in Figure 6.10. The top of this window, which can be seen in blue in Figure 6.10, was located at the base of the first breaks. The bottom of the window was located at 2 ms into the shot record as there was no reflection data observed after this point. Ideally, this window would only contain the reflection data, however as mentioned before there are likely multiples and other events included in this window as well.

The frequency spectra corresponding to the data in this window can be seen in Figure 6.11 for the Hussar 2011 data, and Figure 6.12 for the Priddis 2012 data. In both of these figures, spectral notching is apparent across all frequencies as expected. In this study, the dominant frequency of the sources is of particular interest, and based on these figures it appears to be difficult to pinpoint precisely where the dominant frequency lies when this notching is

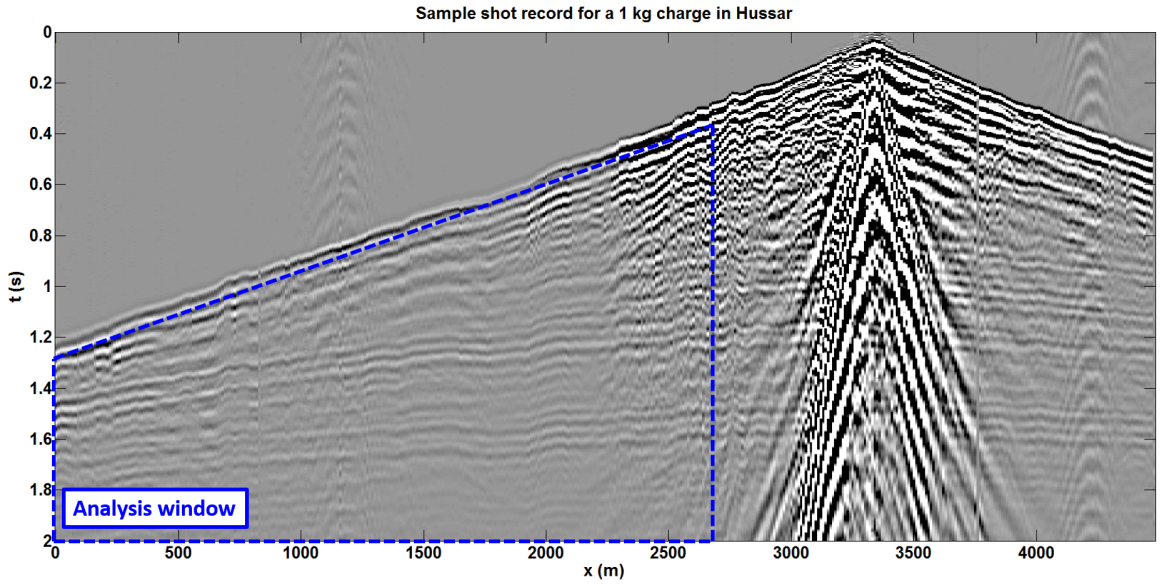

Figure 6.10: Analysis window (shown in blue) used for determining the effect of spectral notching. The top of the window began at the bottom of the first breaks and went to the end of the record; the portion of data near the source was ignored in this case, as the models that were investigated in this study are not able to make predictions about waves near the source.

present. Figure 6.7 shows a model where the dominant frequency of the reflections have been buried by a notch, and the dominant frequency of the entire spectra has been shifted. Given the geometry of the model that created this spectra, it is the most likely scenario to be encountered in the data as the sources were buried fairly close to the surface. If this scenario is encountered, it is entirely possible that the measured dominant frequency of the sources are erroneous; this introduces a potential source of error in this experiment.

6.4 Chapter Summary and Conclusions

- Spectral notching has been observed in the Hussar 2011 and Priddis 2012 data sets.
- We did not account for the free surface in any of our models, and thus we cannot account for effects like multiples and source ghosts that give rise to spectral notches.

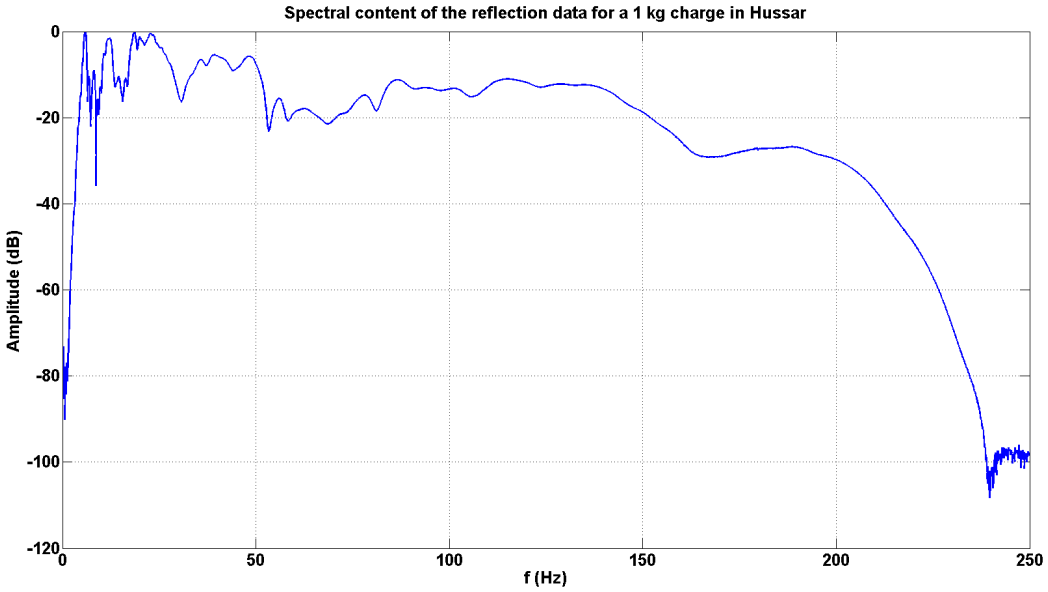

Figure 6.11: Frequency spectra obtained from the reflections in the Hussar 2011 data set. The notches in this spectra are most likely caused by source ghosts and multiples, and other events that may be present within the data. These notches can make it difficult to locate the dominant frequency of the source, which can cause errors with the interpretation of the results of this study.

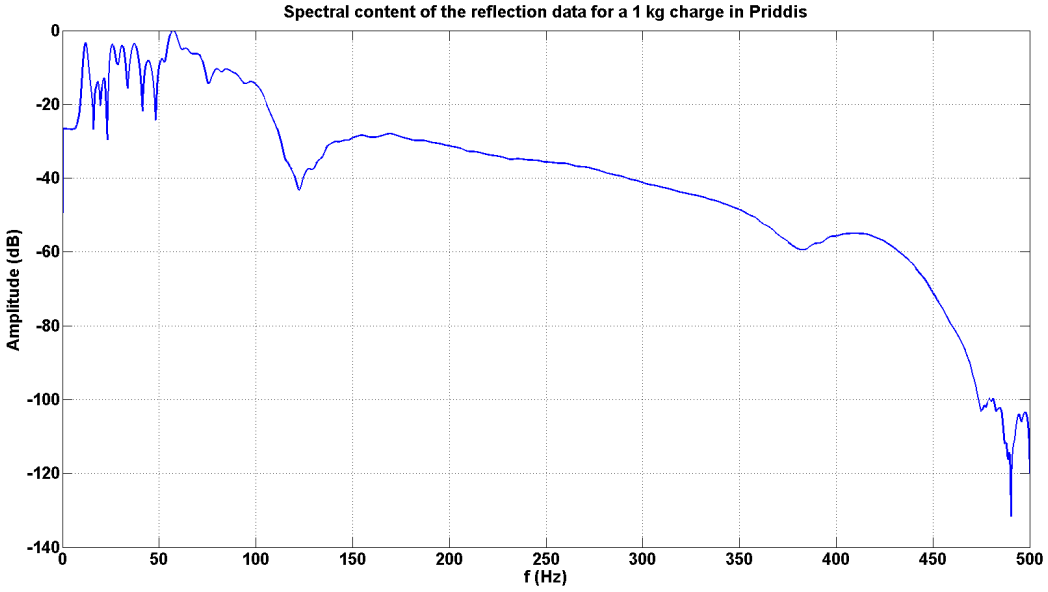

Figure 6.12: Frequency spectra obtained from the reflections in the Priddis 2012 data set. The notches in this spectra are similar to what was observed in Hussar 2011 (Figure 6.11.

- The causes of these notches have not been identified at this point, however, they are most likely caused by source ghosts and multiples.
- The notches introduce a potential source of error as it is possible for one of them interfere with dominant frequency in the frequency spectra.

Chapter 7

Application of the SHCM to real data

The relationship between charge size and cavity radius is an integral part of the SHCM if we wish to apply it to data obtained in the field (Sharpe, 1942). In our discussion of the SHCM we observed a cubic relationship between power and cavity radius, which can be seen in Figure 2.10. Based on this observation, if a relationship between charge size and shot power can be established, it may be possible to determine some sort of a link between charge size and the cavity radius in the SHCM.

7.1 Establishing a Link Between Charge Size and Cavity Radius

We began our analysis by computing the shot power for each charge in both the Hussar 2011 and Priddis 2012 field experiments. The power was computed over the vertical component of the geophones, and we chose a time window that only encompassed the first breaks and the reflections, as the SHCM cannot predict the nature of the energy outside of these windows (Sharpe, 1942). Figure 7.1 shows an example of a shot record and the window over which we computed the power, and conducted the frequency analysis of each shot record. The power was computed using the equation

$$P = \frac{\sum s^2}{N}, \tag{7.1}$$

where P is the power, s is the trace, and N is the length of the trace. Note that the power in this case is unitless. The frequency spectra were obtained using the function **fxtran** in the CREWES MATLAB toolbox.

Figure 7.2 and 7.3 shows a plot of the computed shot power that results from each charge size. Both the Hussar 2011 and Priddis 2012 data sets display a relationship between charge size and shot power that is approximately linear, with only slight deviations from the linear

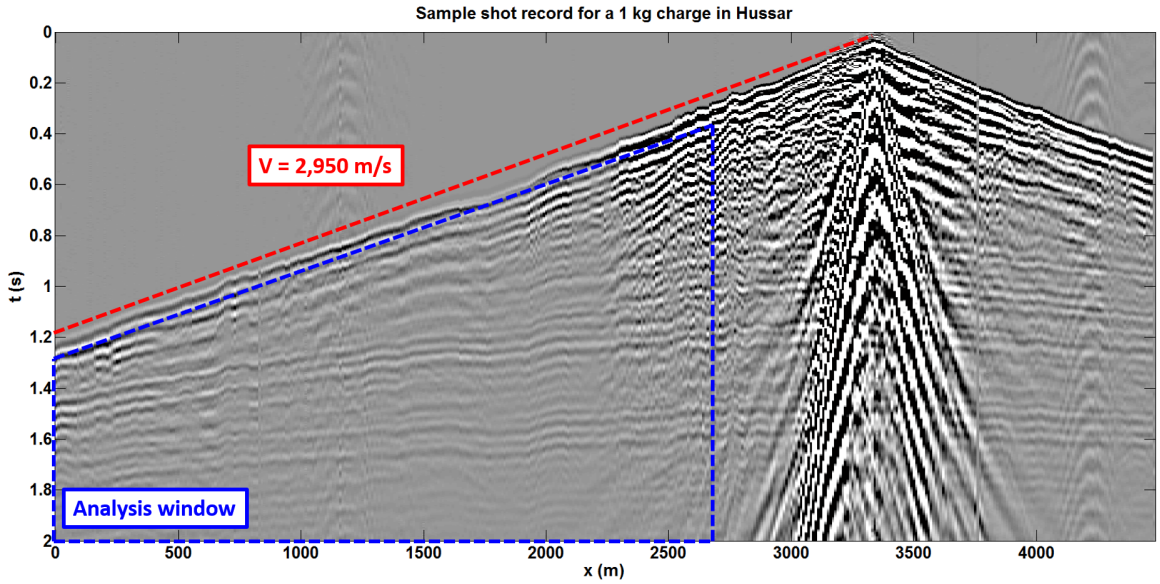

Figure 7.1: An example shot record for the one kilogram charge in the Hussar 2011 data set. The window over which the power and frequency analysis was conducted is shown in blue, and the line used to determine the wave speed is shown in red. Note that this red line is the slope of the first break line.

best fit line. This suggests that the relationship between shot power and charge size could potentially be linear within the ranges of charges that we have used in these experiments. Note however that we have only used a narrow range of charges in this experiment, and that we are dealing with a limited dataset in terms of the total number of charges that we used. Therefore, we may have to collect more data before we can draw any sort of reliable conclusions regarding the relationship between charge size and shot power.

We had established a cubic relationship between the cavity radius in the SHCM and the power, such that

$$P \simeq a^3, \tag{7.2}$$

where a is the cavity radius in meters, and P is the power. Figures 7.2 and 7.3 suggest that the relationship between charge size and measured shot power may be linear in nature, such that

$$P \simeq m, \tag{7.3}$$

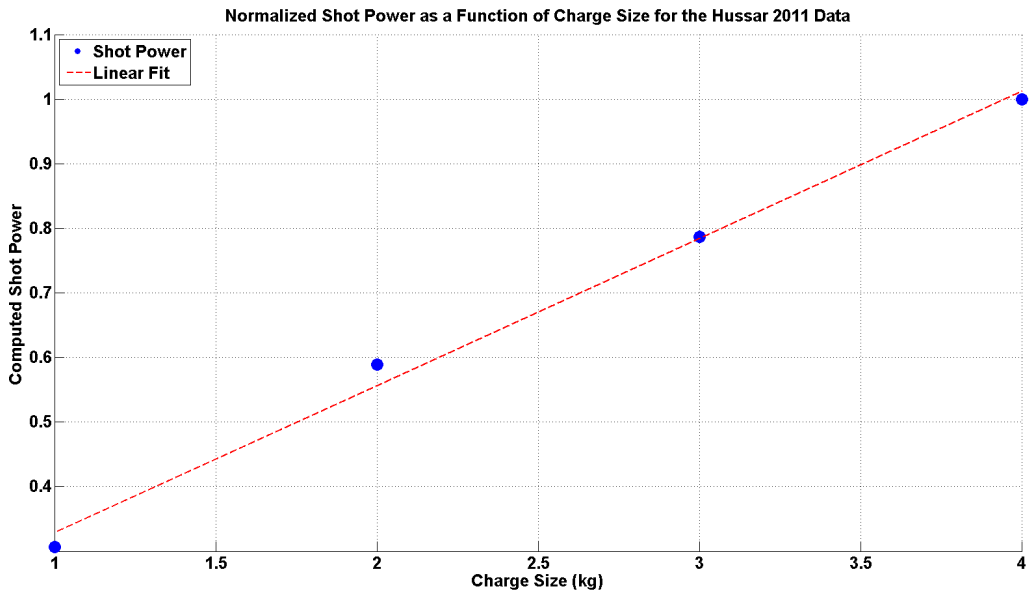

Figure 7.2: Normalized shot power as a function of the charge size in the Hussar 2011 dataset. Note that the power in this case has been normalized using the maximum shot power for the group of shots at the first location in the Hussar 2011 data set. There appears to be a linear relationship between charge size and the resulting power of the shot however, this is something that should be studied in greater detail before any solid conclusions can be made.

where m is the charge size in kilograms. If we assume that the measured power is that of the SHCM, we can combine Equations 7.2 and 7.3 to obtain the relationship,

$$m = ca^3, \tag{7.4}$$

where c is a proportionality constant with units of a kilogram per cubic meter. Recall that the frequency of SHCM is given by

$$f_o = \frac{\omega}{2\pi} = \frac{\sqrt{2}v}{3a}, \tag{7.5}$$

where a is the cavity radius, v is the P-wave speed in the medium, ω is the angular frequency, and f_o is the dominant frequency (Sharpe, 1942). By combining Equations 7.4 and 7.5 we can obtain the expression

$$f_o^3 = c\left(\frac{\sqrt{2}v}{3}\right)^3 \frac{1}{m}. \tag{7.6}$$

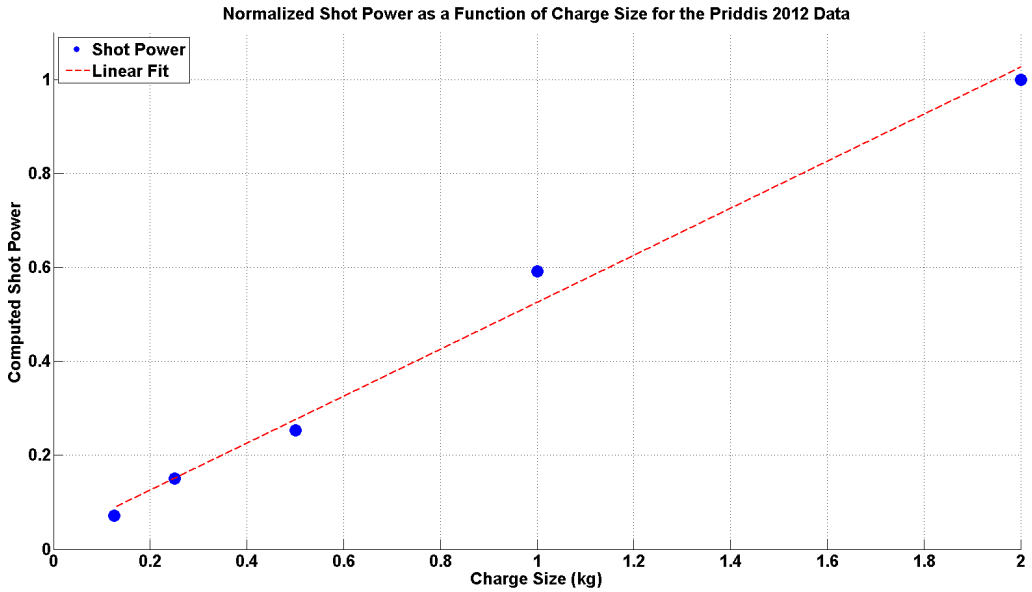

Figure 7.3: Normalized shot power as a function of the charge size in the Priddis 2012 dataset. Note that the power in this case has been normalized using the maximum shot power for the Priddis 2012 data set. There appears to be a linear relationship between charge size and the resulting power of the shot however, this is something that should be studied in greater detail before any solid conclusions can be made.

Equation 7.6 shows that if the cube of the measured dominant frequency is plotted against the inverse of the charge size, the resulting plot should be a straight line of intercept zero, and a slope of

$$S = c\left(\frac{\sqrt{2}v}{3}\right)^3, \tag{7.7}$$

where c is the proportionality constant, and S is the slope of the previously discussed plot. After a plot of the cube of the measured dominant frequency as a function of the inverse charge has been determined, the value of c can be computed using the following equation:

$$c = S\left(\frac{3}{\sqrt{2}v}\right)^3. \tag{7.8}$$

Figures 7.4 and 7.5 shows a plot of the cube of the measured dominant frequency as a function of the inverse charge size for both the Hussar 2011 and Priddis 2012 datasets. In both data sets, the plots appear to be linear with only slight deviations from the line of best fit.

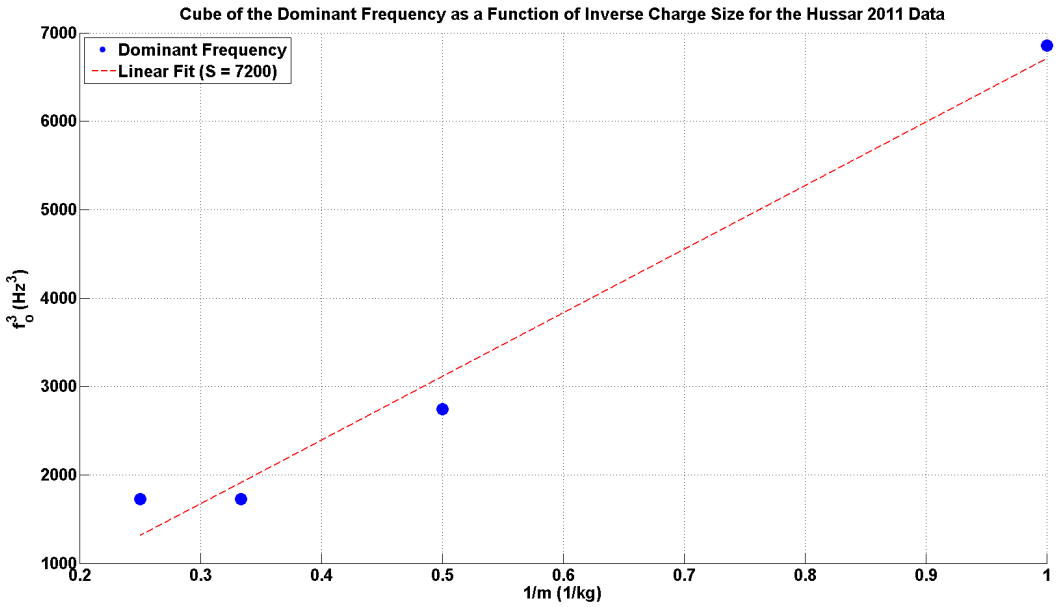

Figure 7.4: A cube of the dominant frequency as a function of the inverse charge size for the Hussar 2011 data set. Note that for this calculation, the same charges from the power computation in Figure 7.2 were used. Based on this figure, there is evidence to suggest that the relationship between the cube of the dominant frequency and the inverse of the charge size is linear.

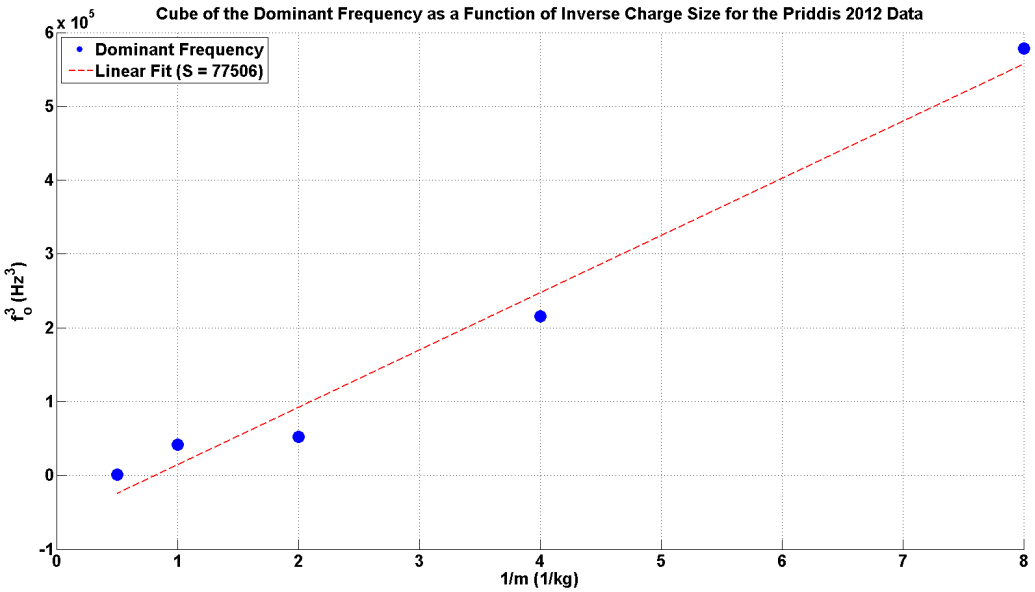

Figure 7.5: A cube of the dominant frequency as a function of the inverse charge size for the Priddis 2012 data set. Note that for this calculation, the same charges from the power computation in Figure 7.2 were used. Based on this figure, there is evidence to suggest that the relationship between the cube of the dominant frequency and the inverse of the charge size is linear.

One of the most important aspects of the SHCM when trying to apply it to real data is establishing a link between charge size and the cavity radius. From this portion of our study, we were able to establish a link between charge size and cavity radius by examining the power spectra that resulted from the theoretical portion of the SHCM, and the data that we obtained in the field. Ziolkowski examined various radial stress patterns that resulted from dynamite of varying charge sizes (Ziolkowski, 1993). He arrived at a cube-root scaling of

$$a = CM^{1/3}, \tag{7.9}$$

where a is the cavity radius and, C is medium-specific constant, and M is the charge size. Since we both arrived at this relationship using differing techniques, there is strong evidence to suggest that the link between charge size and cavity radius cubic in nature.

7.2 Determining the c-Value

After obtaining the plots in Figure 7.4 and 7.5, we used Equation 7.8 to determine the value of c for each individual data set. The c-values that we obtained where

$$c_{Hussar} = 1.0 \times 10^7 \ m^{-3}, \tag{7.10}$$

for the Hussar 2011 data set, and

$$c_{Pridds} = 2.0 \times 10^7 m^{-3}, \tag{7.11}$$

for the Priddis 2012 data set. We determined the value of the wave speed v, by using the the slope of the first break line as shown in Figure 7.1. For the Hussar 2011 dataset we obtained a value of 2750 m/s, and for the Priddis 2012 dataset we obtained a value of 3500 m/s. We then used this c-value in Equation 7.4 to determine the cavity radii that corresponded to each charge size; and then proceeded to use these cavity radii in the SHCM to make a series of theoretical plots of the frequency spectra for each data set. Figure 7.6 shows the geometry of the Sharpe model that we used to calculate the theoretical frequency spectra for each sensor in the survey. After obtaining individual spectra for each modeled sensor in the experiment, they were all combined to produce a theoretical frequency spectra for each data set. The theoretical frequency spectra obtained from this calculation can be found in Figures 7.7 and 7.8.

To summarize, the method for calculating the value of c is as follows.

1. Determine the value of the wave speed from the shot record
2. Compute dominant frequency as a function of the charge size
3. Plot the cube of the dominant frequency with respect to inverse charge size
4. Determine the slope of this plot
5. Use Equation 7.8 to determine the value of c

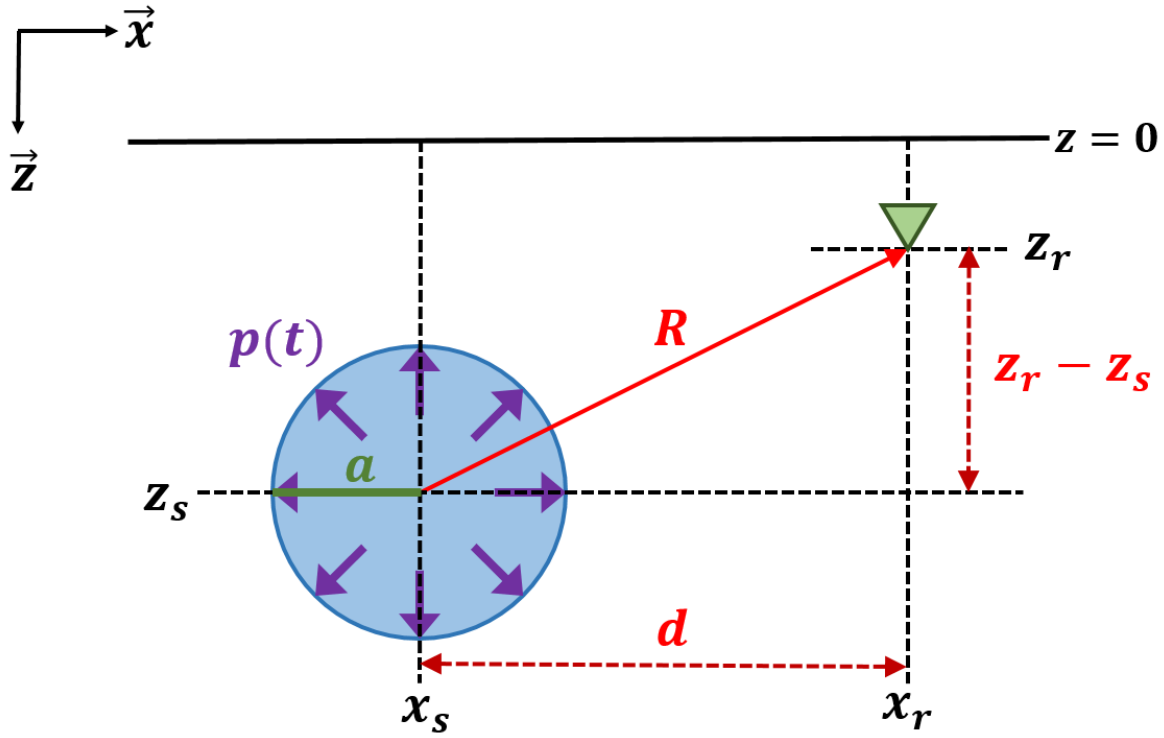

Figure 7.6: Figure showing the geometry of the SHCM that we used to construct the theoretical frequency spectra for each sensor, which we combined to get the total spectra seen in Figures 7.7 and 7.8.

6. Use this c-value in Equation 7.4 to determine cavity radii

7. Use these cavity radii to produce frequency spectra from the SHCM

7.3 Amplitude Response and the SHCM

Figures 7.9 and 7.10 shows the frequency spectra obtained from the Hussar 2011 and Priddis 2012 datasets respectively. Examination of these data sets shows an increase in the amplitude of the waves emitted by the source for larger charge sizes, which is predicted by the SHCM. Habberjam and Whetton conducted a survey whereby a large number of varying sized explosives were detonated, in an attempt to establish a relationship between the amount of charge used and the amplitude response (Habberjam and Whetton, 1951). From this body

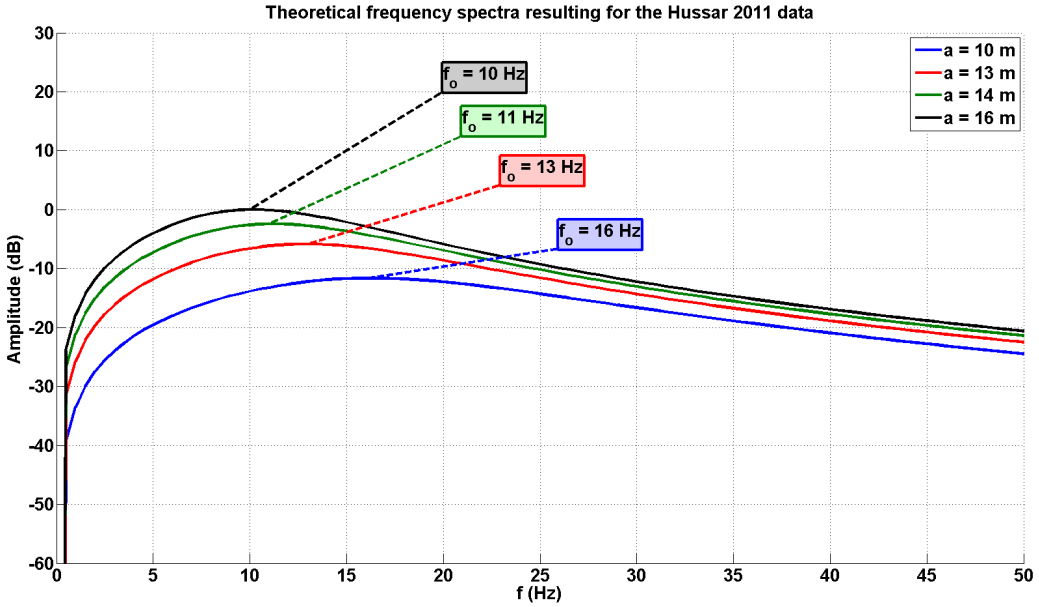

Figure 7.7: Theoretical frequency spectra obtained from the SHCM, using the charge sizes from the Hussar 2011 experiment,the calculated c value from Equation 7.8, and a wave speed v of 2000 m/s.

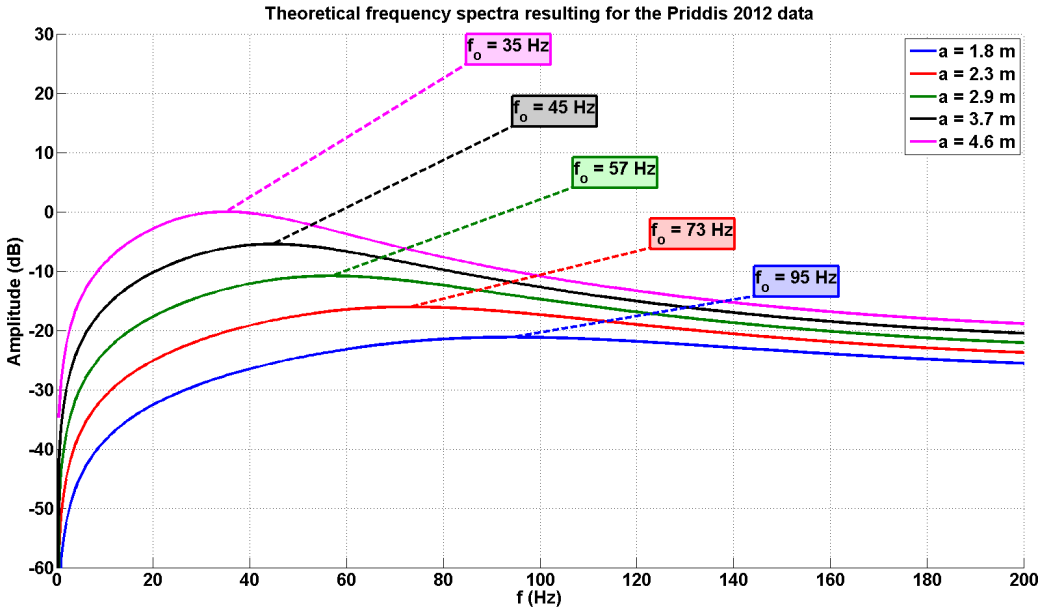

Figure 7.8: Theoretical frequency spectra obtained from the SHCM, using the charge sizes from the Priddis 2012 experiment, the calculated c value from Equation 7.8, and a wave speed v of 2500 m/s.

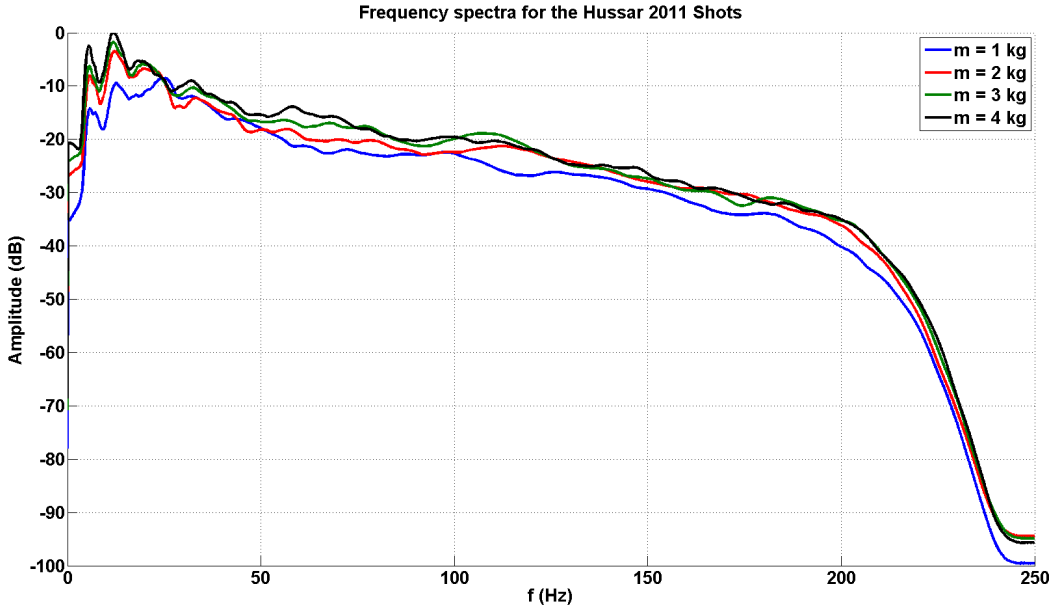

Figure 7.9: Frequency spectra obtained from the Hussar 2011 test shots. Note that the overall amplitude increases with larger charge sizes, but the dominant frequency decreases with bigger charges. This matches the predictions of the SHCM.

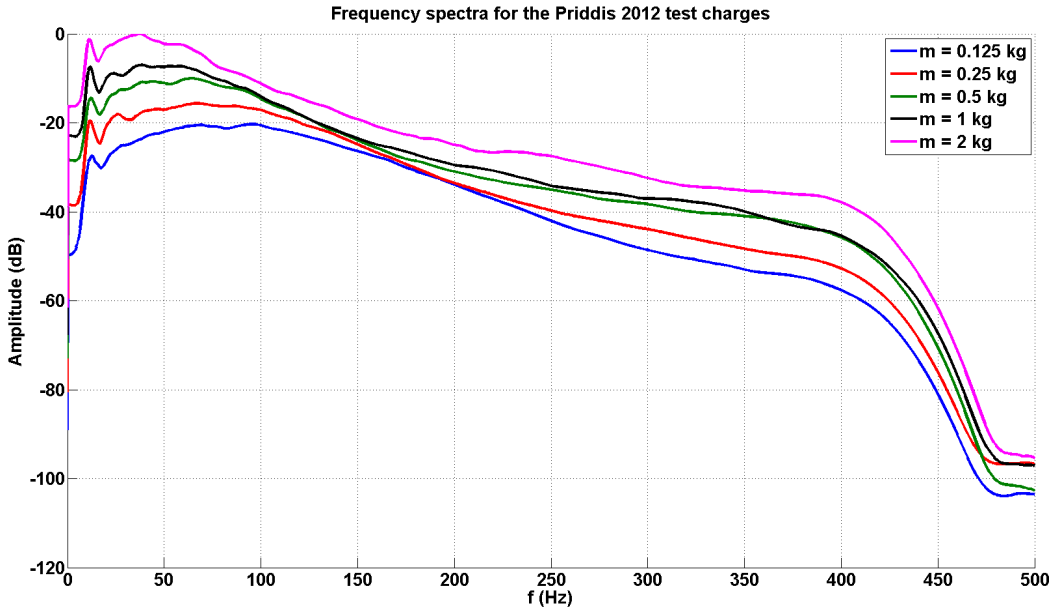

Figure 7.10: Frequency spectra obtained from the Priddis 2012 test shots. Note that the overall amplitude increases with larger charge sizes, but the dominant frequency decreases with bigger charges. This matches the predictions of the SHCM.

of work, they were able to establish a relationship between charge size and amplitude, which was of the form

$$C = QA^{1.242}, \tag{7.12}$$

where C is the amount of charge, Q is a factor ranging from 1 and 3, and A is the amplitude. This study found that the charge size was proportional to the amplitude response of the medium, which coincides with our observations from our study, which in turn suggests that the SHCM can be used to predict the amplitude response of charges detonated in the field.

There are currently numerous bodies of work that have been conducted using dynamite which attempt to explore the nature of the craters left behind after explosions. Sharpe is very commonly referenced in these studies, as the SHCM was one of the first models to lay some sort of theoretical groundwork for future studies of this nature. The most important factor in the SHCM is the cavity size, however, it is not very well understood at this point whether or not the size of the cavity is representative of the volume of subsurface that is displaced by an explosion. Nicholls and Duvall explored the effect of charge diameter on the power of explosives for the U.S Department of Interior (Nicholls and Duvall, 1965). Their publication focuses mainly on the performance of three different types of explosive material: Pentolite, Semigelatin dynamite, and AN-FO prills. A series of these test charges ranging in size was detonated within the subsurface and their explosive power was measured, along with several other subsurface parameters. They did find that larger charge sizes produced higher amplitude responses for each type of explosive which coincides with our observations as well, but of particular interest to the SHCM is the diameter of the cavities that were left over after the explosions. They found that larger charge sizes produced bigger craters, regardless of the type of charge that they used, which yields some very interesting results about the nature of the cavities lefter after an explosion. These observations suggest that the hollow cavity in the SHCM may also hold some physical significance in practice. It may be worth investigating this phenomenon in future research projects.

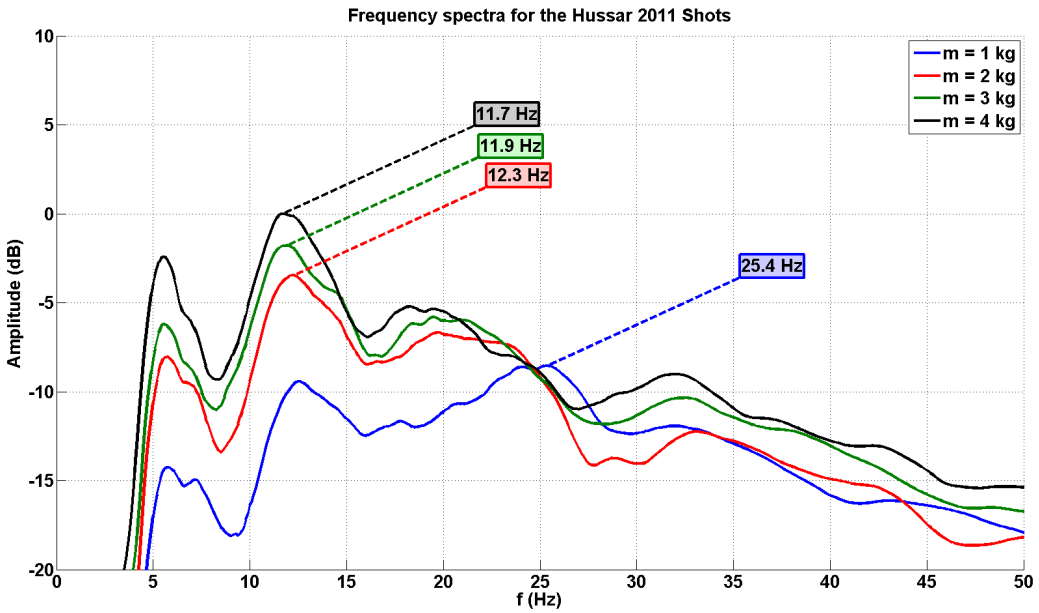

Figure 7.11: Closer view of the peaks of the frequency spectra obtained from the SHCM for the Hussar 2011 data. Both the predicted amplitudes and dominant frequency are approximately the same as that of the measured spectra, with the exception of the one kilogram charge.

7.4 Frequency Content and the SHCM

Figures 7.11 and 7.12 shows a closer view of the peaks of the frequency spectra that was obtained from the Hussar 2011 and Priddis 2012 data. These plots have been displayed along with their corresponding theoretical spectra obtained from the SHCM. Additionally, Tables 7.1 and 7.2 contain a summary of the peak amplitude and dominant frequency of both the theoretical and measured spectra, for both data sets. Note that in these tables "A" denotes to the amplitude data, while "f" denotes the frequency data. Additionally, the subscript "M" is used to denote the measured data, while the subscript "T" is used to denote the theoretical predictions. The form of the frequency spectra that we have obtained in these figures, suggest that the pressure pulse $p_3(t)$ that we have used in our theoretical calculations produce a frequency spectra that follows the form of that obtained from real data. In both scenarios, the SHCM appears to be able to make reasonably accurate predictions of the

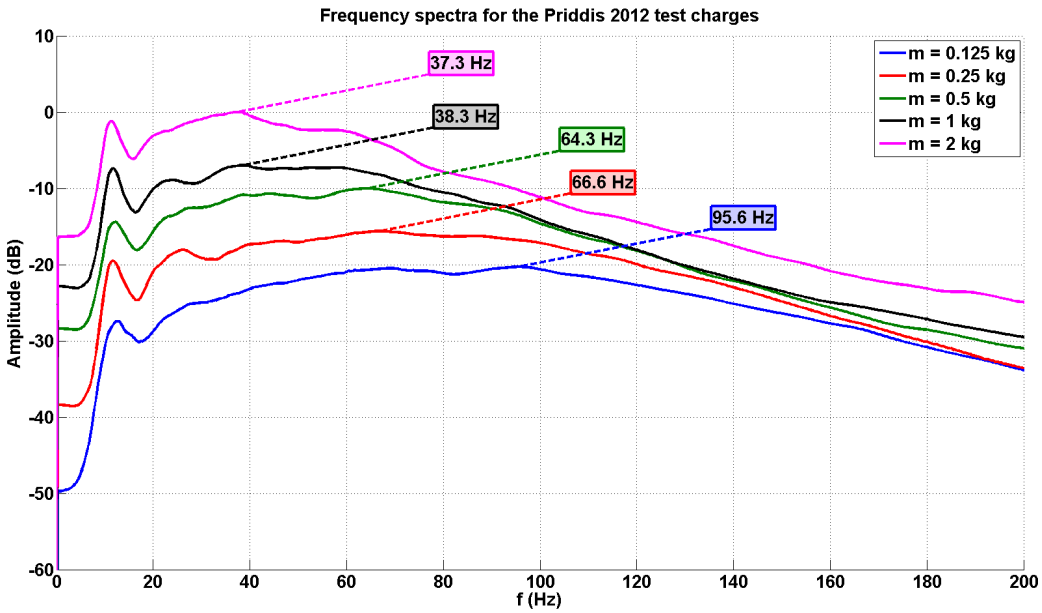

Figure 7.12: Closer view of the peaks of the frequency spectra obtained from the SHCM for the Priddis 2012 data. Both the predicted amplitudes and dominant frequency are approximately the same as that of the measured spectra, with the exception of the one kilogram charge.

peak amplitude and dominant frequency of data obtained in the field. This confirms that the SHCM could be used to predict the features of the frequency spectra for future data sets, provided that some information about the subsurface, such as the wave speed and the c-value are already known. If the value for c and v can be determined for a specific region, this information could be used to more accurately determine survey parameters in that same region for future studies. These parameters include the size of the charges that you need to use to produce a specific amplitude and dominant frequency.

7.5 Limitations and Experimental Uncertainties

There are some uncertainties/inaccuracies that may cause some problems for future work involving the SHCM. At best, we were only able to operate under the assumption that the relationship between charge size and shot power (shown in Figures 7.2 and 7.3) is linear.

Hussar 2011 Data Summary				
m (kg)	$f_M(Hz)$	$f_T(Hz)$	A_M	A_T
1	25.4	16	-8	-11
2	12.3	13	-4	-7
3	11.9	11	-3	-3
4	11.7	10	0	0

Table 7.1: A summary of the peak amplitudes and dominant frequency the theoretical and measured frequency spectra for the Hussar 2011 data. Note that in these tables "A" denotes to the amplitude data, while "f" denotes the frequency data. Additionally, the subscript "M" is used to denote the measured data, while the subscript "T" is used to denote the theoretical predictions.

Priddis 2012 Data Summary				
m (kg)	$f_M(Hz)$	$f_T(Hz)$	A_M	A_T
0.125	95.6	95	-20	-20
0.25	66.6	73	-17	-17
0.5	64.3	57	-10	-10
1	38.3	43	-8	-7
2	37.3	35	0	0

Table 7.2: A summary of the peak amplitudes and dominant frequency the theoretical and measured frequency spectra for the Priddis 2012 data. Note that in these tables "A" denotes to the amplitude data, while "f" denotes the frequency data. Additionally, the subscript "M" is used to denote the measured data, while the subscript "T" is used to denote the theoretical predictions.

If this is not the case, we cannot use Equation 7.4 to establish a link between charge size and cavity radii, which significantly limits the rest of our predictions. Given the linear trend in Figures 7.2 and 7.3 , it is most likely the case that for the range of charges used in this experiment, the relationship between charge size and shot power is linear. There is also an issue with the determination of c, which is based on the idea that the relationship between the cube of the measured dominant and the inverse charge size is linear. The data from Priddis, seen in Figure 7.10, seems to follow a linear trend. However, the Hussar data which is shown in Figure 7.9, does not seem to follow a linear pattern in any sort of reliable fashion. In order to improve on both of these ideas, it would be advisable to collect a wider range of charge size data in much smaller increments at a variety of different locations. This would help us determine whether or not we approach a linear relationship between power and charge size with a larger variety of charges sizes, and whether or not we approach a liner relationship between the cube of the measured dominant frequency and the inverse of the charge size.

Spectral notching is present in data from both the Hussar 2011 experiment, and the Priddis 2012 experiment. The notching in the low frequencies, seen in Figures 7.11 and 7.12, are of particular interest as they seem to produce the biggest limitation. There are two distinct peaks in the Hussar data set for the one kilogram charge which appears to deviate significantly from the data obtain from the other charges. By definition, the dominant frequency is found where the amplitude is the largest, and thus the peak shown in the figure was the one that is chosen. However, based on the data from the other charges, it would not be unreasonable to assume that the dominant frequency actually lies within the same region as the others. In this experiment, it is very likely that spectral notching has interfered with our data, and thus there may be errors associated with that phenomenon. In the Priddis 2012 data set however, the notch pattern appears to be wider than that of Hussar. In this data set, there is a set of peaks at the lower end of the spectrum, which is followed by a much

broader set of peaks. Again, the dominant frequency was chosen to be the point where the amplitude is maximum, and in this case it is difficult to assess whether or not the notching has caused a misrepresentation in the frequency content of the source. Given the notching that is present, it is entirely possible that it presents an uncertainty in this experiment as well.

7.6 Chapter Summary and Conclusions

- The SHCM predicts an increase in the overall amplitude response of the waves emitted by a source with increasing charge size, which has been verified by experimental observations.
- The SHCM predicts a decrease in dominant frequency with larger charge sizes, which has been verified by experimental observations.
- For both the Hussar 2011 and Priddis 2012 data sets the SHCM was able to make reasonably accurate predictions regarding the amplitude and frequency content of the waves emitted by varying charge sizes.
- The relationship between charge size and cavity radius appears to be cubic in nature, which coincides with both our observation, and that of Ziolkowski in his charge scaling experiment (Ziolkowski, 1993).
- Our method for determining the c-value, which links the charge size and the cavity radius, appears to work for both the Hussar 2011 and Priddis 2012 data sets as the computed values produce reasonably accurate dominant frequency and amplitude predictions.
- Overall, it appears that the SHCM is reasonably effective at making predictions of the amplitude and frequency content of waves emitted by explosive sources, specifically dynamite.

- It would be worthwhile to collect data for a larger range of dynamite explosions to strengthen the hypothesized link between charge size, power, and cavity radius in the SHCM.

Chapter 8

Application of the GBSM to Real Data

The analysis for the GBSM was very similar to that of the the SHCM in methodology, in that we used experimental and subsurface parameters to compute a theoretical frequency spectra of the data using the GBSM. In the SCHM we determined that the cavity radius and the charge size are linked via a proportionality constant. In the GBSM we determined a similar link between Gaussian ball width and charge size. We require a proportionality constant to link the charge size and the Gaussian ball width in this particular model as shown in Equation 3.11, and currently do not have a reliable means of determine it. For the purposes of this study, we used a series of c-values to match the amplitude response of the GBSM with that of the highest amplitude response in the data set, and assumed that was the c-value for that particular data set. Recall that for the Hussar 2011 data we computed a c-value of

$$C_{Hussar} = 1.0 \times 10^7 \ m^{-3}, \tag{8.1}$$

and for the Priddis 2012 data set we determined a c-value of

$$C_{Priddis} = 2.0 \times 10^7 \ m^{-3}. \tag{8.2}$$

Using each of these c-values, and the same values for the subsurface parameters that we used for the SHCM, we computed the frequency spectra of the GBSM for each medium.

The results of this part of the study can be found in Figures 8.1 and 8.2. Recall that the measured data for Hussar 2011 and Priddis 2012 can be found in Figures 7.9 and 7.10. Additionally, Tables 8.1 and 8.2 contain a summary of the results of our GBSM analysis for both the Hussar 2011 and Priddis 2012 data sets. In both data sets were not able to model the amplitude response of the measured data with that of the GBSM. We were also unable to match the dominant frequency of the measured data (shown in Figures 7.11 and 7.12

Hussar 2011 Data Summary				
m (kg)	$f_M(Hz)$	$f_T(Hz)$	A_M	A_T
1	25.4	7	-8	-6.5
2	12.3	5	-4	-3.0
3	11.9	5	-3	-1.3
4	11.7	4	0	0

Table 8.1: A summary of the peak amplitudes and dominant frequency the theoretical and measured frequency spectra for the Hussar 2011 data. Note that in these tables "A" denotes to the amplitude data, while "f" denotes the frequency data. Additionally, the subscript "M" is used to denote the measured data, while the subscript "T" is used to denote the theoretical predictions.

with that of the GBSM (shown in Figure 8.3 and 8.4). Despite being unable to match the amplitude response and the dominant frequency of the measured and theoretical data, the overall form of the frequency spectra in the GBSM appears to match that of the measured data. This suggests that there may be a scaling issue with this model when attempting to use it for the charge sizes in these experiments, and thus we cannot produce significant enough variation in the amplitude and frequency content of the GBSM to match measured data. Aldridge suggests that this model may only be usable for larger explosions, and thus we may not be able to use it for typical dynamite charges used in the field (Aldridge, 2011). This phenomenon may also be a result of an incorrect assumption that a constant links the Gaussian ball width and the charge size; a variable may be required to accurately link Gaussian ball width and charge size. This is something that we would have to investigate further before we can reliably use the GBSM to make predictions about the amplitude and frequency content of waves in practice.

8.1 Chapter Summary and Conclusions

- The GBSM is able to accurately model the features of the frequency spectra obtained from explosive sources used in practice.

Pridids 2012 Data Summary				
m (kg)	$f_M(Hz)$	$f_T(Hz)$	A_M	A_T
0.125	95.6	8	-20	-16.5
0.25	66.6	8	-17	-11.5
0.5	64.3	7	-10	-7.1
1	38.3	7	-8	-3.4
2	37.3	5	0	0

Table 8.2: A summary of the peak amplitudes and dominant frequency the theoretical and measured frequency spectra for the Priddis 2012 data. Note that in these tables "A" denotes to the amplitude data, while "f" denotes the frequency data. Additionally, the subscript "M" is used to denote the measured data, while the subscript "T" is used to denote the theoretical predictions.

- We were not able to match the amplitude response or the dominant frequency of the GBSM with that of the data obtained in both the Hussar 2011 and Priddis 2012 data sets.

- In our calculations, the GBSM made predictions about the dominant frequency that were consistently too low compared to that of the measured data.

- We require further investigation into this issue to determine whether or not this is an issue with scaling within the model.

- It would be worthwhile for us to develop a method to determine the c-value linking Gaussian ball width and charge size.

- We require further investigation to determine whether or not the link between charge size and Gaussian ball width is in fact linked by a constant, rather than a variable.

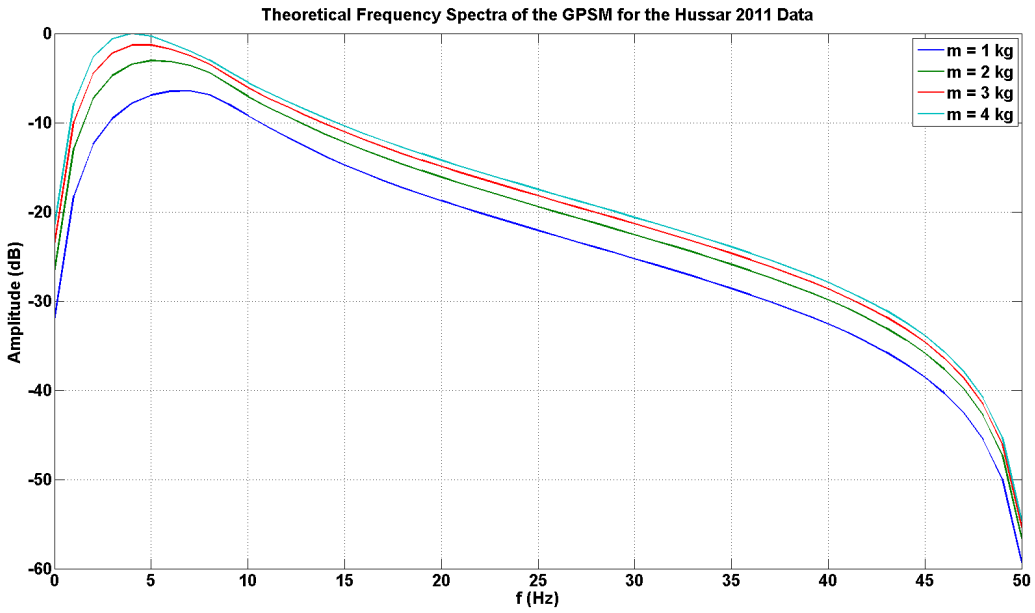

Figure 8.1: Theoretical frequency spectra obtained for the GBSM using the parameters from the Hussar 2011 data set. The overall form of the frequency spectra matches that of the data obtained in practice shown in Figure 7.9, however we could not match the dominant frequency and amplitude response of the theoretical and measured data.

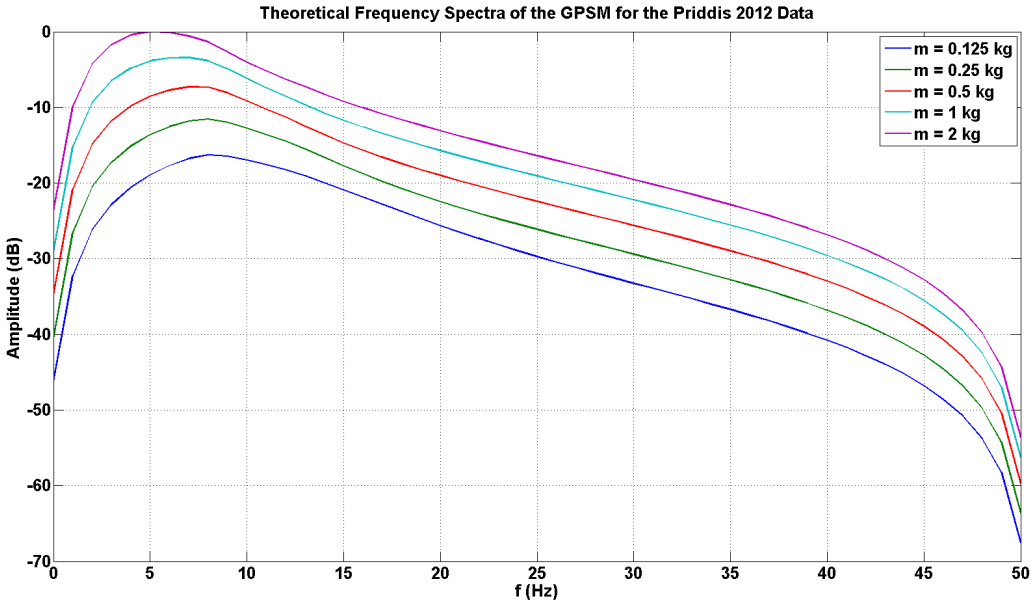

Figure 8.2: Theoretical frequency spectra obtained for the GBSM using the parameters from the Priddis 2012 data set. The overall form of the frequency spectra matches that of the data obtained in practice shown in Figure 7.10, however we could not match the amplitude response of the theoretical and measured data.

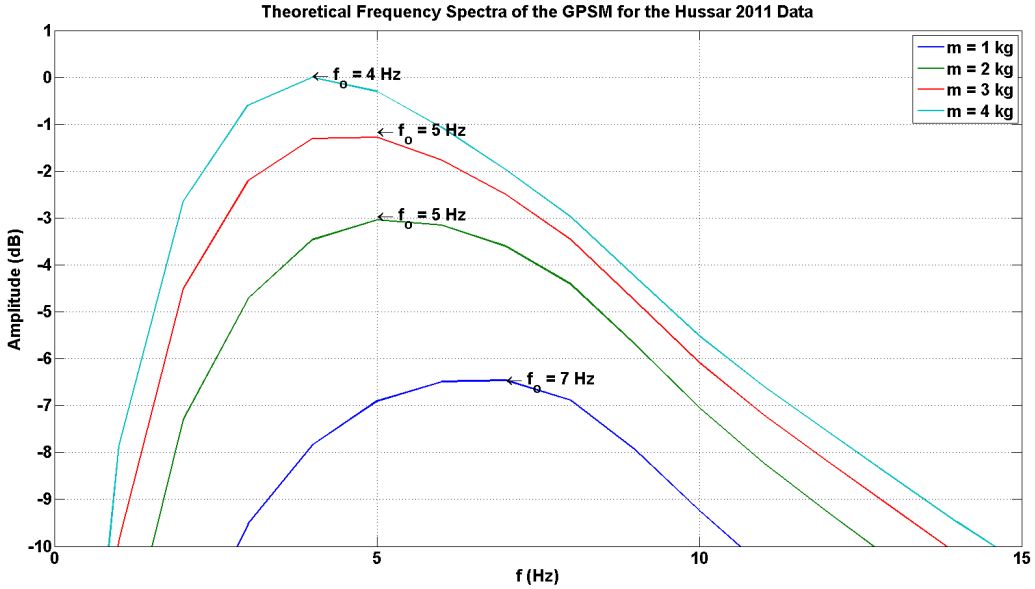

Figure 8.3: A closer view of the peaks of the frequency spectra obtained from the GBSM using the parameters of the Hussar 2011 data set. In this case we could not match the dominant frequency of the theoretical model with that of the experimental data shown in Figure 7.11.

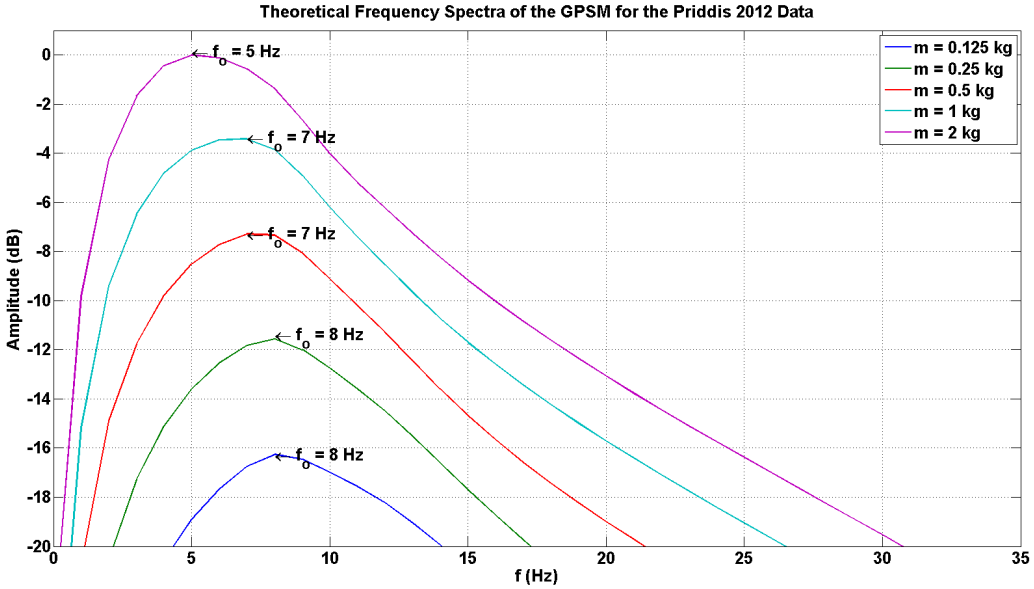

Figure 8.4: A closer view of the peaks of the frequency spectra obtained from the GBSM using the parameters of the Priddis 2012 data set. In this case we could not match the dominant frequency of the theoretical model with that of the experimental data shown in Figure 7.12.

Chapter 9

Application of the HCM to real data

One of the more significant features of the HCM is the variation of amplitude response with cavity orientation. Figure 4.10 shows that the theoretical power that is predicted by the HCM peaks at 90^o, which corresponds to a line that is directly along the radial component of the cylindrical cavity, which can be seen in Figure 4.1. Conversely, the power is at a minimum at both 0^o and 180^o, which corresponds to a line that is directly along the axial component of the cylindrical cavity. If we can observe this in a real data set, we may be able to characterize the radiation patterns that are emitted by dynamite in a borehole.

9.1 Rotating the Sensors

The Priddis 2013 experiment, which contains the data that we used for this analysis, is unique because we are using a series of sensors that are placed in a vertical observation well. Also note that some of the boreholes used for the test charges were drilled at an angle. One of the major strengths of the HCM, is the fact that it can predict the amplitude response across both the radial, and the transverse component of particle displacement (Blair, 2007). In order to observe the particle motion along each of these components, it would be useful to be able to mathematically rotate each of the sensors in our observation well such that they line up along either the radial or transverse component of particle motion.

Figure 9.1 shows the geometry of this experiment. The borehole is shown in blue, while the receivers that were in the well are shown in green. The distance from the axis of the borehole to the receiver line is given by d, and the distance from the center of the borehole to each receiver in the well is given by R. The variables z_s and x_s represent the depth and the x-position of the center of the borehole respectively, and z_r and x_r represent the depth and

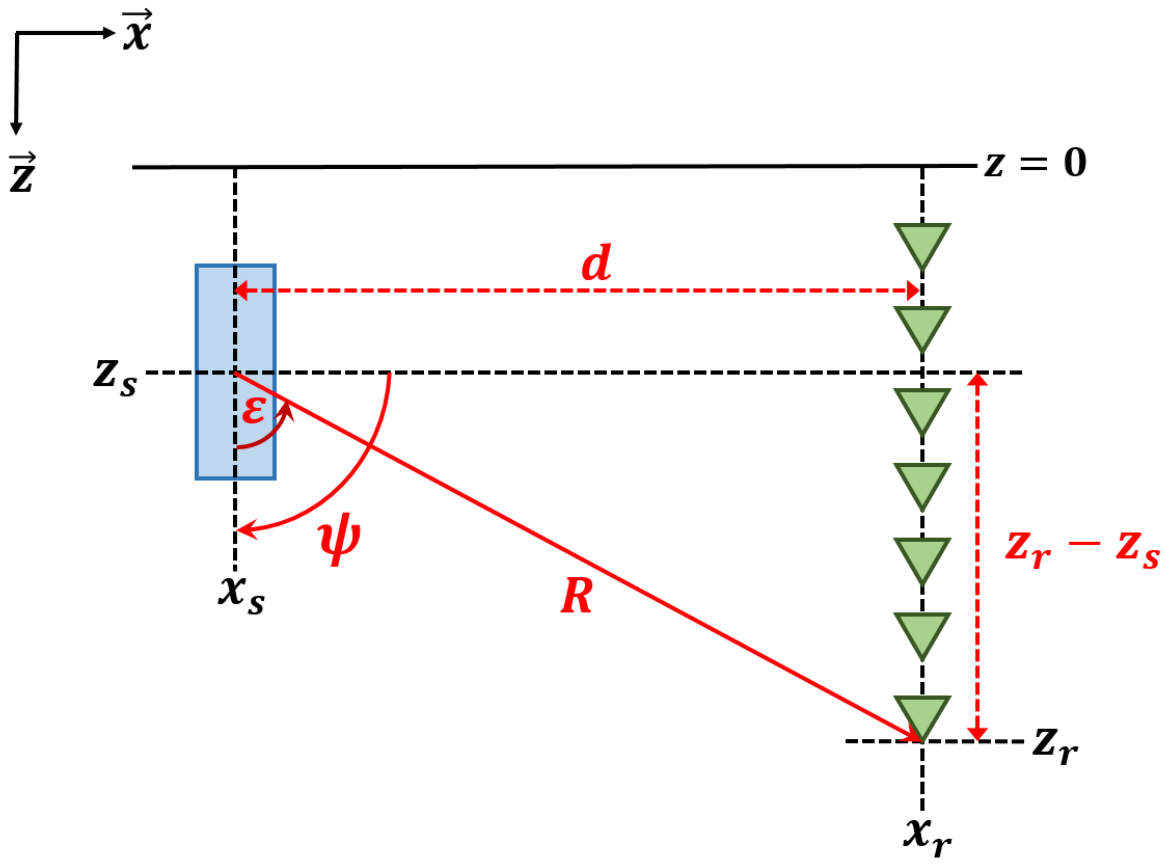

Figure 9.1: A graphical depiction of the HCM in the context of our field experiment. The borehole containing the source is shown in blue, and the receivers in the well are shown in green. The variables z_s and x_s are used to represent the depth and x-position of the center of the borehole respectively, and z_r and x_r are used to represent the x-position and depth of each receiver in the well respectively. The distance from the center of the source and the receiver line is given by d, and the distance from the center of the source to each receiver in the well is denoted by R. Note that in this particular figure the borehole is oriented vertically, but there were boreholes that were drilled at an angle in this experiment. The angle ε is the angle that the line connecting the center of the source to the receiver makes with the axial component of the borehole. The variable ψ is used to represent the angle that the axis of the borehole makes with the surface.

x-position of each receiver in the well. Note that x_r is assumed to be the same for all receivers in the well, as the well was drilled vertically. In this figure the borehole is assumed to be oriented vertically with respect to the source, but there were boreholes in this experiment that were drilled at an angle. For each sensor in the well, the line connecting the center of the source to sensor makes an angle ε with respect to the z-component passing through the source. The use of ε was implemented in order to avoid any confusion that might result when discussing borehole orientation measured in the field, and angles used in the HCM. In other words, when reporting angles measured from the field data we are referring to this angle ε (refer to Figure 9.1) to account for borehole orientation; when making references to the HCM itself, we use the angle ϕ (refer to Figure 4.1) which assumes that the cylindrical cavity is oriented vertically.

Figure 9.2 shows a top-down view of a columnar source (shown in red) emitting a series of waves (shown in purple) along the radial component of the cylinder. For future reference, the x-component will be referred to as the radial component, and the y-component will be referred to as the transverse component. In this scenario, we are looking downwards onto the top of a source. The axial component of the source aligns with the depth vector, and the depth component points directly into the page. The terms x_s and y_s correspond to the radial and transverse component of the sensor (shown in green) that is detecting the passage of elastic waves. When a line of sensors is deployed in a well it is very likely that they will rotate on the way down, such that the radial and transverse component of the sensor do not line up with the radial and transverse component of the emitted waves. Note that the the vector $\vec{p}$ in this figure represents the particle displacement that results from the emission of the elastic waves from the source.

In order to fully investigate the effect of the source orientation on the measured amplitude spectra, it would be beneficial to rotate the sensors such that either the radial or transverse component of the geophone is aligned in the direction of maximum particle displacement.

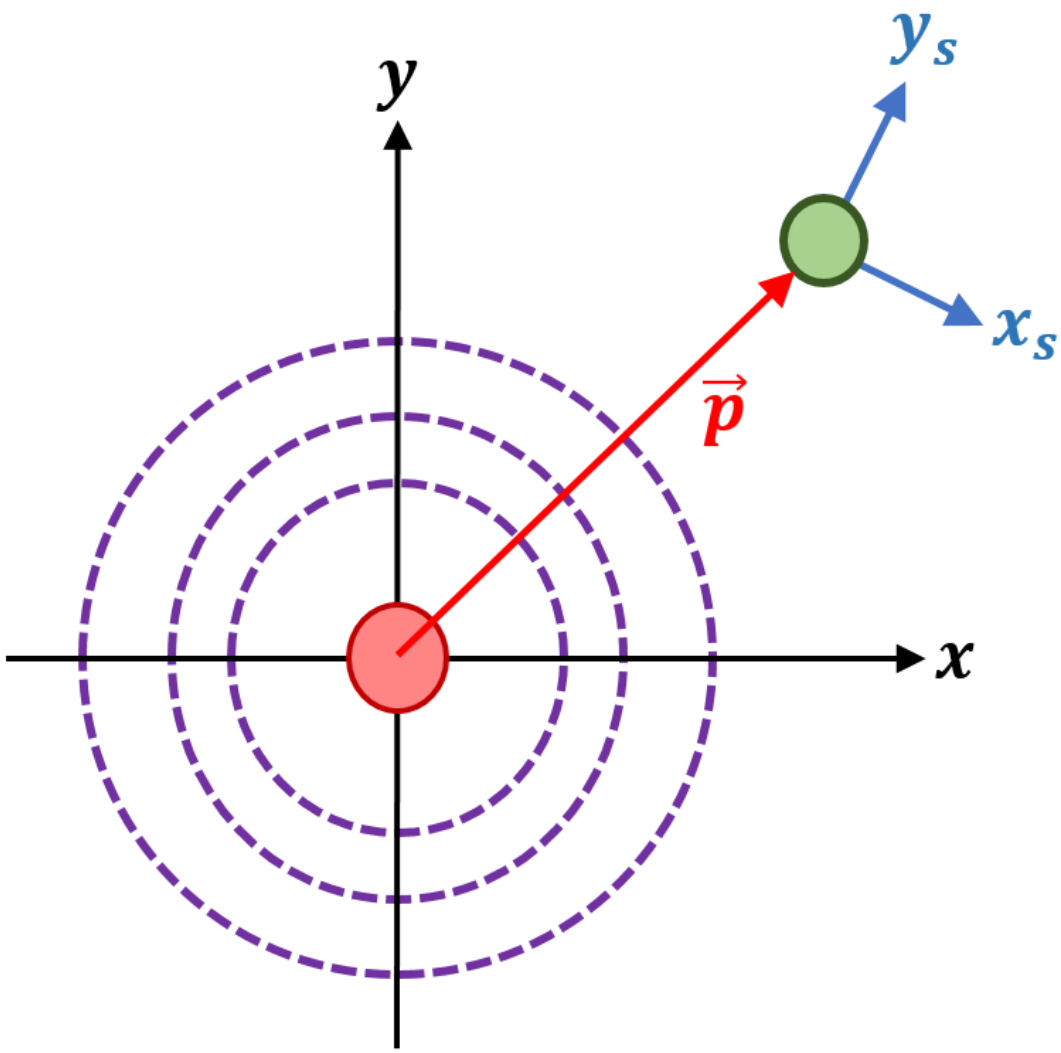

Figure 9.2: Top-down view of a columnar source emitting a series of waves, that are in turn detected by a sensor. The source is shown in red, the emitted waves are shown in purple, and the sensor is shown in green. The vector $\vec{p}$ corresponds to the particle displacement that results from the propagation of the emitted waves.

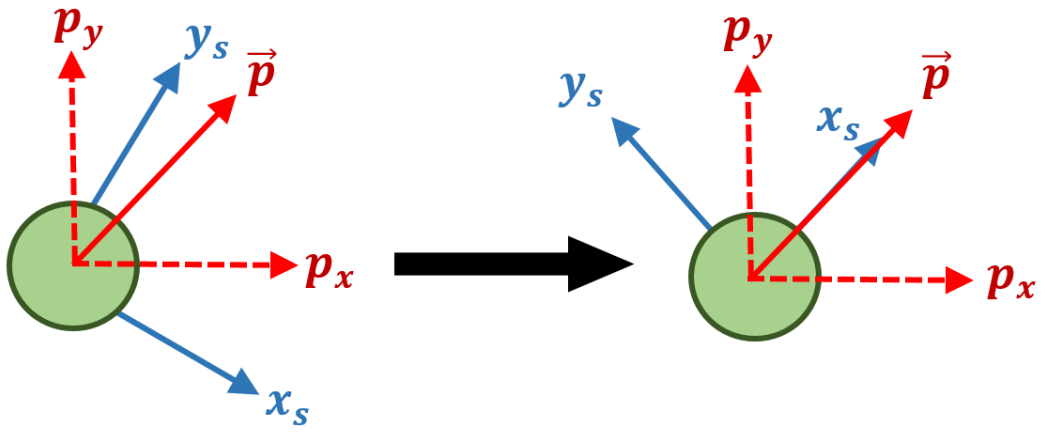

Figure 9.3: A graphical depiction of the ideal rotation to be performed in order to maximize the energy along the radial component of the geophone.

This ideal rotation to produce the maximum energy along the radial component of the geophone has been shown in Figure 9.3. The rotation matrix in two dimensions is given by

$$R = \begin{bmatrix} \cos\theta & -\sin\theta \\ \sin\theta & \cos\theta \end{bmatrix}, \tag{9.1}$$

where θ is the rotation angle, and R is the rotation matrix. By applying the rotation matrix to the acquired radial and transverse data, we can rotate both components of the geophone by an amount θ. If we let x_s and y_s represent the initial radial and transverse data obtained in practice, the rotated radial and transverse components can be obtained via the following equation:

$$\begin{bmatrix} x_s{}' \\ y_s{}' \end{bmatrix} = \begin{bmatrix} \cos\theta & -\sin\theta \\ \sin\theta & \cos\theta \end{bmatrix} \begin{bmatrix} x_s \\ y_s \end{bmatrix}, \tag{9.2}$$

where $x_s{}'$ and $y_s{}'$ are the rotated radial and transverse components of the sensors respectively.

In order to properly align the desired sensor component with the maximum particle displacement, we need to determine the rotation angle θ that will produce the maximum

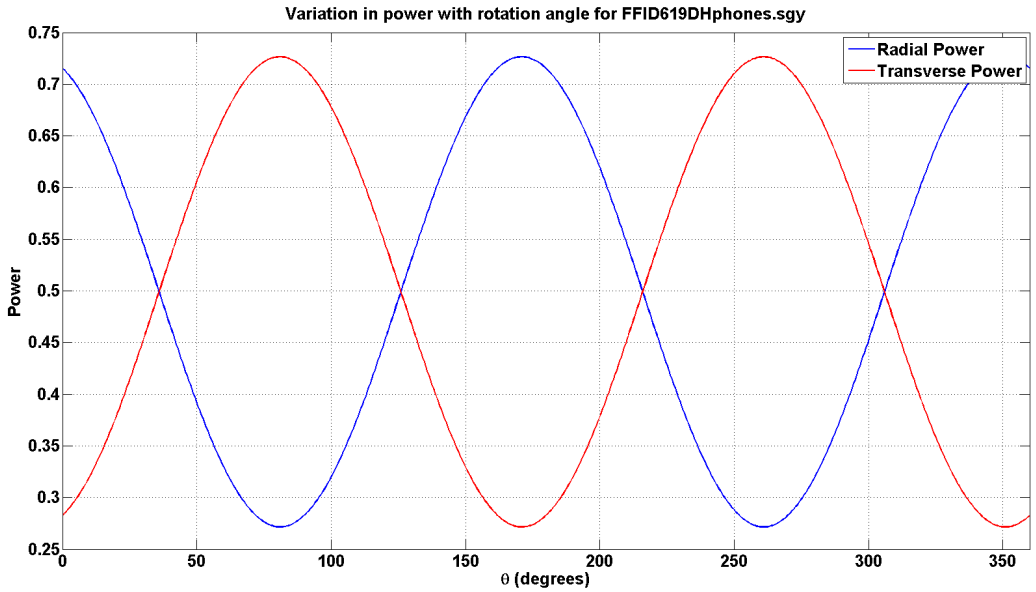

Figure 9.4: An example plot of the rotated shot power as a function of the rotation angle for both the radial and transverse component. The maximum amplitudes of the radial and transverse component appear to be 90^o out of phase.

energy along that component. The maximum energy from the source should occur along the p-vector that is shown in Figure 9.2, so ideally we would like to rotate one of the components along this vector. We started by selecting a single shot record and carrying out a series of rotations on a single trace using Equation 9.2 for θ values between 0 and 360^o. For each individual rotation we computed the shot power for the obtained $x_s{}'$ and $y_s{}'$ rotated data, and plotted it against the corresponding angle. The results of this operation can be seen in Figure 9.4. This plot shows a distinct variation in the shot power for both the radial and transverse component with rotation angle. Note that there appears to be a 90^o phase difference between the peaks of these plots, which should be expected as there is a 90^o angle between the transverse and radial component. Also note that these energy patterns are 2π periodic, as they begin to repeat themselves after 180^o.

Using the information that we obtained in our previous calculation, we computed the rotation angles that would produce the maximum transverse and radial energy for the sensors. Figure 9.5 shows a plot of the rotation angles that produce the maximum transverse and

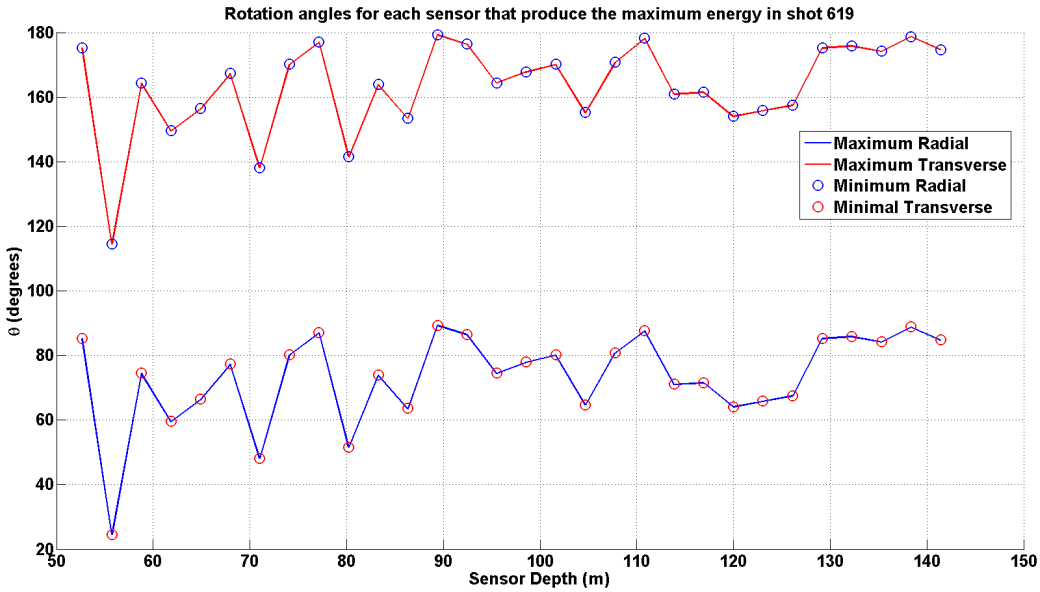

Figure 9.5: A plot of the maximum and minimal radial and transverse energy as a function of the rotation angle. Note that in this case the maximum amplitudes of both the radial and the transverse component are 90^o out of phase, which matches our observation in Figure 9.4.

radial energy for each sensor in a selected shot record. The angles associated with both the radial and transverse energy show some variance with each sensor, which should be expected as each sensor will most likely rotate differently as they are placed in a well. Additionally, the maximum and minimum radial and transverse energy patterns are 90^o out of phase at every angle, which matches our observation from Figure 9.4.

Upon obtaining the initial rotation angles shown in Figure 9.4, we rotated the data set by applying Equation 9.2 to each individual sensor using the angles that produced the maximum transverse and radial energy. Figures 9.10 and 9.11 shows the initial radial and transverse energy of shot 619 before rotation. In this case the sesnors appear to be oriented in such a way that the transverse energy is higher than that of the radial energy. Figures 9.12 and 9.13 shows the radial and transverse energy after the data was rotated to produce the maximum radial energy. Note that for these two figures, we used the angles that lie along the blue line in Figure 9.5 for the rotation angle θ. Conversely, Figures 9.14 and 9.15 shows the radial and transverse energy after the data was rotated to produce the maximum transverse energy.

For this set of figures, we used the angles that lie along the red line in Figure 9.5.

Observation of Figures 9.10 through 9.15 reveals a distinct change in the energy patterns when a rotation is applied to each sensor. Note that all of these figures are from the same gather of plots, and share the same clip level. Comparison of Figures 9.10 and 9.12 shows a distinct increase in the radial energy when the sensors are rotated to produce maximum radial energy. Using the same rotation angles produces minimal energy along the transverse component, which can be seen in Figure 9.13. This is a significant decrease from the initial transverse energy which is shown in Figure 9.11. These observations are consistent with our predictions of the maximum amplitude variation with rotation angle shown in Figure 9.5. Rotating the records to produce the maximum transverse energy produces the same effect in the transverse energy, which can be seen in Figures 9.11 and 9.15.

9.2 Energy at the Top of the Well

Throughout the course of our analysis, we noted that at the top of the well there was a great deal of energy that did not appear to be affected by the rotation of the sensors. Currently, we do not understand what is causing this phenomenon, the only thing that we know for certain is the fact that it does not seem to be affected by rotation of the sensors. Up until this point, we have only considered the first thirty sensors in the well, as they do not seem to be affected by this energy pattern. Figure 9.6 shows rotation angles that correspond to maximum radial and transverse energy for all the sensors in the well for shot 619. Previously, we had observed that the maximum radial and transverse energies should be 90^o out of phase (Figure 9.4) which does not appear to be occurring in this set of sensor rotations. Figures 9.16 and 9.17 shows the rotated data for shot 619 that was carried out using all the sensors, and the angles shown in Figure 9.6. Observation of these figures shows that the energy at the top of the well is never completely minimized regardless of rotation angle. This suggests that some of the energy at the top of the well is different than that of the energy near the

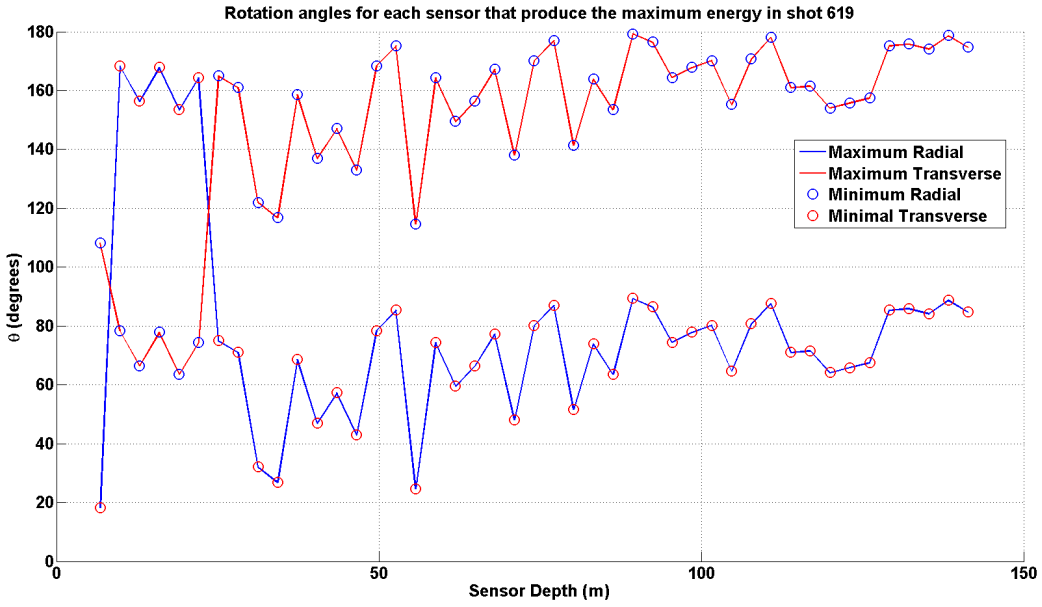

Figure 9.6: A plot of the maximum maximum shot power as a function of rotation angle for shot 619. As we approach the top of the well, the radiation patterns do not appear to resemble that of Figure 9.4, which predicts that the maximum radial and transverse energy should be 90^o out of phase. This observation may indicate that we cannot use the HCM to model this energy.

bottom, and thus we may not be able to use the HCM to characterize the nature of this radiation. Therefore, we must be cautious about any conclusions that we draw regarding the HCM until this energy pattern at the top of the well is better understood.

9.3 Extracting the Radiation Pattern

After rotating the shot records we examined the radiation pattern at each sensor, which is dependent on the angle ε as shown in Figure 9.1. This was accomplished by computing the shot power for each sensor, and then determining the angle ε of the corresponding sensor from the geometry of the experiment. Note that for this calculation, we used all of the sensors in the well, and we applied a gain correction to account for loss of amplitude due to spherical divergence. For the first vertical borehole, which was shot 619 that we have been using for all the figures at this point, the extracted radiation pattern can be seen in Figure 9.18. This figure also contains the two polar plots that predict amplitude variation with angle ϕ in the HCM. For this shot the borehole was drilled vertically downwards, and so the measured angle ε is equal to that of ϕ in the polar plots. The polar plots predict that the maximum amplitude in this configuration should be at approximately 90^o, which appears to have occurred here.

9.4 Radiation Variation with Borehole Orientation

In addition to shot 619 in this study there were two other shots, 621 and 622, which were both drilled at an angle of approximately 30^o either towards or away from the well. Each of these shots were the same size, and were drilled to approximately the same depth of 15 m. Shot 621 was drilled away from the well at an angle of approximately 30^o with respect to the surface, such that the radial component of the cylinder shown in Figures 4.1 points towards the surface. Conversely, shot 622 was drilled towards the well at an angle of approximately 30^o with respect to the surface, such that the radial component of the cylindrical cavity

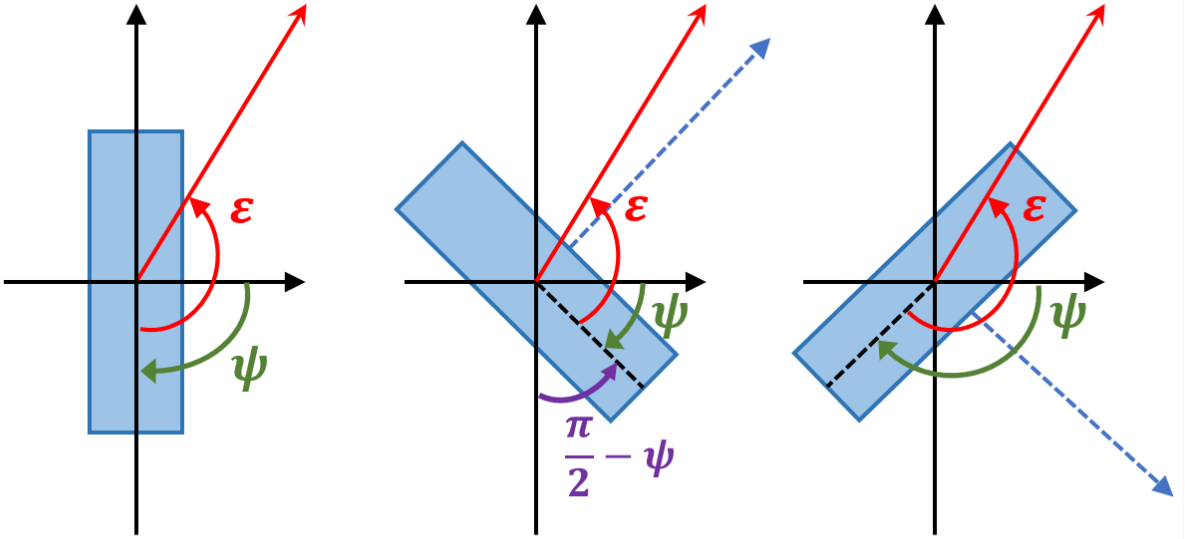

Figure 9.7: Graphical depiction of the rotation of the cylindrical cavity. The rotation of the cavity, and therefore the borehole, should redirect some of the energy from the shot if the predictions of the HCM are to hold true for real data, as the HCM predicts that the largest portion of the emitted energy should occur along the axial component of the cylinder.

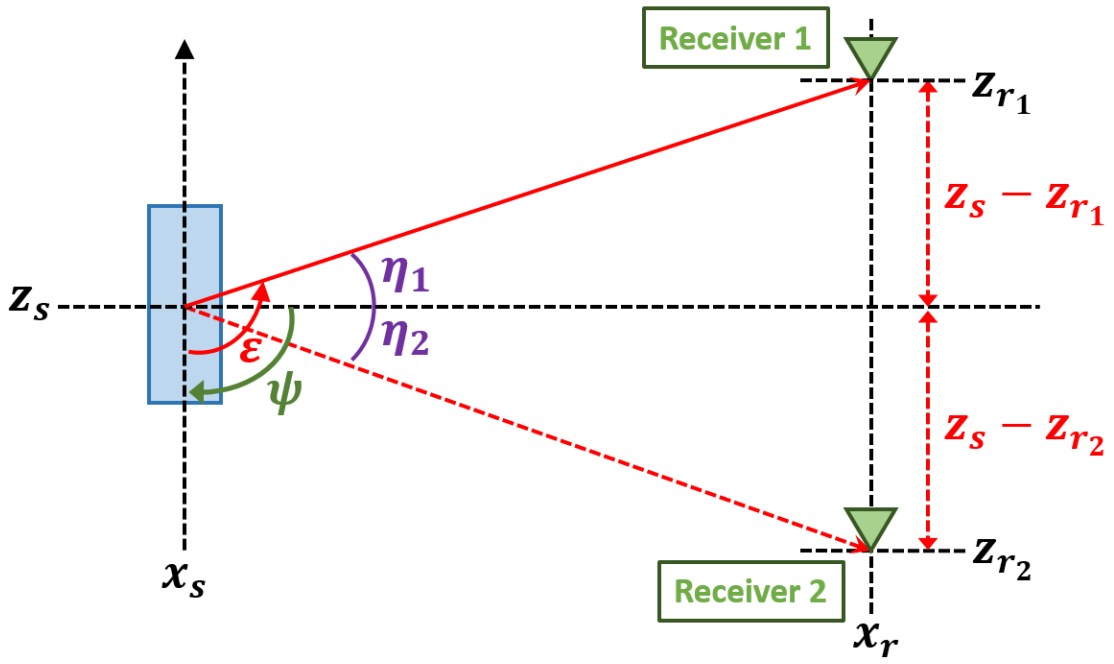

Figure 9.8: Graphical depiction of the geometry used to determine the angle ε. Similar to the other figures, the source is shown in blue, while the receivers are shown in green. For a given receiver, the angle η is first calculated using the variables d, z_s, and z_r. After η is obtained, it is added to the value of ψ, which gives ε. Addition works because in the event that a receiver is above the borehole (such as receiver 1 in this case), $z_s - z_{r1}$ will be positive, and thus η is positive. In that scenario, ε is ψ plus η. Alternatively, if the receiver is below the borehole (such as receiver 2 in this case), $z_s - z_{r2}$ will be negative. In that scenario, ε is ψ minus η. Therefore, due to the geometry, the correct value for ε can always be found if ψ is added to η.

points towards the lower portion of the well. Rotation of the cylindrical cavity in the HCM and the direction of the radial component has been depicted in Figure 9.7, where the dotted blue arrow shows the direction of the radial component of the cavity. From the theory of the HCM, we expect that a large portion of the shot energy should be directed along the radial component of the cavity (Figure 4.10), and thus the orientation of the borehole should affect the radiation patterns measured by the sensors in the well.

Calculation of the angle ε requires an understanding of the orientation of the sensors with respect to the boreholes. Figure 9.8 shows the geometry involved with the boreholes and the sensors in the well. To calculate ε for a particular sensor, the value of η must first be calculated using the distance from the source to the receiver, and the depths of the source and receiver. This is accomplished using the tangent relationship, such that

$$\eta = \arctan\left(\frac{z_s - z_r}{d}\right), \tag{9.3}$$

where z_s is the depth of the source, z_r is the depth of the receiver, and d is the distance from the source to receiver as seen in Figure 9.8. Upon obtaining η, ε can be calculated by adding η to the ψ angle. Recall that ψ is the orientation of the borehole with respect to the surface. Therefore, ε can be calculated using the equation

$$\varepsilon = \psi + \eta. \tag{9.4}$$

Combining this equation with Equation 9.3 yields

$$\varepsilon = \psi + \arctan\left(\frac{z_s - z_r}{d}\right), \tag{9.5}$$

which was used to calculate the reported ε values obtained in this experiment. Equation 9.5 should always be valid for calculating the value of ε regardless of the location of the receiver with respect to the borehole. Referring once again to Figure 9.8, if the receiver is located above the source like receiver 1 is in this figure, the value of $z_s - z_{r1}$ will be positive, and thus η will be positive based on Equation 9.3. In that scenario, based on the geometry of

the problem, ε is the sum of ψ and η. Alternatively, if the receiver is located below the source like receiver 2 is in this figure, the value of $z_s - z_{r2}$ will be negative, and thus η will be negative based on Equation 9.3. In that scenario, ε is the difference between ψ and η.

Figures 9.19 through 9.20 shows the individual radiation patterns that were extracted from shots 619, 621, and 622 respectively. Figure 9.22 shows each of these figures plotted together on the same scale, where each power spectra has been normalized to the total power of each individual shot. Observation of this figure shows that the shot that was drilled away from the observation well produced the largest amounts of energy, and the shot that was drilled towards the borehole produced the smallest amount of energy. There are several key features of this plot that are important to the HCM. The first and foremost is the fact that the orientation of the borehole appears to affect the resulting radiation pattern, which is one of the key aspects of the HCM. The second is the fact that when the radial component of the borehole points towards the surface of the well, which is the case for the borehole that was drilled away from the well, the radiation near the top of the well is much higher than when the radial component is pointed towards the lower portion of the well, which is the case for the borehole that has been drilled towards the well. The power from the shot that has been drilled vertically appears to be less than that of the shot drilled away from the well, but more than that of the shot that has been drilled towards the well. The HCM states that the majority of the emitted energy occurs along the radial component of the cylindrical cavity, and the variation radiation patterns with the borehole orientation that we observe here coincides with that prediction.

A key feature of the HCM is the variation in amplitude with source orientation. We observed significant variation in the amplitudes depending on the orientation of the source, which suggests that this aspect of the HCM can be used in practice. Aldridge offers some theoretical groundwork for describing the wave fields that are produced by a line source, which may be of use when attempting to describe the waves that result from angled boreholes.

Figure 9.9 shows the amplitude of the particle displacement that result for varying angles of ϕ, that was taken directly from Aldridge's publication (Aldridge, 1998). From this figure we can see that the maximum amplitude displacement occurs along the $\phi = 90^o$ line, and when we change the orientation of the borehole we are effectively rotating this plot. In the scenario where the borehole is drilled away from the well, we are shifting this plot in a counter-clockwise direction, which points the higher amplitude components towards the top of the well. When the borehole is drilled towards the well, we are rotating this plot clockwise, and so the higher amplitude components are moved away from the top of the well and moved closer to the bottom. This could potentially explain the amplitude variations that we observed in our applications of the HCM.

9.5 Frequency Spectra and Borehole Orientation

To observe how the orientation of the borehole affected the frequency spectra in the HCM we examined the data from three separate sensors from each shot record. We looked at one sensor near the bottom of the observation well, one sensor in the middle of the well, and one sensor at the top of the well for shots 619, 621, and 622. Figures 9.23 through 9.25 shows the frequency spectra obtained from these sensors for all three shot records. There does not appear to be a significant variation in the frequency spectra for each sensor. In order to see if there is any sort of pattern to these variations, we compared the data from each sensor location between all three shot records. Figure 9.26 shows the the frequency spectra for the bottom sensor in the well for all three shot records, which are all plotted on the same decibel scale. Figures 9.27 and 9.28 shows spectra for the middle and top sensors for the three separate shot records as well. Note that each of these frequency plots is plotted on its own individual decibel scale.

For all three sensors, the low frequency content of the spectra does not appear to have any sort of discernible pattern, which makes it difficult to draw any sort of conclusions about

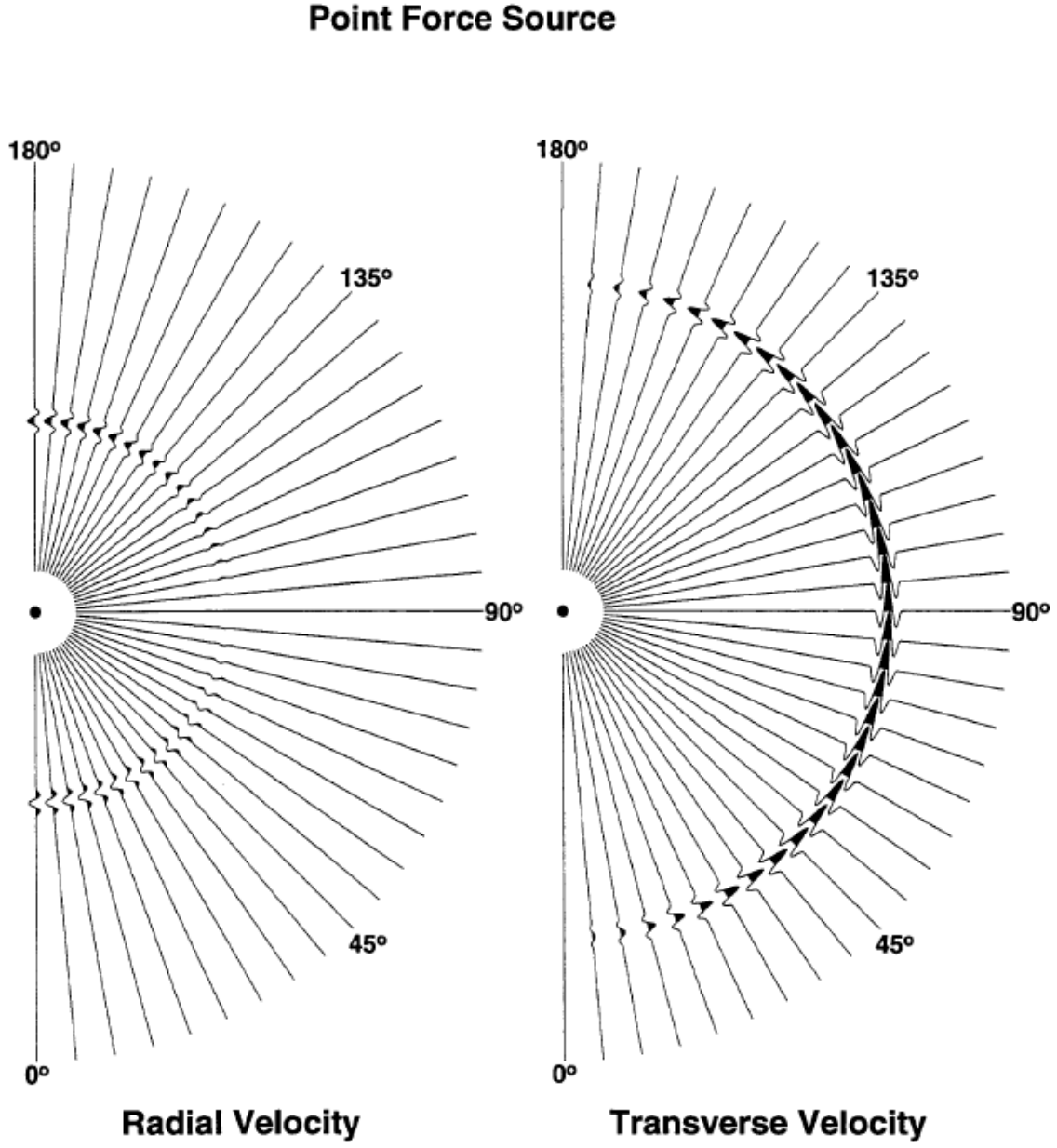

Figure 4

Figure 9.9: Figure of the Point Force Source taken directly from an Aldridge publication (Aldridge, 1998). This figure shows the variation in amplitudes with ϕ for both the transverse and radial energy.

the effect of the borehole orientation on the frequency spectra. For the bottom sensor all three spectra are similar across all frequencies, and there does not appear to be any sort of significant variations in the frequency spectra. However, for the top and middle sensors, there does appear to be a similar pattern in the higher frequencies of the spectra. The shot that was drilled towards the well seems to have produced more high frequency content than that of the other two orientations. In the theoretical modeling of the HCM, we did not notice any sort of distinct variation in the frequency spectra as we varied the ϕ angle, so it might not be possible to attribute this frequency pattern to anything we have observed in the HCM.

Blair explored a numerical model for a line charge and compares it to that of the solutions of the HCM (Blair, 2007). His work within this publication showed that the Heelan far-field approximation is not in essence a "true" far-field approximation because it places restrictions on the frequency content of the source. Blair also states that for very high source frequencies, the Heelan approximation significantly overstates the the true solution regardless of the distance from the source to receiver. Conversely, if the source frequencies are too low, the Heelan solution produces large fluctuations about the true solution. Therefore, we may not be able to rely on the HCM to make frequency predictions regarding shots in angled boreholes.

9.6 Limitations and Experimental Uncertainties

One of the biggest issues that may be present in this study regarding the HCM is the energy that is present near the top of the well in each of the shots we have investigated. The computed angles that produced the maximum and minimum radial and transverse energy patterns did not appear to follow the phase behavior that was present in the bottom portion of the well. This energy may not be as dependent on the rotation of the geophones as the energy in the bottom portion of the well. We must therefore be cautious about drawing any

sort of conclusions about the amplitude variation with borehole orientation, as the energy near the top of the well may not be something that we can account for with this particular theory.

The frequency spectra that we observed do not display any sort of discernible patterns besides the amplitude differences in the higher frequency content of the top and middle sensors. We currently don't have anyway of investigating this phenomenon, as the HCM as we've used it does not seem to produce any sort of variation in the frequency spectra with when the angle ϕ is altered. Additionally, the notching in this spectra is very severe, and it is entirely possible that that dominant frequency in each case has been buried by one of the notches, making it difficult for us to identity the dominant frequency of the waves in this part of the experiment.

We are also dealing with a very limited data set, as we only had a few holes from this experiment that were drilled in a direction that was not vertical. In order to investigate the claims of the HCM in a more reliable manner, we may need to collect more data in the future to see if our observations from this data set occur at other locations as well.

9.7 Chapter Summary and Conclusions

- Our method for rotating the sensors appears to be able to produce the maximum radial and transverse energy patterns.
- The amplitude content of the waves emitted by an explosive source is affected by the orientation of the borehole.
- We could not observe any significant frequency variation in the emitted waves with varying borehole orientation.
- The HCM can potentially make predictions about the amplitude content of waves emitted by the source.

- Further research is required before we can draw any reliable conclusions regarding the HCM's ability to predict the frequency content of waves emitted by sources in an angled borehole.

- There is energy present in the top of the well that does not share the same behavior of amplitude variation with rotation angle as that of the other sensors. This suggests that this energy may not be affected by the rotation of the sensors, and thus we may not be able to reliable characterize it using the HCM.

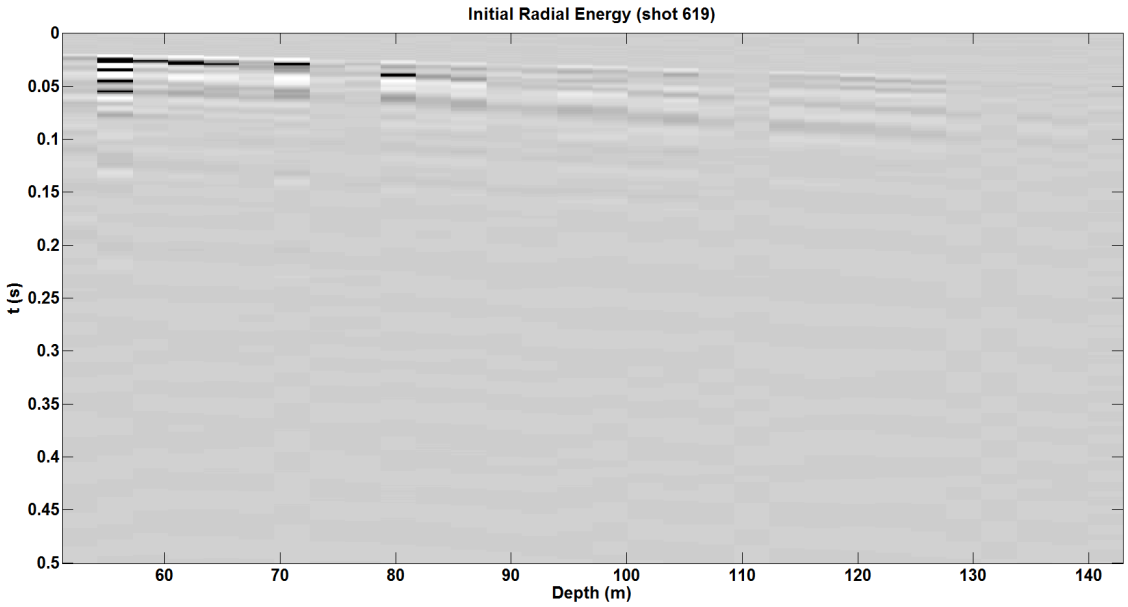

Figure 9.10: Plot of the initial radial energy for shot 619 from the Priddis 2013 data set.

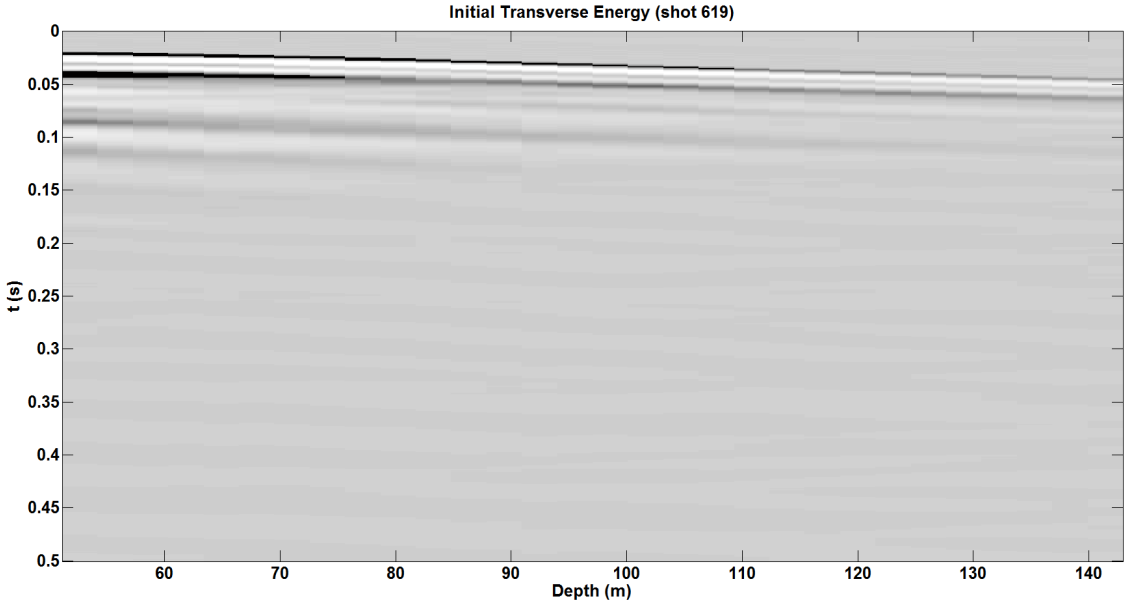

Figure 9.11: Plot of the initial transverse energy for shot 619 from the Priddis 2013 data set.

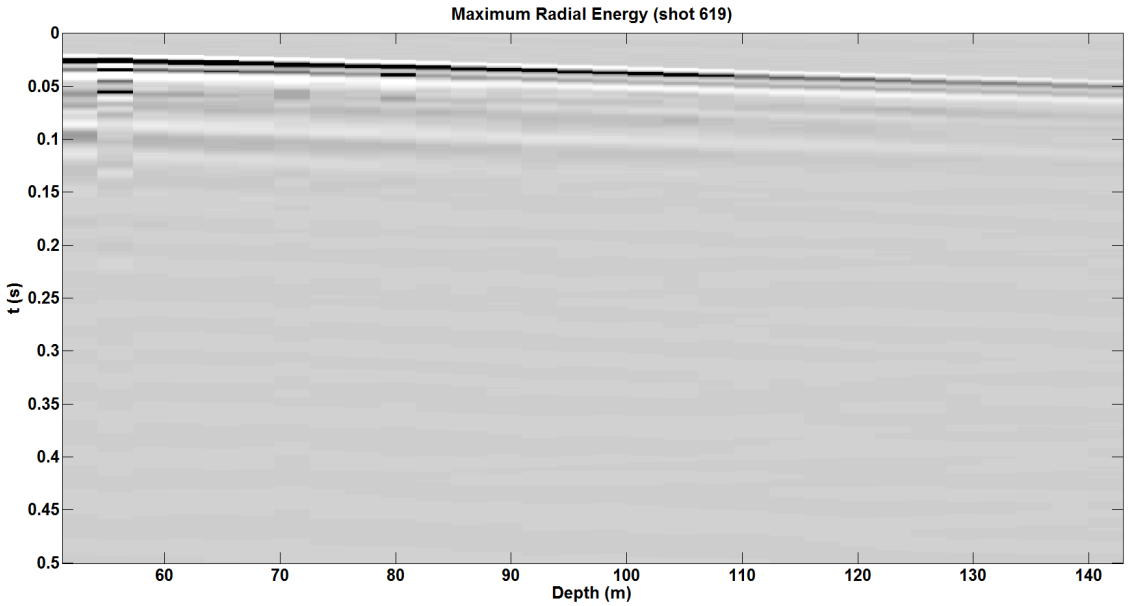

Figure 9.12: Plot of the maximized radial energy for shot 619 in the Priddis 2013 data set.

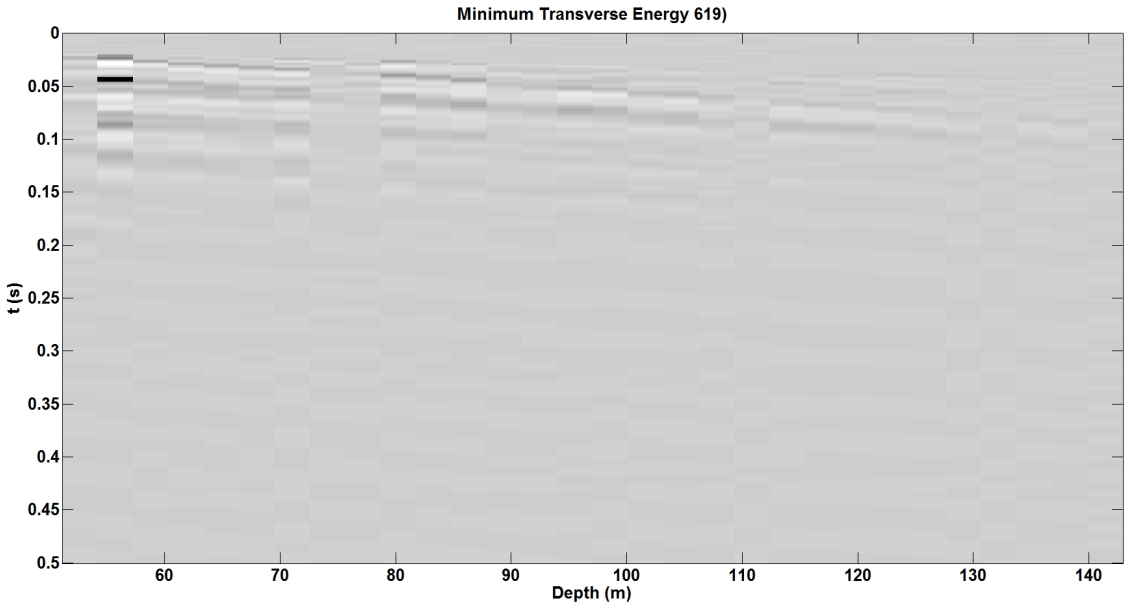

Figure 9.13: Plot of the minimized transverse energy for shot 619 in the Priddis 2013 data set.

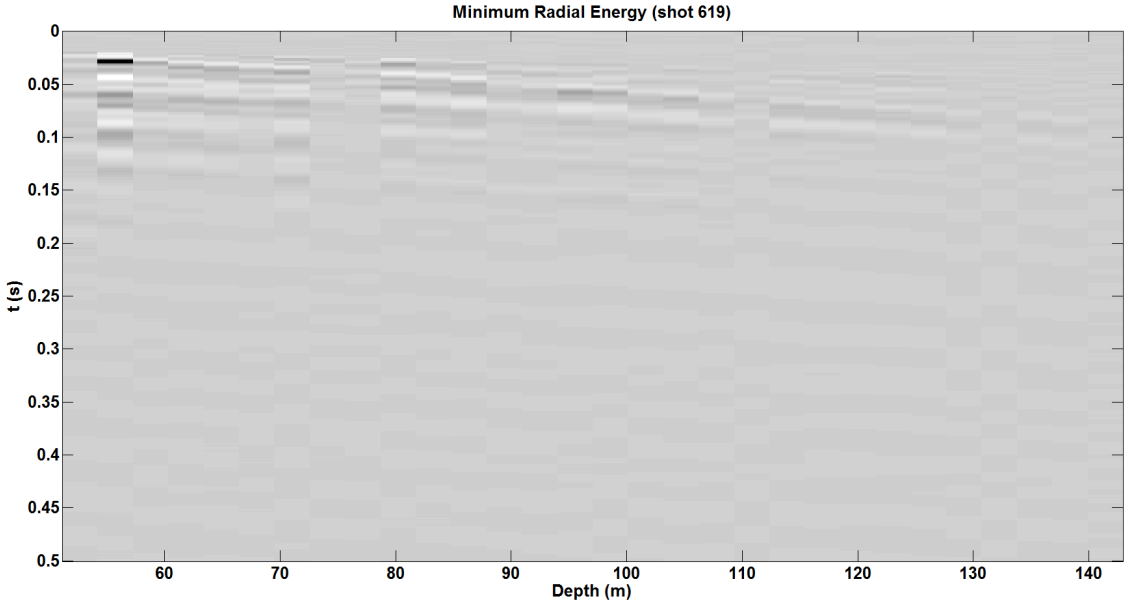

Figure 9.14: Plot of the minimized radial energy for shot 619 in the Priddis 2013 data set.

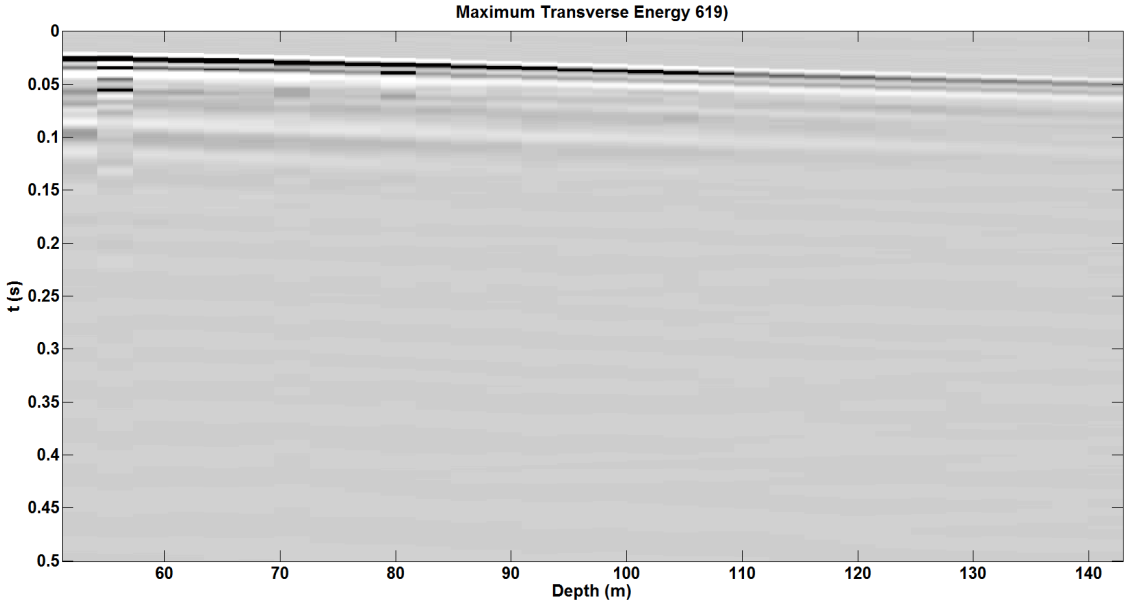

Figure 9.15: Plot of the maximized transverse energy for shot 619 in the Priddis 2013 data set.

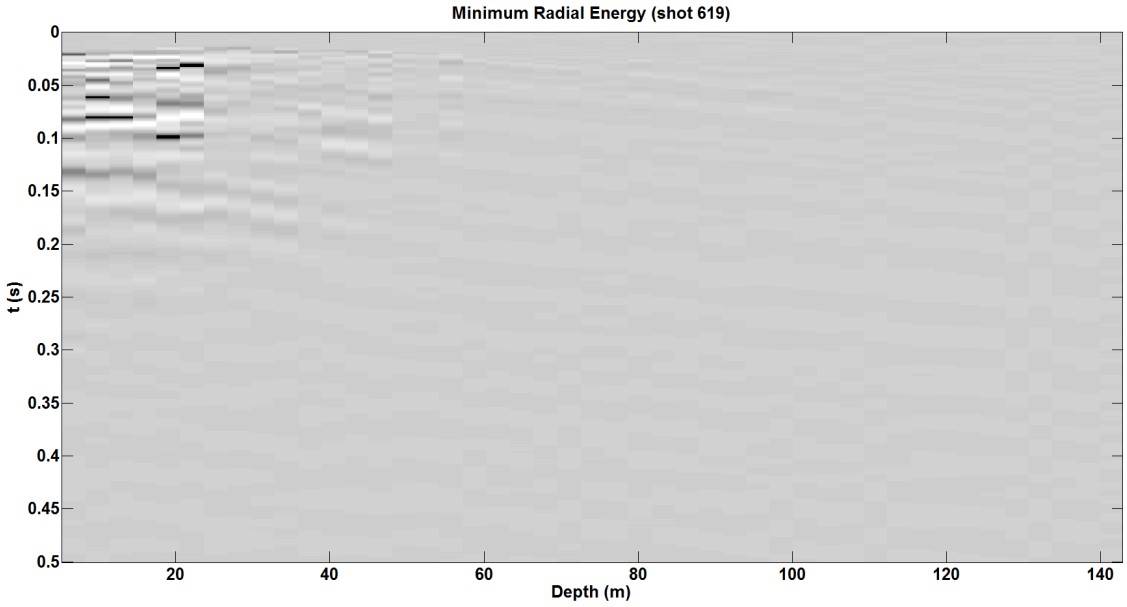

Figure 9.16: Rotated shot record for all sensors in shot 619. This sensors were rotated to produce the minimum radial energy, which does occur for the lower sensors. However, the energy at the top of the well do not seem to be affected by this rotation.

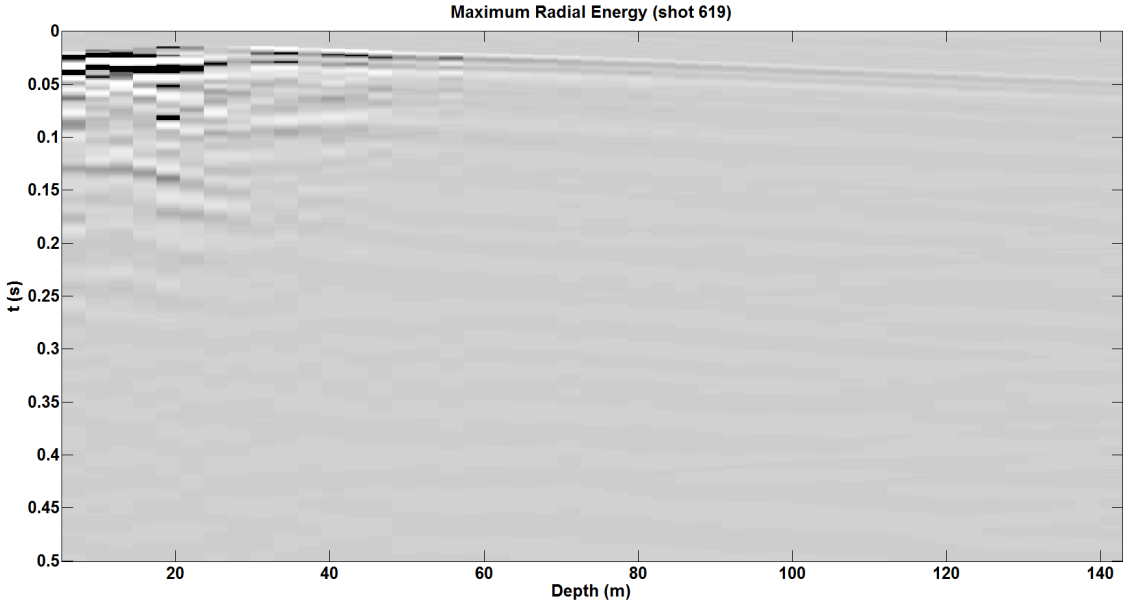

Figure 9.17: Rotated shot record for all sensors in shot 619. This sensors were rotated to produce the maximum radial energy. The energy at the top of the well do not seem to be affected by this rotation.

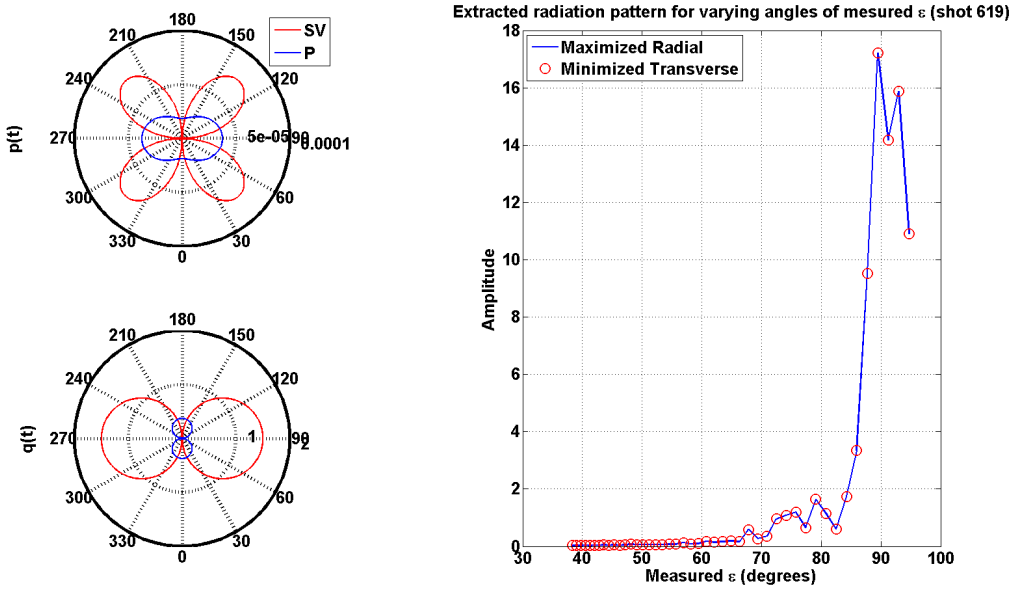

Figure 9.18: Extracted radiation pattern for Shot 619 along with the Heelan polar plots showing amplitude variation with angle ϕ in the HCM. In this particular figure the borehole is drilled vertically, so the angle ϕ in the polar plot is equal to the measured angle ε in Figure 9.1. Note that the maximum energy seems to occur along $\phi = 90^o$.

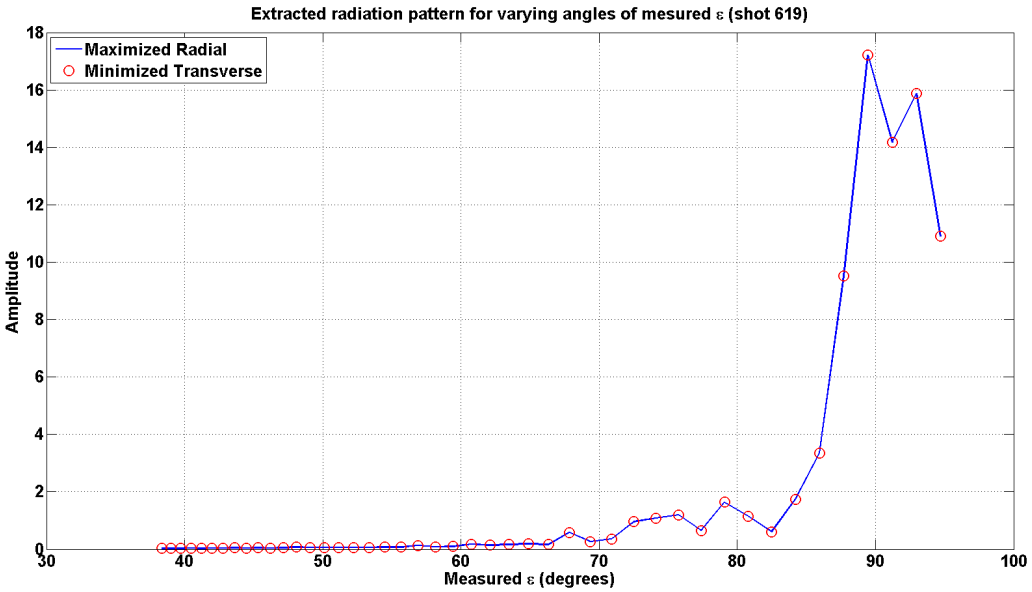

Figure 9.19: The extracted radiation pattern from shot 619 as a function of the angle ε. The borehole for this shot was drilled vertically downwards.

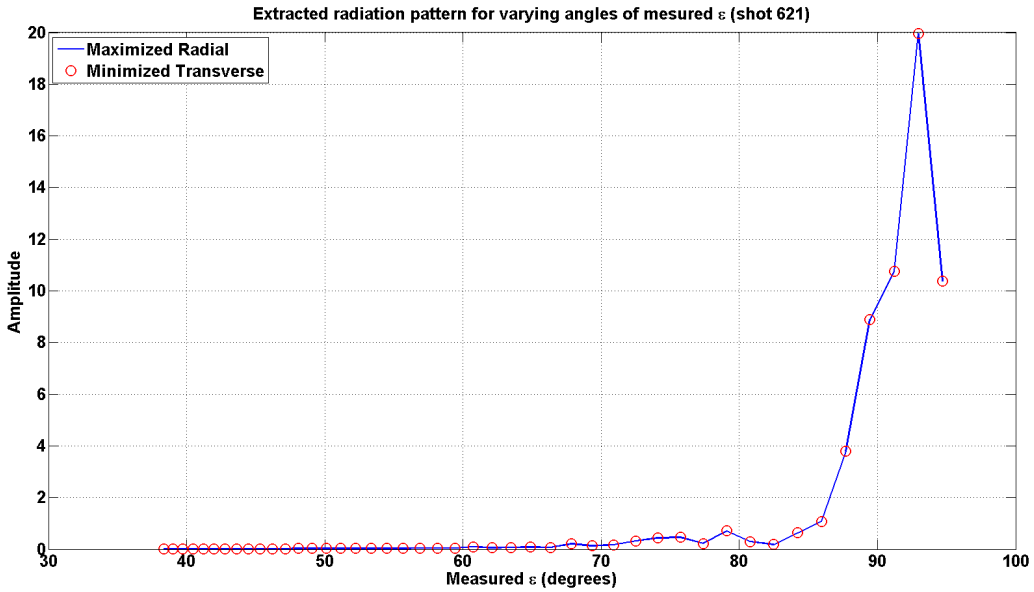

Figure 9.20: The extracted radiation pattern from shot 621 as a function of the angle ε. The borehole for this shot was drilled away from the well at an angle of approximately 30^o with respect to the surface.

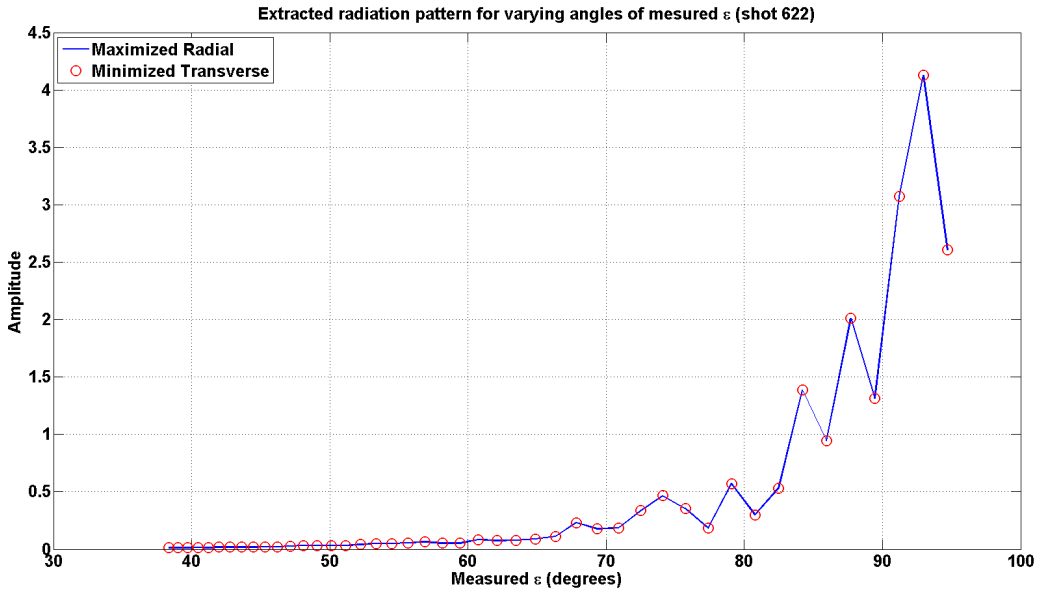

Figure 9.21: The extracted radiation pattern from shot 622 as a function of the angle ε. The borehole for this shot was drilled towards the well at an angle of approximately 30^o with respect to the surface.

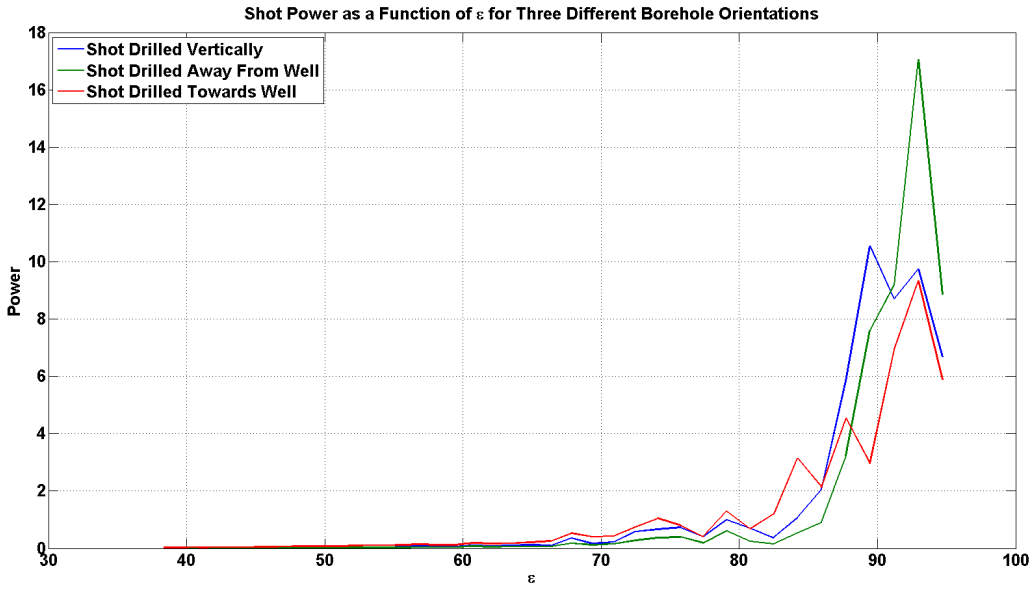

Figure 9.22: A plot of the extracted radiation patterns for all three shot records, where each spectra has been divided by the total power of their corresponding shot. The shot that was drilled away from the well appears to produce the largest amplitude, and the shot that was drilled towards the well appears to produce the smallest amplitude.

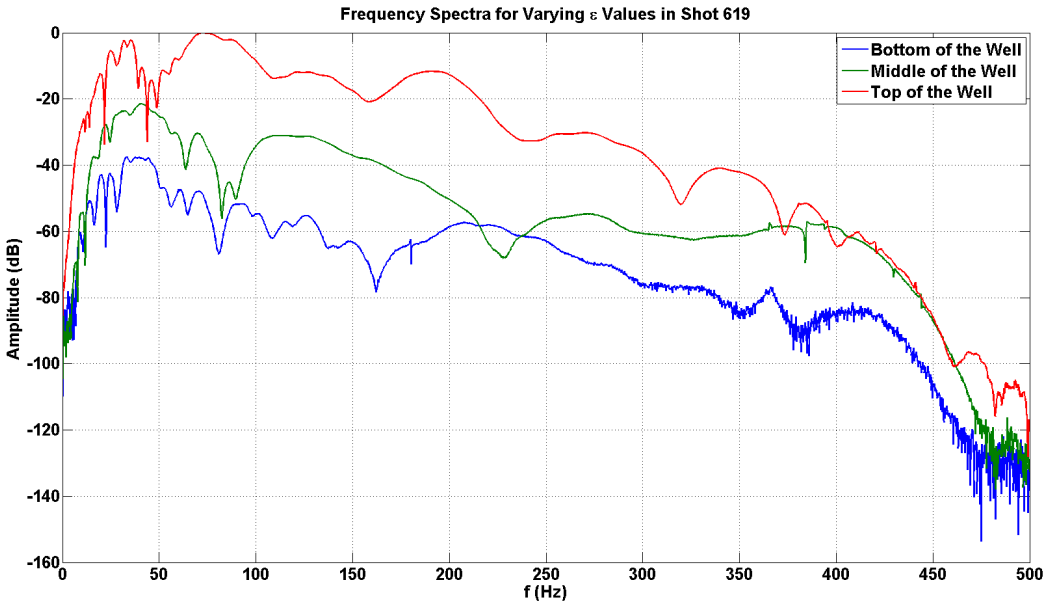

Figure 9.23: Frequency spectra three sensors in shot 619. One sensor is at the bottom of the well, one sensor is near the middle of the well, and one sensor is at the top of the well.

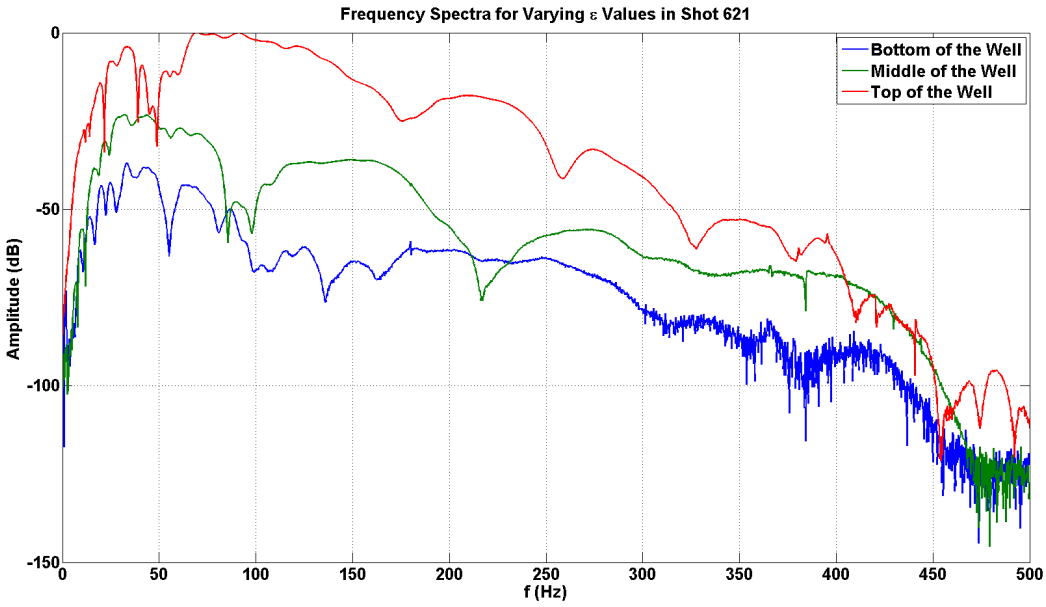

Figure 9.24: Frequency spectra three sensors in shot 621. One sensor is at the bottom of the well, one sensor is near the middle of the well, and one sensor is at the top of the well.

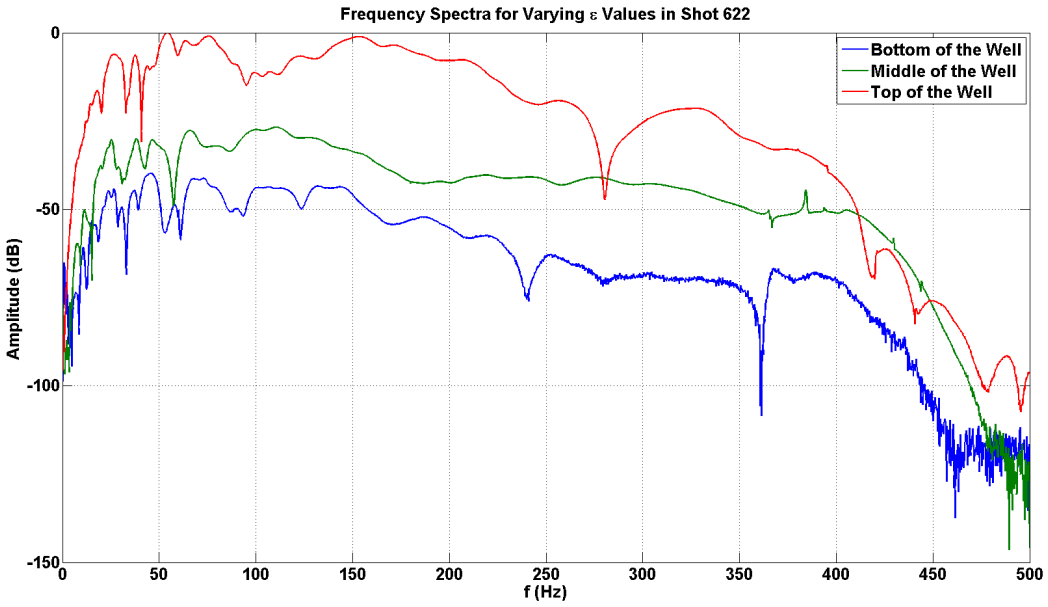

Figure 9.25: Frequency spectra three sensors in shot 622. One sensor is at the bottom of the well, one sensor is near the middle of the well, and one sensor is at the top of the well.

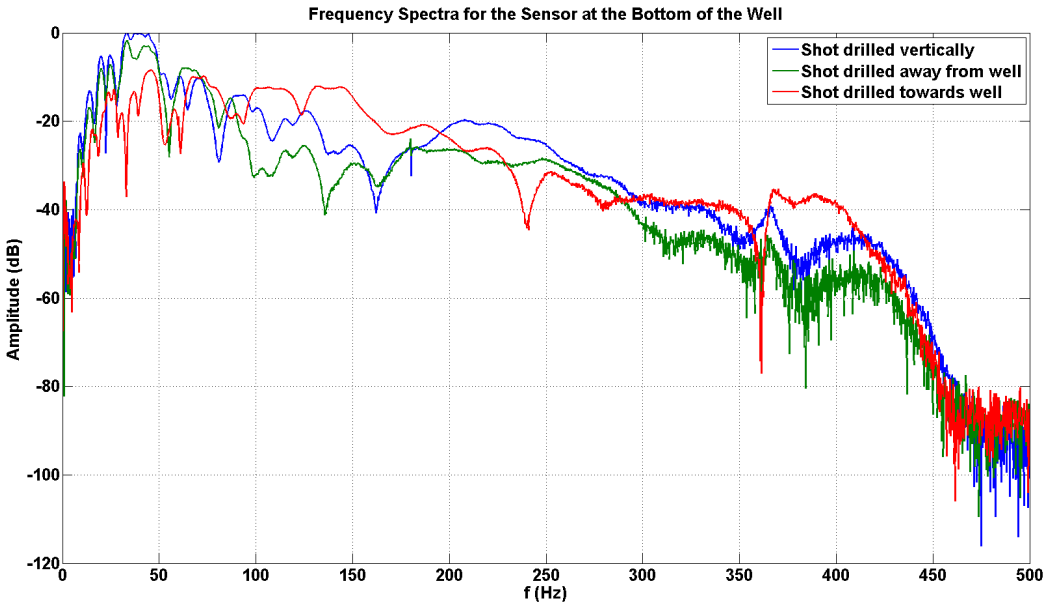

Figure 9.26: Frequency spectra from the bottom sensor for all three shot records.

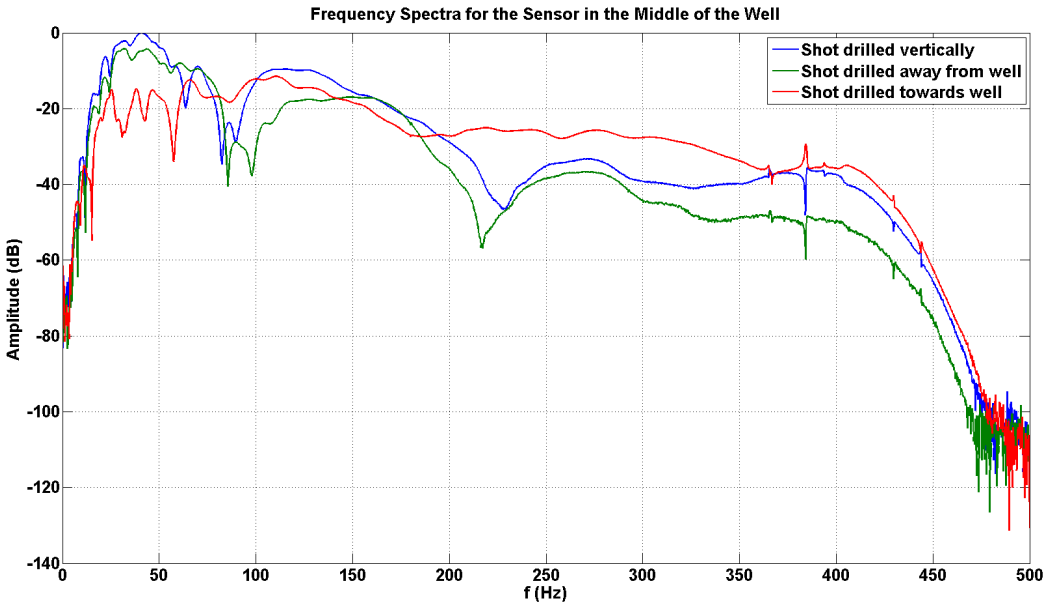

Figure 9.27: Frequency spectra from the middle sensor for all three shot records.

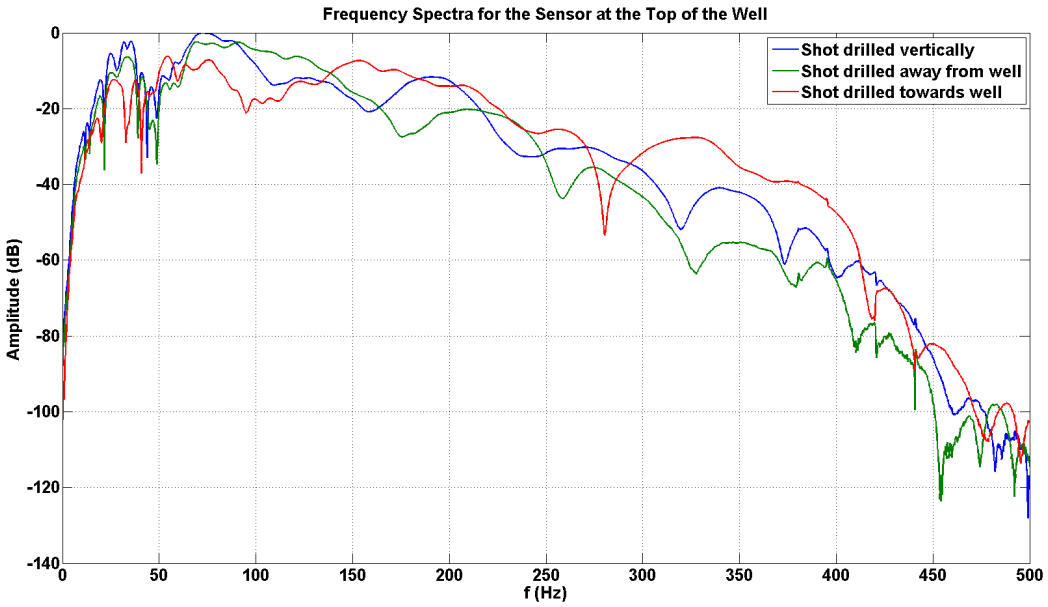

Figure 9.28: Frequency spectra from the top sensor for all three shot records.

Chapter 10

Conclusions and Future Work

10.1 Thesis Conclusions

- When ascribing a pressure pulse to the SHCM, a pulse must be chosen that produces a frequency spectra that shares the same form as that obtained from dynamite data in practice.

- The SHCM predicts that overall amplitude response should increase with charge size, but the dominant frequency should decrease with larger charge sizes. There must also be a low-frequency roll-off present in the data. Each of these predictions made by the SHCM was observed in both the Hussar 2011 and Priddis 2012 experiments.

- When utilizing the SHCM, our method for determining the c-value for a medium appears to produce reasonable accurate predictions about the amplitude and frequency content of dynamite data used in practice, which suggests that it is a viable method for determining the c-value of a medium.

- Based on our results of the SHCM, we can conclude that it is able to make accurate predictions regarding the amplitude and frequency content of waves emitted by explosive pressure sources.

- The GPSM produced a frequency spectra that was of the same form as that obtained from real data.

- We were not able to use the GPSM to predict the amplitude response and frequency spectra of the Hussar 2011 and Priddis 2012 data sets. This was largely due to the fact

that we could not produce significant enough variations in Gaussian ball widths in the GPSM to match it with our observed data.

- Currently, we cannot use the GPSM to make reliable predictions about dynamite data obtained in practice.
- The HCM predicts amplitude variation along the axial and radial components of the borehole.
- The HCM predicts maximum amplitude along the radial component of the cylindrical cavity.
- A variation in amplitude with both measurement angle and borehole orientation was observed in the Priddis 2013 data set.
- The orientation of the borehole may affect the radiation pattern that results from a charge within a borehole. The borehole that was drilled away from the well produced the most energy, and the borehole that was drilled towards the well produced the smallest amount of energy.
- Drilling the boreholes at an angle in seismic surveys may be an effective way to direct energy to regions in which a larger amount of power is desired.
- There was no significant variation in frequency with borehole orientation.
- Further research is required before we can draw any reliable conclusions regarding the ability of the HCM to predict features of dynamite data obtained in practice.

10.2 Suggestions for Future Work

- It would be worthwhile to collect more dynamite data for a wider range of charge sizes, in order to examine whether or not the relationship between shot power and charge size

is linear for very large charge sizes as well. If the relationship between charge size and power is not linear for charge sizes larger than those contained in this study, we may only be able to reliably use the SHCM for the charge sizes that were used in this experiment.

- Utilizing the SHCM over a wider variety of geological areas can test the versatility and robustness of the model, and help us to determine whether or not there are settings in which it cannot be used.

- In order to improve upon the utilization of the GPSM, it may be worthwhile to investigate a more robust means of determining a c-value for the medium. Accomplishing this may help us determine whether or not our inability to match the GPSM with measured data is a result of a scaling issue, or an incorrect link between charge size and the Gaussian ball width.

- To further investigate the HCM we require a much wider range of borehole orientations as we were very limited in this study.

- In the Priddis 2013 experiment, the charges were placed very close to the surface, which greatly limited the range of ϵ values in our data. By burying the charges deeper into the subsurface, we may be able to observe energy patterns that occur above the source.

- The energy at the top of the well during the Priddis 2013 experiment is not very well understood at this point, other than the fact that it does not appear to be affected by rotations of the sensors. By bettering our understanding of this energy, we may be able to determine if its behavior can be modeled by the HCM.

Bibliography

[1] Aki, K., and P. G. Richards, 1980, Quantitative seismology, theory and methods: W. H. Freeman and Company.

[2] Aldridge, D. F., 1998, Elastic wave radiation from a line source of finite length, Technical Report SAND98-2474, Sandia National Laboratories.

[3] Aldridge, D. F., 2002, Elastic wave radiation from a pressurized spherical cavity, Technical Report SAND2002-1882, Sandia National Laboratories. ssss

[4] Aldridge, D. F., and S. S. Collis, 2011, A Gaussian explosion seismic energy source: SEG Technical Program Extended Abstracts, 2297-3001.

[5] Arfken, G., 1985, Mathematical methods for physicists, 3rd Edition: Academic Press, Inc., 794-865.

[6] Bayin, S. S., 2006, Mathematical methods in science and engineering, 1st Edition: John Wiley and Sons, 347-360.

[7] Bertram, M. B., and K. W. Hall, 2012, The pulse-probe experiment - a look at the Autoseis recording system: CREWES Research Reports, **24**, 10.

[8] Bertram, M. B., Lawton, D. C., Hall, K. W., Bertram, K. L., and E. V. Gallant, 2012, Recent data from the Priddis Geophysical Observatory: CREWES Research Reports, **25**, 12.

[9] Blair, D., 2007, A comparison of Heelan and exact solutions for seismic radiation from a short cylindrical charge: Geophysics, **72**, no.2, E33-E41.

[10] Habberjam, G. M., and J. T. Whetton, 1951, On the relationship between seismic amplitude and charge of explosive fired in routine blasting operations: Geophysics, **17**, 116-128.

[11] Hall, K. W., Bertram, K. L., Bertram, M. B., Gallant, E. V., Margrave, G. F., and Lawton, D. C., 2013, Installation of the new observation wells at the Priddis Geophysical Observatory, **25**, 30.

[12] Hambartan, N. S. and Margrave, G. F., 1998, Analysis of a ghost: CREWES Research Reports, **10**, 4-1 - 4-26.

[13] Hatton, L., Worthington, M., Makin, J., 1986, Seismic Data Processing - Theory and Practice: Blackwell Scientific Publications.

[14] Heelan, P. A., 1953, Radiation from a cylindrical source of finite length: Geophysics **18**, 685-696.

[15] Margrave, G. F., Mewhort, L., Phillips, T., Hall M., Bertram, M., Lawton, D. C., Innanen, K. A. H., Hall., K. W., and K. L. Bertram, 2011, The Hussar Low-Frequency Experiment: CREWES Research Reports, **23**, 78.

[16] Nicholls, H. R., and W. I. Duvall, 1965, Effect of charge diameter on explosive performance, Report of Investigations TN23.U7 no. 6806 622.06173, U.S. Department of Interior.

[17] O'Brien, P., 1957, The relationship between seismic amplitude and weight of charge: Geophysical Prospecting, **3**, 349-352.

[18] Sharpe, J. A., 1942, The production of elastic waves by explosion pressures, Part I: Theory and empirical field observations: Geophysics, **7**, 144-154.

[19] Sharpe, J. A., 1942, The production of elastic waves by explosion pressures, Part II: Results of observations near an exploding charge: Geophysics, **7**, 311-321.

[20] Sharpe, J. A., 1944, The effect of charge size on reflection records: Geophysics, **9**, 131-142.

[21] Sheriff, R. E., 1975, Factors affecting seismic amplitudes: Geophysical Prospecting, **23**, 125-138.

[22] Sramek, O., and Y. Ricard, 2007, Simultaneous melting and compaction in deformable two-phase media: Geophysics Journal International, **168**, 964-982.

[23] Ziolkowski, A., 1993, Determination of the signature of a dynamite source using source scaling: Part 1, Theory: Geophysics, **58**, 1174-1182.